

Pharmacological Inhibition of the Methyltransferases SUV4-20 in Cellular Models of Friedreich's Ataxia

Saumya Maheshwari

Supervisors: Gabriela Vilema-Enríquez and Richard Wade-Martins

Laboratory for Molecular Neurodegeneration and Gene Therapy

Department of Physiology, Anatomy and Genetics

Submitted in fulfilment of the requirements for the degree of Master of Science by Research in Physiology, Anatomy and Genetics

Academic year 2020-2021, Christ Church

Acknowledgements

I would like to express my deep gratitude to Professor Wade-Martins for welcoming me into his lab. He has given me the invaluable opportunity to explore my passion for scientific research in a truly exciting and nurturing environment. I would like to thank him for his generosity, energy and for supporting my growth as a scientist.

I would also like to thank my supervisor Dr Gabriela Vilema-Enríquez. I could not have asked for a better teacher, mentor and friend. She has been by my side throughout this journey and words cannot express how grateful I am for her time, guidance and companionship over the past year. Thank you for being such a **brilliant** mentor and for helping me see the potential I carry within myself. Additionally, thank you for all your help with my experiments.

Thanks to everyone in the Wade-Martins lab, for their energy, assistance, conversations and friendships. In particular, Dr Sandor Szunyogh for his enormous help throughout my project, teaching me several laboratory techniques and keeping me entertained in the lab with his humour. Thanks to Dr Sukrat Arya for his initial guidance and assistance at the beginning of this journey.

I would also like to thank Professor Sally Cowley and Jane Vowles for generating the control iPSC lines as well as Professor Joel Gottesfeld and Dr Elisabetta Soragni for donating the FRDA iPSC lines. Thank you to our medicinal chemist collaborators, Professor Paul Brennan and Robert Quinlan for deriving the A-196 structural analogues, Dr Fengling Li and

Professor Masoud Vedadi for providing me with the chemical potency data and Dr Suzanna Ackloo for providing me with the negative probe SGC-2043.

Thank you to Dr Javier Tello, Dr Frederic Picard and Professor Keisuke Kaji, alongside all the other amazing teachers I have had the blessing to learn from over the past few years. Their presence in my life has fuelled my passion to learn.

Thanks to all my friends, who have been a constant source of support and who help me see the best in myself every day.

And finally, a special thanks to my family. Thank you for prioritising my education and for allowing me to pursue my passions and dreams. I am so grateful for your encouragement, care, belief and unconditional love. Thank you for shaping me into the person I am today. None of this would be possible without you.

Table of Contents

Abbreviations *10*

Abstract *13*

1. Introduction to Friedreich's Ataxia *15*

1.1. Disease Overview **15**

1.2. Genetics **15**

1.2.1. Identification of *FXN* and the Repeat Expansion 15

1.2.2. Other Genotypes 16

1.3. Clinical Phenotype **17**

1.3.1. Classical Disease Course 17

1.3.2. Neurological Presentations 18

1.3.3. Cardiovascular Presentations 19

1.3.4. Other Presentations 19

1.3.5. Atypical Presentations 20

1.4. Disease Management **21**

1.4.1. Diagnosis 21

1.4.2. Treatment 22

1.5. Frataxin and Its Role in Disease Pathology **22**

1.5.1. Frataxin Localisation 22

1.5.2. Frataxin Function 23

1.5.3. Mechanisms of Reduced Frataxin Biogenesis 24

1.5.4. Consequences of Reduced *FXN* Expression 25

1.5.5. Specificity of Tissue Dysfunction Explained by *FXN* Expression 25

1.6. Disease Pathophysiology 27

1.6.1. Degeneration within the Nervous System 27

1.6.2. Cardiac Pathophysiology 28

1.7. Current Therapeutic Avenues for FRDA 29

1.7.1. Iron Chelators 29

1.7.2. Anti-oxidant Therapy 30

1.7.3. Increasing Frataxin 30

1.8. Epigenetic Based Therapy for FRDA 31

1.8.1. HDAC Inhibitors 31

1.8.2. Histone 4 K20 Methylation 32

1.8.3. Targeting SUV4-20 Methyltransferases 33

1.8.4. Chemical Inhibition of SUV4-20 by A-196 and its Structural Derivatives 33

1.9. iPSCs and FRDA Drug Discovery 35

1.9.1. Current Paradigm of Drug Discovery 35

1.9.2. Traditional *In Vitro* Models of FRDA 35

1.9.3. Introduction to iPSC Technology 36

1.9.4. Development of FRDA iPSCs and their Derived Models 37

1.9.5. FRDA iPSC-Derived Neurons 39

1.10. Background Summary and Project Relevance 39

2. Thesis Aims *41*

2.1. Aim 1: To Investigate the Effectiveness of A-196 Structural Derivatives to Increase *FXN* Expression in Cellular Models of FRDA 41

2.2. Aim 2: To Establish an FRDA iPSC-derived Sensory Neuronal Model 41

3. Methods *43*

3.1. Cell Lines 43

3.1.1. HEK Reporter Cell Line 43

3.1.2. Fibroblasts 43

3.1.3. iPSCs 44

3.2. HEK Compound Screening Treatment Protocol 45

3.3. Concentration Response Testing 45

3.4. Luciferase assay 46

3.4.1. 96-well Plate Protocol 46

3.4.2. 384-well Plate Protocol 47

3.5. BCA assay 47

3.6. Fibroblast testing 47

3.7. Fibroblast qRT-PCR 48

3.8. iPSC Culture 49

3.8.1. Protocol 1 50

3.8.2. Protocol 2 50

3.8.3. iPSC Replating 54

3.9. Immunocytochemistry **55**

3.10. iPSC qRT-PCR **57**

3.11. Cell Counting **58**

3.12. Statistical Analysis **59**

4. Results ***60***

4.1. A-196 Structural Derivatives Increase *FXN* Expression in Cellular Models of FRDA **60**

4.1.1. Select Structural Analogues of A-196 Increase *FXN* Expression in Initial Screen 60

4.1.2. Structural Analogues of A-196 are Validated by Initial Concentration Response Testing 63

4.1.3. Structural Analogues Display Confirmed Toxicity at Higher Concentrations 67

4.1.4. Structural Analogues Potentially Increase *FXN* Expression in FRDA Patient-Derived Fibroblasts 72

4.2. Establishing an iPSC-derived Sensory Neuronal Model of FRDA **74**

4.2.1. iPSCs Exhibit Clear Morphological Changes During Neurogenesis 74

4.2.2. Cells Exhibit Sensory Neuronal Gene Expression Profiles During Differentiation 81

4.2.3. Immunocytochemistry Confirms Expression of Neuronal Markers 85

5. Discussion ***93***

5.1. A-196 Structural Derivatives Increase *FXN* Expression in Cellular Models of FRDA **93**

5.1.1. The Potential of Targeting Histone Methyltransferases SUV4-20 H1 93

5.1.2. Development of A-196 Structural Analogues 95

5.1.3. Select Structural Analogues of A-196 Increase *FXN* Expression in Initial Screen 96

5.1.4. Validation of Structural Analogues by Initial Concentration-Response Testing 98

5.1.5. Broader Range Concentration-Response Screen Confirms High-Dose Toxicity 99

5.1.6. The GAA-*FXN*-Luciferase Reporter Cell Line as a Model for FRDA 100

5.1.7. Structural Analogues Potentially Increase *FXN* Expression in FRDA Patient-Derived Fibroblasts 102

5.1.8. The Influence of Repeat Length on Compound Effect Sensitivity 103

5.1.9. Evaluating the Optimal Treatment Concentration 104

5.1.10. A-196 as a Variable Positive Control 104

5.1.11. Target Upregulation Required for Therapeutic Benefit 106

5.2. Establishing an iPSC-derived Sensory Neuronal Model of FRDA 107

5.2.1. Why Develop iPSC-derived Models for FRDA? 107

5.2.2. Generation of Specific Neuronal Subpopulations of the DRG 108

5.2.3. Inter-Protocol Differences in Neuronal Generation 109

5.2.4. Protocol Optimisation 110

5.2.5. Cells Exhibit Sensory Neuronal Gene Expression Profiles During Differentiation 111

5.2.6. Determination of Neuronal Subpopulations Derived 112

5.2.7. Analysis of *FXN* Gene Expression Profiles 114

5.2.8. Interpretation of ICC Staining 115

5.2.9. Limitations of iPSCs: Cell Variability 116

5.2.10. Limitations of iPSCs: Age-Related Maturity 117

5.2.11. iPSCs and a New Paradigm for FRDA Drug Discovery 118

6. Conclusion and Future Perspectives 121

6.1. Conclusions 121

6.1.1. A-196 Structural Derivatives Increase *FXN* Expression in Cellular Models of FRDA 121

6.1.2. Establishing an iPSC-derived Sensory Neuronal Model of FRDA 121

6.2. Future Perspectives 122

6.2.1. Altering Treatment Length 122

6.2.2. Evaluation of Phenotypes 123

6.2.3. Alternative Therapeutic Approaches 124

Appendices 147

Abbreviations

FRDA	Friedreich's ataxia
GAA	Guanine adenosine adenosine
DRG	Dorsal root ganglion
ECG	Electrocardiogram
LOFA	Late-onset Friedreich's ataxia
VLOFA	Very late-onset Friedreich's ataxia
FARR	Friedreich's ataxia with retained reflexes
AVED	Ataxia with vitamin E deficiency
PCR	Polymerase-chain reaction
MMP	Matrix metalloproteinase
ISC	Iron-sulphur cluster
MRI	Magnetic resonance imaging
BBB	Blood brain barrier

CoQ	Coenzyme Q
EPO	Erythropoietin
UCM	Ubiquitin-competing-molecules
TAT	Transactivator of transcription
HDACi	Histone deacetylase inhibitor
HMTase	Histone methyltransferase
HAT	Histone acetyltransferase
HDAC	Histone deacetylase
PBMC	Peripheral blood mononuclear cell
HDM	Histone demethylase
iPSC	Induced pluripotent stem cell
ESC	Embryonic stem cell
RPE	Retinal pigment epithelium
PSN	Peripheral sensory neuron

DMEM	Dulbecco’s modified eagle medium
PBS	Phosphate-buffered saline
FBS	Fetal bovine syndrome
MEM	Minimum essential media
ICC	Immunocytochemistry
PFA	Paraformaldehyde
NDS	Normal donkey serum
DAPI	4’,6-diamidino-2-phenylindole
PV	Parvalbumin
DEG	Differentially expressed genes
SNP	Single nucleotide polymorphism
NGN1	Neurogenin 1
NGN2	Neurogenin 2
iNs	Induced-neurons

Abstract

FRDA is the most common hereditary ataxia in the western world. The disorder is characterised by a pathological GAA trinucleotide repeat expansion in the *FXN* gene, resulting in a decrease in the expression of its encoded protein, frataxin. Symptoms commonly arise during adolescence, with patients exhibiting a clinical syndrome of progressive neurodegeneration, cardiomyopathy and endocrine dysfunction. FRDA remains without a cure, likely due to our incomplete understanding of disease pathology, coupled with limitations surrounding the *in vitro* models historically used for drug discovery. Recently, the methyltransferases SUV4-20 have been identified for their role in facilitating the partial silencing of *FXN*, through an increase in repressive H4K20 di- and tri-methylation marks. Inhibition of SUV4-20 by the tool compound A-196 has been show to rescue *FXN* expression, implicating SUV4-20 as an exciting therapeutic target for FRDA. Working in collaboration with medicinal chemists, we were provided with 22 structural derivatives of A-196, in order to determine their effectiveness to increase *FXN* expression. We found that several analogues were capable of increasing *FXN* expression in our *FXN*-Luciferase reporter model. Progression of the most promising analogues to testing in FRDA patient fibroblast lines, demonstrated one compound capable of significantly increasing *FXN* mRNA expression. Additionally, by adapting 2 previously published differentiation protocols we aimed to establish an iPSC-derived sensory neuronal model of FRDA. Utilising 2 control and 2 FRDA iPSC lines, we analysed the gene expression profiles and performed immunocytochemistry staining of derived cells, confirming the successful generation of an iPSC-derived sensory neuronal model. Further work is required to fully establish this model

and determine the subpopulations of PSNs derived. Thus, overall this project contributes to accelerating drug development for FRDA, firstly by advancing our understanding of the epigenetic mechanisms underpinning *FXN* repression, and secondly by working towards developing a phenotypically relevant cellular model of the disease.

1. Introduction to Friedreich's Ataxia

1.1. Disease Overview

Friedreich ataxia (FRDA) is the most common inherited ataxia, estimated to affect 1 in 50,000 individuals in the western world [1–3]. The eponymous disorder is named after the German neurologist, Nikolaus Friedreich, who first identified and described the disease in 1863 [4]. The majority of sufferers carry a characteristic guanine-adenine-adenine (GAA) repeat expansion in the intron 1 region of the frataxin (*FXN*) gene. The consequential repression of the *FXN* gene and subsequent decrease in expression of its encoded protein, frataxin, is acknowledged to be the principal cause of the disease phenotype. Symptoms frequently arise during late childhood, with patients exhibiting central and peripheral nervous system degeneration, alongside the development of substantial cardiac pathology [5,6]. FRDA is presently without a cure, however, recent advancements in our understanding of disease pathology, coupled with novel developments in disease modelling, have ensured exciting promise for the field of FRDA drug discovery.

1.2. Genetics

1.2.1. Identification of *FXN* and the Repeat Expansion

In his early studies of the disease, Nikolaus Friedreich noted the hereditary nature of FRDA [5,7]. It was not until later in the 20th century, with the aid of segregation analysis, that an autosomal recessive mode of inheritance was confirmed [6,8,9]. The gene and corresponding

mutation responsible for the FRDA phenotype was first identified in 1996 [3]. This was a GAA repeat expansion, located 1.4 kb downstream from exon 1 of the *FXN* gene (initially named *X25*), present on chromosome 9q13. The authors of the study named the 210-amino acid protein produced by the *FXN* gene, frataxin [3]. Chromosomes carrying hyperexpanded GAA repeats experience repressed frataxin expression, with FRDA patients producing 2-30% of frataxin compared to normal wildtype levels [10–14]. Unaffected chromosomes tend to carry between 6 to 27 GAA repeats, whilst FRDA chromosomes can carry expansions ranging from 44 to 1700 repeats [15]. A range of 700-800 GAA repeats is most commonly seen in FRDA patients [3,16], with frataxin production shown to be inversely correlated with expansion length [17–22]. Due to the meiotic instability of hyperexpanded repeats, it is frequent to observe expansion or contraction of GAA repeat lengths across generations [23,24]. A German study estimated an FRDA carrier rate of 1:60- 1:90 [25].

1.2.2. Other Genotypes

The vast majority of suffers (96%) are homozygous for expanded alleles, inheriting two expanded FRDA chromosomes. In a small number of remaining cases, individuals are compound heterozygotes, possessing one expanded FRDA chromosome and a point mutation in its corresponding homologous pair [3,15]. Nonsense and frameshift mutations result in null frataxin production from the affected chromosome, possibly explaining the lack of homozygous FRDA point mutation carriers, as such an individual would likely possess a lethal phenotype [26,27]. Compound heterozygotes tend to present with atypical phenotypes, with some missense mutations resulting in more mild phenotypic presentations, implicating residual functionality of mutated frataxin [6,26,28,29]. Interestingly,

there have also been reports of genetic locus heterogeneity in FRDA, with a small subset of patients presenting with FRDA phenotypes without hyperexpanded GAA repeats or discernible point mutations in their *FXN* gene [30,31].

1.3. Clinical Phenotype

1.3.1. Classical Disease Course

Friedreich ataxia tends to present in early adolescence, with the mean age of symptom onset being 10-15 years of age [32]. Around 20% of patients are younger than 5 when they present [9], whilst others may only display symptoms as late as the 8th decade of life [33]. The majority of patients present with difficulties in balance and coordination, often manifesting as slowly progressive gait ataxia. A small proportion also initially present with non-neurological signs, such as scoliosis [34]. Disease onset, severity and rate of symptomatic progression have all been shown to be inversely correlated with GAA expansion length [18,19,32].

Due to the progressive nature of the disorder, symptoms gradually worsen with time, resulting in most patients initially losing independent gait, followed by being wheelchair-bound by the 3rd decade of life [9]. Life expectancy for sufferers of FRDA is commonly reduced to around 40 years [6], but a number of patients can live considerably longer. Cardiac dysfunction presents the most common cause of death in FRDA patients, with other less frequent causes including stroke, diabetic coma and aspiration pneumonia [35–37].

1.3.2. Neurological Presentations

Almost all classical FRDA patients suffer from a neurological syndrome of progressive gait and limb ataxia, dysarthria (difficulty with speech), lower limb areflexia and sensory loss. Neuropathological degeneration within both the CNS and PNS, including the dorsal root ganglia (DRG), dorsal columns, spinocerebellar tracts and the cerebellum, is responsible for the neurological dysfunction seen in the majority of patients [38]. As the disease progresses, degeneration severity increases, resulting in a deterioration of symptoms. Ataxic gait is characteristically uncoordinated and staggered, with patients showing difficulty maintaining balance and walking in a straight line. This presents the earliest clinical sign for many patients, who respond to examination with a positive Romberg's test (ataxia is more prominent when visual input is removed). Patients will often further develop progressive truncal and appendicular ataxia, necessitating a gradual increase in support with their daily movement and a dependence on walking aids. This frequently results in exclusive wheelchair reliance a mean time of 15.5 years after symptom onset [9]. Dysarthria is another cardinal and early presenting feature of FRDA, caused by the weakness of muscles used for speech production. Patients display slurred speech, which may progress to become intelligible later in the disease course. Areflexia is the absence of deep tendon reflexes and is a robust clinical sign in FRDA, resulting from peripheral neuropathy. Patients often have absent upper and lower limb reflexes, with several studies noting that lower limb reflexes are lacking in almost all classical cases of FRDA [9,39,40]. Reduced muscle tone, muscle wastage and spasticity are just some of several additional symptoms which may further complicate patient management in advanced stages of the disease.

1.3.3. Cardiovascular Presentations

Signs of cardiovascular abnormalities can be found in the majority of FRDA patients, however, most remain asymptomatic until late in the disease course. Despite this, almost all patients will develop cardiomyopathy during their lifetime, with subsequent cardiac dysfunction representing the most common cause of death [35]. Cardiomyopathy is poorly correlated to the severity of neurological symptoms, emphasising the importance of robust and frequent clinical follow-up of cardiac disease in FRDA patients [41,42]. Hypertrophic cardiomyopathy (thickening of the intraventricular septum) can be seen in 2/3rd of individuals [43] with 35% of patients displaying concentric hypertrophy [44]. An electrocardiogram (ECG) shows further evidence of left ventricular hypertrophy in almost 1/5th of cases [45]. Patients may also develop replacement fibrosis resulting in the eventual dilation of their left ventricle, with 20% of patients suffering from a reduced ejection fraction [44]. Patients with a reduced ejection fraction are deemed "high risk", possessing longer GAA expansions and associated with higher mortality rates [42]. Further ECG abnormalities are found in 90% of patients [45], with findings including ST-T wave changes, such as T wave inversion and ST-segment elevation and depression.

1.3.4. Other Presentations

Patients suffering from FRDA can often present with several other clinical syndromes. One such is diabetes mellitus, whose association with FRDA was confirmed in the 1960s [46,47]. Diabetes often manifests late in the disease progression, with a mean age of 15 years after symptom onset [37]. Whilst the precise mechanism and association with FRDA is unclear,

aetiology is thought to be due to a combination of reduced insulin production due to pancreatic β-cell dysfunction and increased insulin resistance in the peripheral tissue. Almost 1/3rd of FRDA patients display evidence of diabetes or impaired glucose tolerance [19], with early-onset and longer disease duration increasing the risk of developing diabetes [37]. Patients often present acutely, potentially in a life-threatening state of ketoacidosis due to severe insulin deficiency.

A number of other clinical manifestations can be seen to disproportionately affect the FRDA population, including scoliosis (up to 100%) [48], optic nerve abnormalities (~18%) [49], obstructive sleep apnoea (21%) [50], lower urinary tract symptoms (82%) [51] and sensorineural hearing loss (13%) [19], amongst others.

1.3.5. Atypical Presentations

Alongside the classical phenotype of FRDA, approximately 25% of patients also present atypically [19]. These presentations include later-symptom onset or atypical features such as retained reflexes. Late-onset FRDA (LOFA) and very-late-onset FRDA (VLOFA) compose the majority of atypical presentations, with patients often exhibiting milder symptoms, slower progression and smaller repeat expansions [52]. Approximately 15% of patients present after the age of 25, with LOFA patients defined as those with symptom onset after the age of 25 and VLOFA patients presenting after the age of 40 [53]. With the advent of genetic testing, patients who present as late as the 6th and 7th decades of life can now be identified, with one report of disease onset at the age of 82 [33]. Patients with LOFA have been shown to express around 1.8 times the mean residual levels of frataxin in comparison to classical FRDA [13], likely accounting for the reduced disease severity and fewer non-neurological

manifestations in this disease population. A small subset of patients (less than 20%) will have a disease onset before the age of five [9]. These early-onset patients often possess larger repeat expansions, display more severe phenotypes, faster disease progression and have a higher incidence of cardiac complications, diabetes, pes cavus and scoliosis [39,52,54].

Approximately 12% of patients who are homozygous for the GAA expansion display FRDA with retained reflexes (FARR). These patients exhibit conserved tendon reflexes in their lower limbs and tend to have a later age of onset than classical FRDA patients. Additionally musculoskeletal abnormalities, cardiac complications and pes cavus tend to have a lower incidence in populations of FARR patients [55].

1.4. Disease Management

1.4.1. Diagnosis

Following symptom onset, FRDA may be suspected in an ataxic patient subsequent to medical history and extensive clinical examination. Differential diagnosis based purely on clinical examination is challenging, due to phenotypic overlap with several conditions including ataxia with vitamin E deficiency (AVED), Charcot-Marie-Tooth disease, hereditary motor and sensory neuropathy and others. This is evidenced by the clinical diagnostic criteria established by Harding, which achieves a 90% specificity, but is only 70% sensitive [9]. Confirmation of an FRDA diagnosis is made by genetic testing, often using Southern blotting or polymerase chain reaction (PCR) techniques to determine the presence of biallelic GAA expansions (> 66 repeats) in the *FXN* gene.

1.4.2. Treatment

Despite significant progress made in the field of therapeutic development for FRDA, there is currently no disease-modifying treatment capable of slowing or halting disease progression. For this reason current treatment for FRDA focuses on managing the symptoms experienced with disease progression alongside maintaining maximum functionality, independence and quality of life for those patients affected. This involves a holistic approach to care, with patients having access to a multidisciplinary team including neurologists, cardiologists, endocrinologists, physiotherapists, occupational therapists, geneticists and other specialists. Often patients are referred early to a specialist ataxia centre which facilitates access to specialist and patient-specific care. It is crucial that patients are monitored (often annually) to assess overall health and discuss management of their symptoms and disease progression [56]. This process will often involve tests such as an ECG, fasting blood sugar measurement, hearing assessment and sleep study [57].

1.5. Frataxin and Its Role in Disease Pathology

1.5.1. Frataxin Localisation

Frataxin is a 210-amino acid protein with a molecular weight of 23 kDa. The protein is highly conserved and essential for life, with *FXN* knock-out mice demonstrating early embryonic lethality [58]. Frataxin is encoded within the nucleus, then transcribed as a precursor within the cytoplasm, before being imported to the mitochondrion where the protein is acted upon by mitochondrial processing peptidase (MMP) resulting in a mature 14 kDa form. This mature construct, composed of amino acids 81-210, is the most common species in healthy

and diseased individuals [59–62]. It is well documented that frataxin localises to the inner mitochondrial membrane, evidenced by its co-localisation with a mitochondrial protein, the co-localisation of anti-*FXN* and anti-mitochondrial antibodies and experiments detailing reporter tagged *FXN* constructs [17,63,64]. Interestingly, as frataxin localises to the mitochondria, it has been expectantly shown that *FXN* mRNA is expressed predominately in tissues with a high metabolic rate, such as the heart, neurons, kidney and liver [63].

1.5.2. Frataxin Function

Despite the discovery of the *FXN* gene in 1996, a full characterisation of the precise function of frataxin still remains unclear. Regardless of this uncertainty, it is well supported that frataxin strongly influences mitochondrial iron homeostasis. This is likely due to its biochemical properties which enable it to modulate cellular iron redox chemistry, through its ability to bind, oligomerise, store and donate iron [65]. Studies utilising the yeast frataxin homologue Yfh1p have indicated that the protein regulates mitochondrial iron efflux, with deletion of Yfh1p resulting in mitochondrial iron overloading, depleted cytosolic iron and increased susceptibility to oxidative stress [64,66,67]. Reintroduction of Yfh1p was further shown to rapidly redistribute iron from the mitochondria to the cytosol [67].

Whilst frataxin plays a role in a number of iron-dependent pathways, its strong association with iron homeostasis is likely through its role in iron-sulphur cluster (ISC) formation. The ISCs are protein cofactors involved in redox reactions and oxidative phosphorylation within mitochondria. The process of ISC formation is crucial for many cellular and mitochondrial-specific functions, including iron uptake and utilisation, limitation of iron-catalysed oxidative stress, enzymatic catalysis and regulation of gene expression [68–70]. Since frataxin

plays a crucial role in ISC formation, frataxin deficient cells show defects in ISC and their associated enzymes, as demonstrated in frataxin scarce FRDA mouse models and patient cells [68,71–73].

1.5.3. Mechanisms of Reduced Frataxin Biogenesis

The presence of a pathological number of GAA repeats in the *FXN* locus results in transcriptional silencing of the gene and a resultant reduction in frataxin levels. The exact mechanism through which the GAA repeat expansion leads to loss of *FXN* transcription remains unclear, although 2 main possibilities have been speculated [74]. Firstly, it is postulated that expanded GAA repeats could cause the formation of atypical non-B DNA structures (triplexes known as "sticky DNA") [75–80] or the creation of inhibitory RNA-DNA hybrid structures (R-loops) [81]. These arrangements impede transcription through inhibition of RNA synthesis, due to sequestration and arrest of RNA polymerase respectively.

The second mechanism of transcriptional inhibition is the epigenetic silencing of the *FXN* gene via heterochromatin formation. It has been shown that expanded GAA repeats are capable of *FXN* silencing through a mechanism similar to heterochromatin-mediated position effect variegation [82]. Furthermore, several studies have documented a significant number of repressive epigenetic marks within the *FXN* locus [74]. These include aberrant DNA methylation and hydroxymethylation of CpG islands upstream of the GAA repeat region, associated with gene silencing [83–86]. Additionally, numerous repressive post-translational histone modifications have been identified to play a role in FRDA pathology. These include decreased acetylation of histones H3 and H4 (markers of euchromatin in an acetylated state) and hypermethylation of histones H3 (H3K9me2/3 and H3K27me3) and H4

(H4K20me3), associated with heterochromatic states [74,83,87–90]. These marks, present within the *FXN* locus, are thought to induce gene silencing though defective transcriptional initiation, as well as potential post-initiation impaired transcriptional elongation.

1.5.4. Consequences of Reduced *FXN* Expression

Patients with FRDA have been shown to express only 2-30% of the frataxin produced by healthy individuals [10–14]. This reduction in levels of frataxin result in a number of negative consequences at a cellular level (see **Figure 1**). It has been detailed that decreased frataxin causes impaired ISC and associated enzyme formation [91,92], resulting in aberrant iron homeostasis. This abnormal iron redistribution creates conditions of mitochondrial iron overloading, evidenced by increased mitochondrial iron in FRDA fibroblasts [93] and the discovery of iron deposits within the hearts of FRDA patients [94–96]. Iron overloading interferes with the electron transport chain, ultimately leading to dysfunctional energy metabolism and increased susceptibility to and accumulation of oxidative stress [70,97–100].

1.5.5. Specificity of Tissue Dysfunction Explained by *FXN* Expression

The specificity of tissue dysfunction and ensuing clinical picture observed in FRDA can be explained as a consequence of the properties of frataxin and its expression pattern within the body. As frataxin localises to the mitochondria, its expression is seen to be highest in tissues with a high metabolic rate [3,63], and thus high mitochondrial dependency. These cell types are particularly vulnerable to mitochondrial dysfunction and impaired energy metabolism, seen as a result of iron overloading. These include cardiomyocytes, neurons, pancreatic β-cells, hepatocytes and skeletal muscle cells. This predominantly mirrors the

clinical signs and symptoms observed in the cardiovascular, nervous and endocrine systems of classical FRDA patients. It is important to note that tissues within affected systems are generally non-dividing, whereas the liver and skeletal muscle contain actively mitotic cells, explaining why these cell types may be less affected by frataxin deficiency [3,6]. The differing capacities of tissues to manage oxidative stress, likely also plays a role in the observed clinical FRDA phenotype [101].

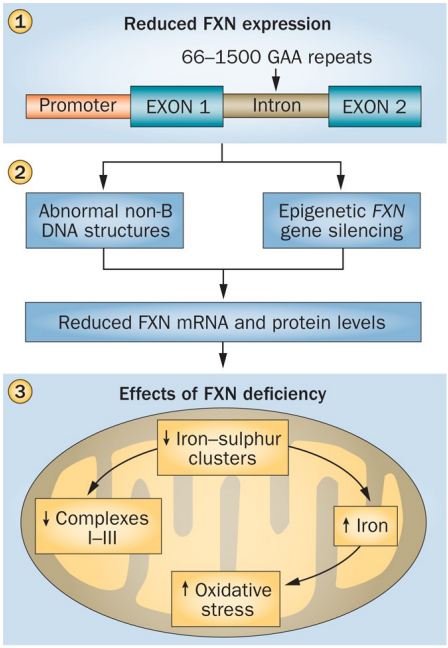


Figure 1: Pathogenesis and Consequences of *FXN* Deficiency

The presence of a pathological number of GAA repeats in the intron 1 region of the *FXN* gene leads to the formation of atypical non-B DNA structures, which inhibit RNA synthesis, and repressive epigenetic marks, which mediate *FXN* silencing through the formation of heterochromatin. The consequential decrease in *FXN* mRNA and intracellular frataxin protein levels has several downstream mitochondrial effects. Defective ISC formation due to frataxin deficiency results in mitochondrial iron overloading and increased oxidative stress. Figure taken from (De Michele, 2015) [102].

1.6. Disease Pathophysiology

1.6.1. Degeneration within the Nervous System

Despite FRDA patients displaying obvious neurological dysfunction, the underlying neuronal pathogenesis still remains relatively unclear. The major sites of neuropathology seen in FRDA are the DRG, dorsal and lateral columns of the spinal cord (particularly the spinocerebellar and corticospinal tracts) and the dentate nucleus of the cerebellum [6,38,103,104]. When examined macroscopically, there is a measurable decrease in spinal cord size, with the dorsal spinal roots appearing thin, and degeneration of the spinocerebellar and corticospinal tracts being visible [5,105]. Microscopically, the neurodegenerative process appears to particularly affect large-diameter and myelinated nerve fibres, with a reduction in the population of myelinated tubes and large axons in the posterior roots of FRDA patients [5,106].

Within the DRG, there is evidence of smaller ganglion cells and the absence of large neurons [5,107]. It is thought that progressive damage of neuronal cytoplasm in the DRG is mediated by invading satellite cells, which form a surrounding layer around neurons. Patients with FRDA possess a comparatively thicker rim of ferritin-reactive satellite cells, which also show an upregulation of ferroportin [5,108]. The increase in levels of these iron-responsive proteins within the DRG, potentially hint at a local iron excess, yet no studies have been able to directly confirm increased iron concentrations within the DRG of FRDA patients. It has been postulated that iron is redistributed from dying neurons to

surrounding glia (satellite cells) in the DRG, yet further research is required to elucidate exactly how aberrant iron metabolism results in neuropathophysiological changes [5,108–110].

Within the cerebellum, there is visible atrophy of the dentate nucleus and its efferent fibres[5], with deterioration of the superior cerebellar peduncle especially apparent in magnetic resonance imaging (MRI) studies [111,112]. The dentate nucleus is a naturally iron-rich structure, however, despite some evidence of increased iron in the region in FRDA using MRI signals [113], autopsies show no significant increase in iron concentrations when compared with controls [110,114]. Conversely, neurodegeneration within the cerebral cortex is mild, likely due to the area normally displaying minimal frataxin expression [3,6,63,115].

1.6.2. Cardiac Pathophysiology

In his early studies of the disease, Friedreich noted a gross "marble-'like pathological discolouration of the myocardium seen in FRDA patients [5,116]. The hearts of sufferers most commonly exhibit hypertrophic cardiomyopathy, with cardiomyocytes showing increased cross-sectional areas histologically [117]. Macroscopically FRDA hearts have a visible thickened left ventricular wall and interventricular septum, with some heart weights being over twice that of healthy controls [5,118]. Myocarditis is also a common finding, with FRDA myocardium displaying evidence of inflammatory invasion. Iron accumulation in FRDA myocardium has also been detailed, with sections of left ventricle displaying an abundance of cytosolic and mitochondrial ferritin [94,95,117].

1.7. Current Therapeutic Avenues for FRDA

Whilst treatment for FRDA currently focuses predominately on disease management, several disease-modifying therapies are currently being developed and explored, with varying levels of success. These approaches either focus on attempting to increase levels of intracellular frataxin, or tackling the downstream effects of frataxin deficiency such as pathological iron accumulation and oxidative stress-induced cellular damage.

1.7.1. Iron Chelators

As previously detailed, frataxin deficiency results in dysfunctional mitochondrial ISC synthesis and ultimately cellular iron overloading [69]. Utilising pharmacological iron chelators to target excess iron, presents a method to deal with the pathological consequences of iron accumulation seen in FRDA. One specific oral iron chelator which has been investigated in the hope to reduce intramitochondrial overloading in FRDA is deferiprone. Despite showing early promise [113], a phase II randomised placebo-controlled trial did not return positive results, with patients displaying worsening ataxia when treated with a daily dose of $\geq$ 40 mg/Kg deferiprone [119]. Interestingly, it has been reported that cells treated with $\geq$ 50 uM deferiprone, show signs of iron depletion rather than redistribution, even displaying decreasing frataxin levels [120]. These results highlight the importance of focusing not only on limiting the toxic effects of chelatable iron, but ensuring the correction of normal iron distribution without causing detrimental global changes in iron homeostasis [68].

1.7.2. Anti-oxidant Therapy

Frataxin deficiency increases susceptibility to oxidative stress, with FRDA cells showing increased levels of oxidative-induced damage. Thus, the use of antioxidant coenzymes such as coenzyme Q_{10} (CoQ), which are capable of passing through the blood-brain-barrier (BBB), present a potentially viable approach to protecting mitochondria from oxidative stress in FRDA. Idebenone is a structural analogue of CoQ which shows improved bioavailability and has been investigated in a number of FRDA studies. However, despite being well-tolerated in FRDA and able to enter brain mitochondria [121,122], two major phase III randomised placebo-controlled trials utilising Idebenone have failed to meet their primary neurological endpoints [122–125].

1.7.3. Increasing Frataxin

Another therapeutic approach being investigated involves attempting to increase the levels of intracellular frataxin, thus preventing the deleterious effects seen with its deficiency in FRDA. This could be achieved by several methods including increasing *FXN* expression, preventing frataxin degradation and the direct delivery of frataxin intracellularly. A number of therapeutic compounds have returned increased frataxin levels in preclinical testing such as erythropoietin (EPO) [126–128], ubiquitin-competing-molecules (UCMs) [129] and transactivator of transcription (TAT)-frataxin fusion proteins [130]. Gene therapy also presents a novel approach, with exciting results having been reported describing the reversal of cardiomyopathy phenotypes following the treatment of a mouse model of FRDA with an adeno-associated virus [131]. However, despite their potential

promise, none of these approaches have yet demonstrated significant clinical benefit in late-stage placebo-controlled trials with FRDA patients [122].

1.8. Epigenetic Based Therapy for FRDA

Over the past 2 decades, significant progress has been made to increase our understanding of the role of epigenetic modifications in the development of FRDA pathology. Consequently, therapies aimed at targeting repressive epigenetic marks in the *FXN* locus are currently the focus of significant scientific interest in the field of FRDA therapeutic development. Traditionally, attention has focused almost exclusively on the use of histone deacetylase inhibitors (HDACis), which remain the most investigated epigenetic-based therapy for FRDA [74,89]. However, more recently, novel findings from our lab have highlighted the enormous potential of histone methyltransferase (HMTase) inhibitors as a viable and hugely exciting avenue for the treatment of FRDA [90].

1.8.1. HDAC Inhibitors

Repressive post-translational histone modifications have been identified to play a key role in the development of FRDA pathology. One such epigenetic mark is the decreased acetylation of lysine residues present on histones H3 and H4, associated with transcriptional repression of the *FXN* gene. Two families of opposing enzymes, histone acetyltransferases (HATs) and histone deacetylases (HDACs), are responsible for the regulation of histone acetylation and consequentially, the transcriptional activity of affected genes. Several studies have investigated the use of HDACis, in the hope to reverse the decreased levels of acetylation of histones H3 and H4 seen in FRDA [74,89]. Following

positive *in vitro* data, two classes of HDAC inhibitor, RG2833 (class 1) and nicotinamide (class 3) have progressed to clinical testing [88,132–134]. In a phase I trial, RG2833 has been shown to increase levels of *FXN* mRNA and H3 acetylation in peripheral blood mononuclear cells (PBMCs) of treated FRDA patients [74]. An open-label clinical trial of nicotinamide, showed a dose-dependent rise in frataxin expression, increasing to levels similar to asymptomatic carriers when FRDA patients underwent 8 weeks of daily dosing [135]. Whilst nicotinamide was well tolerated and increased frataxin expression, treatment did not result in corresponding clinical benefits, illustrating the need for further research to determine whether HDACis could potentially attenuate FRDA phenotypes [122,135].

1.8.2. Histone 4 K20 Methylation

A number of histone methylation marks have also been associated with *FXN* gene repression in FRDA, including the hypermethylation of histones H3 (H3K9me2/3 and H3K27me3) and H4 (H4K20me3). Of particular interest are the epigenetic modifications which occur to histone 4 lysine 20, which possess three methylation states: mono- (H4K20me1), di- (H4K20me2) and trimethylated (H4K20me3) [74,136]. Both H4K20me1 and H4K20me2 methylation states are allied to DNA replication and DNA damage repair, whilst H4K20me3 is associated with the formation of heterochromatin and gene repression. It has been shown that within the genome, H4K20me3 is strongly enriched at repetitive elements, telomeres, imprinted regions and pericentric chromatin, highlighting its potential role in epigenetic-mediated transcriptional silencing [137–140]. Specifically in FRDA, H4K20me3 has been shown to be increased in sections of the *FXN* gene which flank the pathological GAA repeat expansion, indicating its involvement in disease pathology [141].

1.8.3. Targeting SUV4-20 Methyltransferases

Somewhat similarly to histone acetylation, histone methylation is regulated by a different family of two opposing enzymes, histone methyltransferases (HMTases) and histone demethylases (HDMs). The monomethyltransferase, SET8 (also known as KMT5a), is responsible for the generation of H4K20me1 states, whereas the family of SUV4-20 methyltransferases, consisting of SUV4-20 H1 and SUV4-20 H2, regulate histone 4 K20 di- and trimethylation [74,137]. Whilst SUV4-20 H1 and SUV4-20 H2 can act to generate both methylation states, they have been shown to have a preference to induce H4K20me2 and H4K20me3 states, respectively [137].

Recent findings published by our group have highlighted the importance of histone methyltransferases in the regulation of *FXN* expression. In particular, it was found that siRNA-mediated knockdown of SUV4-20 H1, significantly increased relative frataxin-luciferase expression in a reporter cell line and increased relative *FXN* mRNA in patient fibroblast cells [90]. These results validated the inhibition of SUV4-20 H1 as a promising therapeutic avenue for the treatment of FRDA.

1.8.4. Chemical Inhibition of SUV4-20 by A-196 and its Structural Derivatives

To further probe the inhibition of SUV4-20 H1 for the treatment of FRDA, the tool compound A-196 was investigated. A-196 is a highly selective substrate-competitive inhibitor of both SUV4-20 methyltransferases [142]. Our laboratory has previously shown that inhibition of SUV4-20 enzymes with A-196, reduces global levels of repressive H4K20me2

and H4K20me3 states, whilst simultaneously increasing H4K20me1 marks (see **Figure 2**). Treatment of FRDA patient PBMCs and fibroblasts with A-196, resulted in a corresponding increase in *FXN* mRNA expression. When off-target effects were examined in patient fibroblasts, minimal genome-wide perturbations in gene expression were found following treatment with A-196, establishing the compound as a promising candidate for FRDA drug discovery [90].

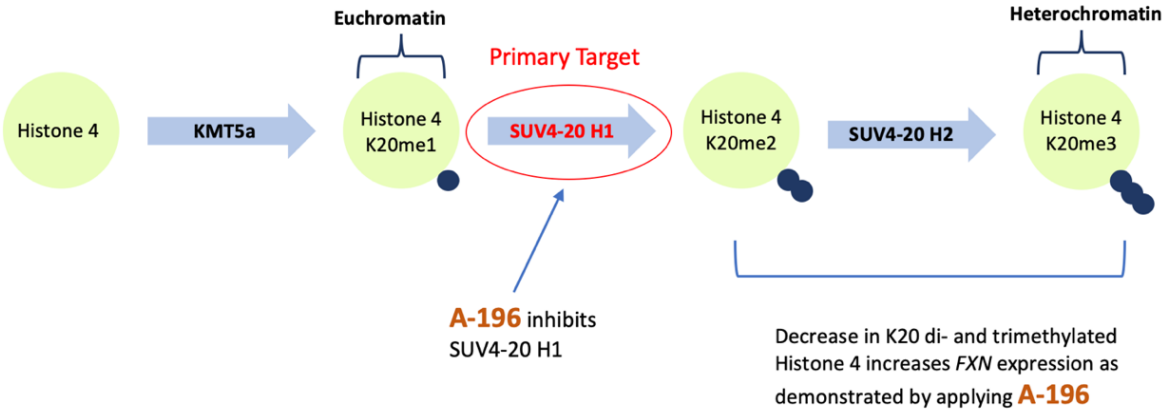


Figure 2: Inhibition of SUV4-20 H1 by A-196

Monomethylation of histone 4 K20 (H4K20me1) by methyltransferase KMT5a is associated with a euchromatic state and *FXN* expression. The SUV4-20 family of methyltransferases are responsible for histone 4 K20 di- and trimethylation. In FRDA, excess H4K20me3 is associated with the formation of heterochromatin and *FXN* gene repression. Treatment with tool compound A-196 inhibits SUV4-20 H1 and H2, resulting in a decrease in H4K20me2 and H4K20me3 repressive marks. A reduction in the heterochromatic H4K20me3 state, increases *FXN* expression, verifying the inhibition of SUV4-20 H1 as a promising therapeutic target in FRDA drug development.

1.9. iPSCs and FRDA Drug Discovery

1.9.1. Current Paradigm of Drug Discovery

In the classical paradigm of FRDA drug development, a large emphasis is placed on the *in vitro* discovery and testing of novel drugs. Traditionally, the initial identification of therapeutic targets is performed by high-throughput screening using reporter cell lines, before the efficacy and safety of potential compounds are tested in accessible patient cell lines. Only the most promising drug candidates would then progress to more expensive, complex and time-consuming *in vivo* animal studies and ultimately human clinical trials. However, despite the best efforts of researchers, doctors, advocacy groups and patients, FRDA still remains without an effective therapy. The vast majority of promising preclinical drugs fail to return any significant benefit when tested in the clinic. This discrepancy is likely due to our incomplete understanding of the underlying disease pathology, combined with several significant limitations with existing laboratory models of FRDA. The advent of induced pluripotent stem cell (iPSC) technology has revolutionised the field of drug discovery and development, enabling researchers to access improved *in vitro* models of FRDA, thus increasing the chances of developing an effective therapy for the disease.

1.9.2. Traditional *In Vitro* Models of FRDA

A number of FRDA reporter cell models have been described previously [143–147], including a *FXN* expanded genomic DNA reporter model which I utilised for preliminary compound screening in my project [148]. Reporter cell models and their corresponding cellular assays provide a rapid, efficient and relatively simple means to perform target identification

through the high-throughput screening of large libraries of potential therapeutic compounds. Following screening, the next step in the paradigm involves the use of diseased cell lines obtained directly from FRDA patients, such as fibroblasts, lymphoblastic cells or PBMCs. Patient cell lines are more complex and less efficient to work with than reporter cell lines, but possess a natural pathological FRDA genetic background, enabling more accurate disease representation. However, a major issue with commonly used FRDA patient cell lines is their phenotypic relevance to disease pathology. Readily accessible cell populations such as fibroblasts and PBMCs are not significantly affected by frataxin deficiency, whereas the most vulnerable cell types, such as neurons, cardiomyocytes and pancreatic β-cells, are not feasibly accessible from live FRDA patients.

1.9.3. Introduction to iPSC Technology

The introduction of iPSC technology provides researchers with a promising cellular tool to access the most desirable and phenotypically relevant cell types for FRDA research. Discovered by Yamanaka in 2006 [149], iPSCs act comparably to embryonic stem cells (ESCs), possessing the potential to propagate indefinitely *in vitro* and differentiate into mature cell types derived from any of the embryonic germ layers. They are obtained via epigenetic reprogramming of somatic cells by the overexpression of 4 key transcription factors (Oct4, Sox2, cMyc and Klf4) to induce pluripotency. The ability to generate iPSCs directly from mature and readily accessible somatic cells, such as patient fibroblast lines, bypasses many of the ethical issues which commonly surround the generation and supply of ESCs [150].

As technology within the field has progressed, laboratories worldwide have optimised the reprogramming process and developed iPSC differentiation protocols to generate a

number of neuronal phenotypes most commonly affected by neurogenerative diseases. These include dopaminergic, GABAergic, glutamatergic and motor neurons [151]. Excitingly, the ability to utilise patient somatic cells for iPSC generation has allowed for the subsequent differentiation of neuronal cell lines carrying a disease-specific genetic background, providing a crucial platform for therapeutic development. Advancements in the field, alongside increases in the efficiency of reprogramming and differentiation techniques, has resulted in iPSC technology gradually being adopted for the study of several rarer neurodegenerative disorders. Since FRDA pathology disproportionately affects many traditionally elusive cell types, it presents a model disease for which the use of iPSCs may enable exciting breakthroughs in drug discovery [152].

1.9.4. Development of FRDA iPSCs and their Derived Models

Just over a decade ago, the first study describing the generation of FRDA iPSCs was performed, reprogramming two FRDA patient primary fibroblast lines to create FRDA iPSCs [153]. The FRDA iPSCs not only maintained *FXN* gene repression, but also exhibited patterns of repeat expansion and contraction across generations, as commonly seen in human disease. One year later, neurons and cardiomyocytes were successfully generated from FRDA iPSCs [154], followed by a study published in 2013 demonstrating that mature cell types derived from FRDA iPSCs displayed a relevant frataxin deficiency phenotype [155]. Following these pioneering studies, groups worldwide have worked on developing and refining differentiation protocols for the generation of a number of elusive cell types from FRDA iPSCs, including neurons, cardiomyocytes, pancreatic β-cells and retinal pigment epithelium (RPE) cells (see **Figure 3**).

As these models represent cell types most phenotypically relevant to FRDA pathology, they have allowed researchers to examine the effects of any novel therapeutics in a disease representative *in vitro* model of FRDA [152].

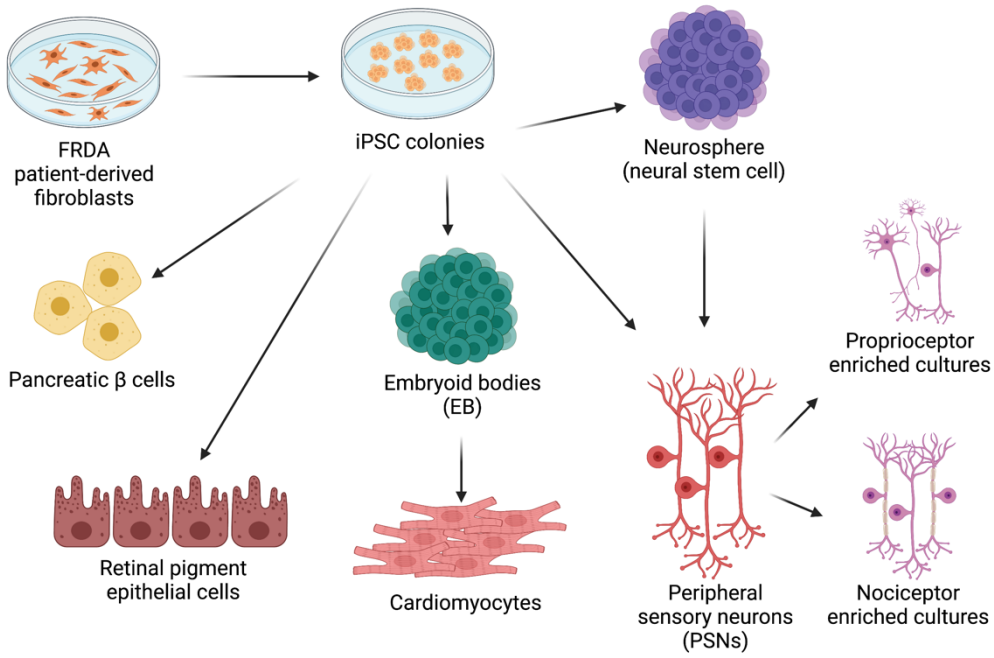


Figure 3: Generation of FRDA iPSCs and Their Derived Cellular Models

The generation of FRDA iPSCs is achieved by reprogramming patient-derived fibroblasts following treatment with pluripotency factors. The resulting FRDA iPSC colonies can be differentiated into a number of mature cell types with the addition of various differentiation factors. Of particular interest in FRDA are cells types vulnerable to *FXN* deficiency. Utilising FRDA iPSCs, groups worldwide have achieved success in generating FRDA cardiomyocytes, pancreatic β-cells, RPE cells and various subpopulations of neurons. Figure taken from (Maheshwari, Vilema-Enríquez and Wade-Martins, in preparation) and was created using BioRender.com.

1.9.5. FRDA iPSC-Derived Neurons

Of significant scientific interest, has been the development of differentiation protocols to generate diverse neuronal subpopulations from FRDA iPSCs. An early study showed that FRDA iPSC-derived sensory neurons, demonstrate characteristic pathological FRDA phenotypes such as reduced mitochondrial membrane potential and delayed development of electrophysiological functionality following differentiation [155]. More recently, there has been a shift in focus to develop protocols which generate populations of neurons more relevant to FRDA pathology, such as proprioceptors found in the DRG. The DRG is composed of many peripheral sensory neuron (PSN) subpopulations, including nociceptors, thermoreceptors, mechanoreceptors and proprioceptors. Although they comprise only 7.5% of PSNs found in the DRG, proprioceptors are responsible for the majority of *FXN* expression within the structure, making them the focus of interest when studying the development of FRDA pathology [108,156]. In my project I will utilise 2 previously described differentiation protocols in the hope to generate FRDA iPSC-derived sensory neurons. The 1st protocol has been shown to generate non-specific populations of PSNs [157], whilst the 2nd has described the generation of PSN cultures that are greatly enriched for proprioceptors [158].

1.10. Background Summary and Project Relevance

FRDA is the most common inherited ataxia in the western world, characterised by a pathological GAA trinucleotide repeat expansion in the *FXN* gene. The resulting decrease in *FXN* expression causes sufferers to experience a clinical syndrome of progressive

neurodegeneration, cardiomyopathy and endocrine dysfunction. The underlying pathophysiology is thought to be driven by reduced levels of intracellular frataxin, resulting in aberrant iron homeostasis, mitochondrial iron overloading and increased oxidative stress. Neuropathology is most apparent in the DRG, spinocerebellar and corticospinal tracts and the dentate nucleus of the cerebellum [5,38]. Despite attempts at the development of a number of disease-modifying therapies, FRDA still remains without an effective treatment. Epigenetic silencing of the *FXN* gene through heterochromatin formation presents a promising target for therapeutic development [74,89]. One exciting avenue currently being explored by our lab is the inhibition of histone methyltransferase SUV4-20 H1, with tool compound A-196 [90]. We have been working on testing structural derivatives of A-196 aiming to find a more potent compound capable of increasing frataxin levels in reporter and patient-derived cell lines. The advent of iPSC technology and its enormous potential for drug discovery, has enabled researchers the ability to study the effects of emerging compounds in novel and phenotypically relevant cellular models of disease. Thus, we are also working to establish an iPSC-derived sensory neuronal model of FRDA, which is capable of accurately recapitulating disease pathology and can be used to test our novel compounds.

2. Thesis Aims

This project consists of two major objectives, both aiming to contribute to the investigation and development of A-196 structural derivatives for the potential treatment of FRDA.

2.1. Aim 1: To Investigate the Effectiveness of A-196 Structural Derivatives to Increase *FXN* Expression in Cellular Models of FRDA

We have been provided several structural derivatives of A-196 by medicinal chemist collaborators from the Oxford Target Discovery Institute. The first aim of this project was to screen and determine the effectiveness of these compounds to increase *FXN* expression in two cellular models of FRDA. Compounds were initially screened utilising a *FXN*-GAA-Luciferase HEK293 reporter cell line, before the most promising derivatives progressed to testing in two FRDA patient-derived fibroblast lines (GM4078 and GM3816).

2.2. Aim 2: To Establish an FRDA iPSC-derived Sensory Neuronal Model

The second aim of this project was to establish an iPSC-derived sensory neuronal model of FRDA by following two previously published differentiation protocols. Utilising two control (SFC856-03-04, SFC156-03-01) and two FRDA patient (iPSC4078 and iPSC3816) iPSC lines, we quantified *FXN* expression and ran immunocytochemistry staining at various

differentiation timepoints to test for expression of key neuronal markers. We wish to establish and further use this iPSC-derived model to test the effectiveness of the most promising A-196 derivatives in a more phenotypically relevant cellular model of FRDA.

3. Methods

3.1. Cell Lines

3.1.1. HEK Reporter Cell Line

Initial compound screening and concentration-response testing were performed utilising *FXN*-GAA-Luciferase and *FXN*-Luciferase reporter cell lines. The reporter cell lines were both built using a HEK293 background as previously described, with the reporter luciferase (Luc) gene inserted in the exon 5a region of a 135kb human *FXN* locus [148]. Both cell lines had GAA repeats inserted in the intron 1 region of the *FXN* locus, with the pathological *FXN*-GAA-Luciferase line containing ~ 310 repeats and the control *FXN*-Luciferase line containing 6 GAA repeats. See **Figure 4** for a visual representation of the reporter cell lines utilised.

3.1.2. Fibroblasts

All fibroblasts lines were obtained from the Coriell Institute (USA). Two FRDA patient-derived primary fibroblast lines were utilised for compound testing (GM04078 and GM03816). GM04078 was derived from an FRDA patient with *FXN* alleles carrying 541 and 420 GAA repeats (average of 481 repeats), whilst GM03816 was derived from an FRDA patient with *FXN* alleles carrying 330 and 380 GAA repeats (average of 355 repeats). GM03440 is a control-derived primary fibroblast line which was utilised as a reference for normal *FXN* expression and contained a non-pathological number of GAA repeats.

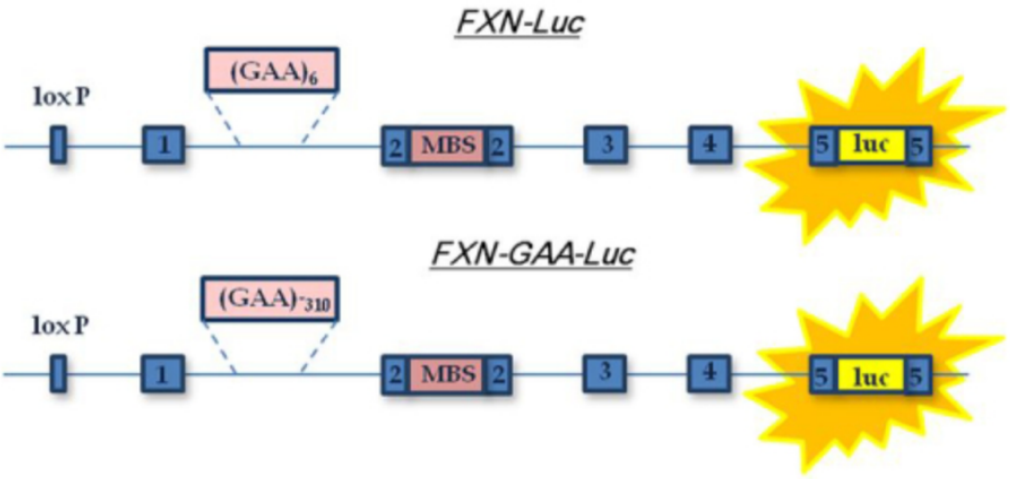


Figure 4: HEK293 Reporter Cell Lines

Schematic representation of reporter cell lines utilised for drug screening and concentration-response testing. Both reporter cell lines carry a 135kb human *FXN* locus with the luciferase gene inserted in the exon 5a region. The pathological *FXN*-GAA-Luciferase line carries ~310 repeats and the control *FXN*-Luciferase line carries 6 GAA repeats in the intron 1 region of the *FXN* locus. Both reporter lines were built using a HEK293 background. Figure taken from (Vilema-Enríquez *et al*, 2020).

3.1.3. iPSCs

We utilised two control-derived iPSC lines (SFC856-03-04, SFC156-03-01) which were generated and kindly provided by Sally Cowley and Jane Vowles from the Oxford James Martin Stem Cell Facility. The two FRDA patient-derived (iPSC4078 and iPSC3816) iPSC lines were provided by Joel Gottesfeld and Elisabetta Soragni from the Scripps Research Institute, California. All lines were used to establish an iPSC-derived sensory neuronal model of FRDA.

3.2. HEK Compound Screening Treatment Protocol

All HEK reporter cell culture was performed using Dulbecco's modified Eagle's medium (DMEM) high glucose, complemented with 10% fetal bovine serum (FBS), 100 units/ml penicillin/streptomycin, 2 mM L-glutamine and 100 µg/ml hygromycin B (Life Technologies) (complete DMEM). Structural derivatives were initially screened using *FXN*-GAA-Luciferase and *FXN*-Luciferase reporter cell lines. Cells were plated in poly-L-lysine (Sigma) coated 96-well plates at a density of 1.5 x 10^3 cells/well in triplicate. Cells were allowed to recover overnight, prior to treatment with A-196 structural derivatives at 5 µM. Two days following treatment, culture media was replaced with fresh media still containing A-196 structural derivatives at 5 µM. Two days following the media change, media was removed from the wells, prior to the wells being washed with phosphate-buffered saline (PBS) and finally plates were snap-frozen by placing on dry ice for ~ 5 minutes. SGC-2043, a structurally inactive analogue of A-196, was utilised as a negative control.

3.3. Concentration Response Testing

Selected structural derivatives were chosen to progress for either one or two rounds of concentration-response testing to validate efficacy. As with the initial compound screening, this was performed using *FXN*-GAA-Luciferase and *FXN*-Luciferase reporter cell lines, with a similar treatment protocol. Cells were plated in poly-L-lysine (Sigma) coated 384-well plates at a density of 0.5 x 10^3 cells/well in triplicate. Cells were allowed to recover overnight, prior to treatment with A-196 structural derivatives at specified concentrations. SGC-2043, a structurally inactive analogue of A-196, was utilised as a negative control. For

the first round of concentration-response testing, cells were treated at 7 concentrations ranging from 0.1-10 µM (0.1, 0.5, 1, 2.5, 5, 7.5 and 10 µM). The second round of concentration-response testing involved a broader range of concentrations, with cells being treated at 11 concentrations ranging from 0.6-40 µM (0.6, 1, 2.6, 5, 7.6, 10, 12, 15, 18, 20 and 40 µM). Cells were treated utilising the Echo 550 from Labcyte and the CyBio FeliX from Analytikjena. Two days following treatment, culture media was replaced with fresh media still containing A-196 structural derivatives at the required specified concentrations for each treatment condition. Two days following the media change, media was removed from the wells, prior to the wells being washed with PBS and finally plates were snap-frozen by placing on dry ice for ~ 5 minutes. Following treatment for the broader concentration-response screen, images of cells were taken at 5X using a Thermo Fisher Scientific EVOS^{TM} XL Core Imaging System.

3.4. Luciferase assay

In order to assess *FXN*-Luciferase expression in the reporter cell lines, a luciferase assay was performed utilising the Promega luciferase assay system kit (Promega, catalogue no. E1500), as per protocol instructions and using the kit reagents. The protocol followed differed slightly according to the plate size.

3.4.1. 96-well Plate Protocol

Cells were washed with PBS and lysed by the addition of 80 µl of cell culture lysis reagent to each well containing cells. Plates were incubated for ~ 15 minutes on a plate rocker at 4 ℃. After incubation, cells were thoroughly resuspended, prior to 25 µl of cell lysate/well,

being transferred to a corresponding well in a white opaque 96-well white microplate (PerkinElmer). Utilising a PHERAstar FSX microplate reader (BMG LABTECH) with operational injector-pumps, 100 µl of luciferase assay reagent was loaded to each sample, prior to luminescence being measured to quantify luciferase expression.

3.4.2. 384-well Plate Protocol

A total of 40 µl of cell culture lysis reagent was added to each well containing cells. The cells were then thoroughly resuspended, prior to 15 µl of cell lysate/well, being transferred to a corresponding well in a 384-well white opaque optiplate (PerkinElmer). Utilising a PHERAstar FSX microplate reader (BMG LABTECH) with operational injector-pumps, 25 µl of luciferase assay reagent was loaded to each sample, prior to luminescence being measured to quantify luciferase expression.

3.5. BCA assay

Luminescence values obtained for *FXN*-Luciferase expression in reporter cell lines were normalised to total protein concentration as determined by BCA protein assay. The protocol was carried out following the manufacturer instructions (Pierce™ BCA Protein Assay Kit – Reducing Agent Compatible (Thermo Fisher, catalogue no. 23250).

3.6. Fibroblast testing

All fibroblast culture was performed using minimum essential medium (MEM, Gibco, 11095080) complemented with 15% FBS, 100 units/ml penicillin/streptomycin and 1% MEM nonessential amino acid solution (100X Gibco). Fibroblasts were plated at a density

of ~ 200,000 cells/flask in T25 cell culture flasks, before treatment the same day with A-196 structural derivatives at either 5 or 10 µM. Two days following treatment, the culture media was replaced with fresh media still containing A-196 structural derivatives at specified concentrations. Two days following the media change, cells were collected as follows:

1. Media was removed and flasks were washed with PBS
2. Trypsin was added to each flask, prior to incubation at 37 ℃ for ~ 5 minutes
3. Cells in trypsin were then resuspended and collected in media before being transferred to an Eppendorf tube
4. Cells were centrifuged at 300 x g for 5 minutes, before the supernatant was removed
5. The cell pellet was then resuspended in PBS before being transferred to a microcentrifuge tube and centrifuged at 300 x g for 5 minutes
6. Finally the supernatant was removed, before the microcentrifuge tubes were placed on dry ice

3.7. Fibroblast qRT-PCR

Total mRNA was extracted from fibroblast cell pellets utilising reagents and following protocols from the RNeasy mini kit (Qiagen). Extracted mRNA was treated with RNase-free DNase (Qiagen). Following extraction, obtained mRNA concentrations were measured using a DeNovix DS-11 spectrophotometer. To synthesise cDNA, 1 µg of mRNA was added to 10 µL of 2X RT Buffer Mix, 1 µL of 20X RT Enzyme Mix and the required volume of

nuclease-free H_20 to create a total 20 µl reaction volume. All RT reagents were obtained from the High-Capacity RNA-cDNA™ Kit (Thermo Fisher, catalogue no. 4388950). Quantitative PCR was carried out utilising the *FXN* and *HRPT1* primers detailed in **Table 5**. Each reaction had a total volume of 20 µl, composed of 2 µl of 1/10 diluted cDNA, 1.4 µl of forward primer, 1.4 µl of reverse primer, 5.2 µl of DNase/RNase-free distilled water and 10 µl of Fast SYBR Green Master Mix (Thermo Fisher).

3.8. iPSC Culture

I utilised and slightly modified two previously described differentiation protocols to generate FRDA iPSC-derived sensory neurons. The 1st protocol has been shown to generate non-specific populations of PSNs, composed predominately of nociceptors, [157] whilst the 2nd protocol has described the generation of PSN cultures that are greatly enriched for proprioceptors [158]. For both protocols, iPSCs were initially maintained and passaged in mTeSR1 basal culture medium with 1X mTeSR1 supplement (STEMCELL Technologies). When iPSCs reached ~ 80% confluency, they were plated in Geltrex-coated plates at a high seeding density, prior to neural induction via the addition of small molecules and changing culture medium. The media and small molecules utilised varied according to each protocol (see **Figure 5** for a visual overview of both protocols). Cells were taken on days 15, 20 and 25 for immunocytochemistry and RNA extraction. To monitor progress during the differentiation, images of cells were taken at 10X daily using a Thermo Fisher Scientific EVOS™ XL Core Imaging System.

3.8.1. Protocol 1

On day 1, neural induction was commenced by changing media to KSR base medium (Knockout-DMEM, 15% knockout-serum replacement, 1% Glutamax, 1% nonessential amino acids, 100 µM β-mercaptoethanol, (Thermo Fisher)) and introducing dual SMAD inhibition with the addition of 10 µM SB431542 (Sigma) and 100 nM LDN-193189 (Sigma). On day 3, three additional small molecules were added to the KSR base medium, 3 µM CHIR99021 (Sigma), 10 µM SU5402 (R&D Systems) and 10 µM DAPT (Sigma), prior to removal of both SMAD inhibitors from day 7. From day 5, the KSR base medium was gradually transitioned in 25% increments every 2 days, to 100% N2 medium (Neurobasal medium, 2% B27 supplement, 1% N2 supplement, 1% L-Glutamine and 1% anti-anti (Thermo Fisher)) on day 11. On day 12, cells were replated to Geltrex matrix-coated plates in 100% N2 medium supplemented with growth factors BDNF, GDNF, NGF and NT3, all at 25ng/ml (Peprotech). Y-27632 rock inhibitor (STEMCELL Technologies) was added for day 12 only, whilst CHIR was included until day 14. Following replating day, medium changes occurred twice weekly and 1µM ARAC inhibitor (Sigma) was added to medium if undifferentiated cells were seen to be present. See **Table 1** for a summary of protocol 1.

3.8.2. Protocol 2

On day 1, neural induction was commenced by changing media to E6 medium (Thermo Fisher) and introducing dual SMAD inhibition with the addition of 10 µM SB431542 (Sigma) and 100 nM LDN-193189 (Sigma). From day 2, three additional small molecules were added to the medium, 3 µM CHIR99021 (Sigma) (stopped on day 7), 9 µM SU5402 (R&D Systems)

and 10 µM DAPT (Sigma) (both stopped on day 8), prior to removal of both SMAD inhibitors on day 6. Between days 4 and 8, the medium was gradually transitioned from E6 to N2-A medium (Neurobasal-A medium, 1% N2 supplement, 1% L-Glutamine and 1% anti-anti (Thermo Fisher)) with the following schedule: days 4-5 (75% E6, 25% N2-A), day 6 (50% E6, 50% N2-A) and days 7-8 (25% E6, 75% N2-A). On day 9, cells were replated to Geltrex-coated plates in N2-B medium (Neurobasal-A medium supplemented with 1% N2, 1% B27, 1% L-Glutamine, 1% MEM Non-Essential Amino Acids, 0.1% β-mercaptoethanol and 1% anti-anti (Thermo Fisher)) supplemented with growth factors 5ng/ml BDNF, 5 ng/ml GDNF, 5ng/ml NGF and 40 ng/ml NT3 (Peprotech). Y-27632 rock inhibitor (STEMCELL Technologies) was added for day 9 only. From day 10, GDNF and NGF were removed from the media. Following day 11, medium changes occurred twice weekly and 1µM ARAC inhibitor (Sigma) was added to the medium if undifferentiated cells were seen to be present. See **Table 2** for a summary of protocol 2.

Table 1: Tabular Day-by-Day Summary of Medium and Small Molecules for Protocol 1

Day	Media and Small Molecules
1	**Medium:** *KSR*
2	**Inhibitors:** 10 µM SB431542 and 100 nM LDN-193189
3	**Medium:** *KSR*
4	**Inhibitors:** 10 µM SB431542, 100 nM LDN-193189, 3 µM CHIR99021, 10 µM SU-5402 and 10 µM DAPT
5	**Medium:** 75% *KSR* + 25% *N2*
6	**Inhibitors:** 10 µM SB431542, 100 nM LDN-193189, 3 µM CHIR99021, 10 µM SU-5402 and 10 µM DAPT
7	**Medium:** 50% *KSR* + 50% *N2*
8	**Inhibitors:** 3 µM CHIR99021, 10 µM SU-5402 and 10 µM DAPT
9	**Medium:** 25% *KSR* + 75% *N2*
10	**Inhibitors:** 3 µM CHIR99021, 10 µM SU-5402 and 10 µM DAPT
11	**Medium:** *N2* **Inhibitors:** 3 µM CHIR99021, 10 µM SU-5402 and 10 µM DAPT
12 (Replating)	**Medium:** *N2* **Growth factors:** 25 ng/ml h-b-NGF, 25 ng/ml BDNF, 25 ng/ml GDNF and 25 ng/ml NT-3 **Inhibitors:** Y-27632 ROCK inhibitor and 3 µM CHIR99021
13-25	**Medium:** *N2* **Growth factors:** 25 ng/ml h-b-NGF, 25 ng/ml BDNF, 25 ng/ml GDNF and 25 ng/ml NT-3 **Inhibitors:** 3 µM CHIR99021 until day 14

Table 2: Tabular Day-by-Day Summary of Medium and Small Molecules for Protocol 2

Day	Medium and Small Molecules
1	**Medium:** *E6 medium* **Inhibitors:** 10 µM SB431542 and 100 nM LDN-193189
2	**Medium:** *E6 medium*
3	**Inhibitors:** 10 µM SB431542, 100 nM LDN-193189, 3 µM CHIR99021, 9 µM SU-5402 and 10 µM DAPT (1:10.000)
4	**Medium:** 75% *E6 medium* + 25% *N2-A*
5	**Inhibitors:** 10 µM SB431542, 100 nM LDN-193189, 3 µM CHIR99021, 9 µM SU-5402 and 10 µM DAPT
6	**Medium:** 50% *E6 medium* + 50% *N2-A* **Inhibitors:** 3 µM CHIR99021, 9 µM SU-5402 and 10 µM DAPT
7	**Medium:** 50% *E6 medium* + 75% *N2-A* **Inhibitors:** 3 µM CHIR99021, 9 µM SU-5402 and 10 µM DAPT
8	**Medium:** 25% *E6 medium* + 75% *N2-A* **Inhibitors:** 9 µM SU-5402 and 10 µM DAPT
9 (Replating)	**Medium:** *N2-B medium + ROCKi day 9* **Growth factors:** 5 ng/ml h-b-NGF, 5 ng/ml GDNF, 40 ng/ml NT-3 and 5 ng/ml BDNF
10	
11-25	**Medium:** *N2-B medium* **Growth factors:** 40 ng/ml NT-3 and 5 ng/ml BDNF

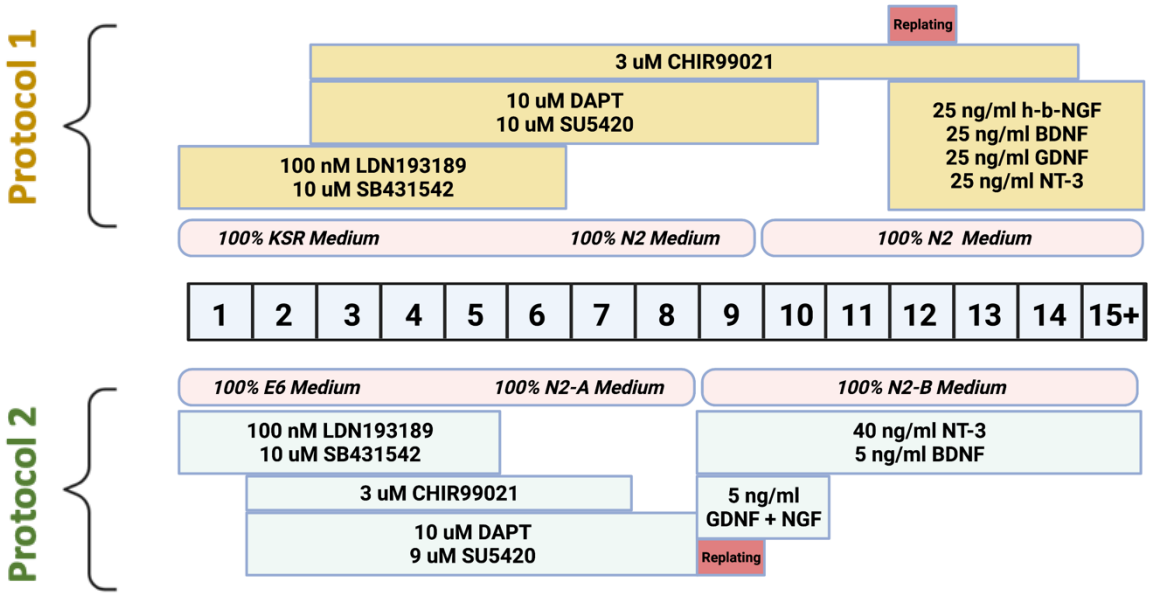


Figure 5: Visual Summary of Differentiation Protocols

A visual representation of both protocol 1 and protocol 2 used for the differentiation of iPSCs and generation of sensory neurons. Both protocols lasted for 25 days, but varied in the time of their replating day, the composition of media used and the concentrations and timings of small-molecule treatments during the differentiation. Figure created using BioRender.com.

3.8.3. iPSC Replating

For the 3rd differentiation, on day 9 (protocol 2) and day 12 (protocol 1) cells were replated onto Geltrex-coated plates. These plates had been treated with a poly-l-ornthine (Sigma, P4957) coating overnight, prior to being treated with Geltrex (Thermo Fisher, A1413202). Cells were passaged onto 96 well plates at a density of 15,000 cells/well for

immunocytochemistry and 12 well plates at a density of 100,000 cells/well for RNA extraction (3rd differentiation). The steps followed for replating were as follows:

1. Remove media from well
2. Add 0.5 ml of Accutase per well and incubate for ~ 5 minutes at 37 ℃, before carefully dissociating cells from the well surface mechanically
3. Resuspend cells in knockout DMEM and transfer to Eppendorf
4. Centrifuge cells at 300 x g for 5 minutes, before removing the supernatant
5. Resuspend cells in appropriate media (for specific protocol/day), before counting and passaging cells onto new plates as required

3.9. Immunocytochemistry

Following replating days, specific 96-well plates were taken on days 15, 20 and 25 of the differentiation for immunocytochemistry (ICC). Plates were fixed and stained as follows:

1. Media was removed from wells containing cells, prior to washing once with PBS
2. Cells were then incubated in 4% paraformaldehyde (PFA, Sigma) at room temperature for 10 minutes
3. The PFA was then removed, before washing with PBS twice
4. Cell membranes were then permeabilised using ice-cold 0.1% Triton-X-100 (prepared in PBS) for 10 minutes
5. Triton-X-100 was removed, cells were washed with PBS and then blocked with 10% Normal Donkey Serum (NDS, Sigma) for 30 minutes at room temperature
6. Cells were then incubated overnight at 4 ℃ with primary antibodies in 5% NDS

7. The next day, primary antibodies were removed. Cells were then washed in PBS three times for 5 minutes, prior to incubation with secondary antibodies in 5% NDS for 1 hour (at room temperature and protected from light)
8. Secondary antibodies were then removed and following two 5-minute washes with PBS, cell nuclei were stained with 1/5000 4',6-diamidino-2-phenylindole (DAPI) for 5 minutes. The DAPI stain was then removed and wells with cells for imaging were kept in PBS to prevent cells from drying out

Images were all acquired using a PerkinElmer Opera Phenix Plus high-content screening system and processed utilising Harmony high-content imaging and analysis software. See **Tables 3 and 4** for a summary of the primary and secondary antibodies utilised for staining.

Table 3: Primary Antibodies

Antibody	Dilution	Company	Catalogue Number
NF-200	1:10,000	Abcam	ab4680
Tubulin β-III	1:500	Biolegend	801202
RET	1:500	R&D Systems	AF1485
ISLET	1:100	Developmental Studies Hybridoma Bank	40.2D6 (0.1 ml)
TrkC	1:50	Santa Cruz	sc-80403
Parvalbumin	1:100	Abcam	ab11427
Runx3	1:50	Santa Cruz	sc-101553

Table 4: Secondary Antibodies

Antibody	Dilution	Company	Catalogue Number
Donkey Anti-Chicken IgG Alexa Fluor 647	1:1000	Millipore	AP194SA6
Donkey Anti-Mouse IgG Alexa Fluor 555	1:1000	Invitrogen	A31570
Donkey Anti-Rabit IgG Alexa Fluor 488	1:1000	Invitrogen	A21206
Donkey Anti-Mouse IgG Alexa Fluor 488	1:1000	Invitrogen	A21202
Donkey Anti-Goat IgG Alexa Fluor 555	1:1000	Invitrogen	A21432

3.10. iPSC qRT-PCR

Following replating days, specific 12-well plates were taken on days 15, 20 and 25 of the differentiation for RNA extraction. Total mRNA was extracted from the wells utilising reagents and following protocols from the RNeasy mini kit (Qiagen). Extracted mRNA was treated with RNase-free DNase (Qiagen). Following extraction, obtained mRNA concentrations were measured using a Quibit 3 Fluorometer (Thermo Fisher, Q33216). To synthesise cDNA, 5ng/µl of mRNA was used following the instructions of the SuperScript™ VILO™ cDNA Synthesis Kit. Quantitative PCR was carried out utilising the primers detailed in **Table 5**. Each reaction had a total volume of 20 µl, composed of 2 µl of 1/10 diluted cDNA, 1.4 µl of forward primer, 1.4 µl of reverse primer, 5.2 µl of DNase/RNase-free distilled water and 10 µl of Fast SYBR Green Master Mix (Thermo Fisher).

Table 5: Primers Utilised for RT-qPCR Experiments

Primers	Sequence (5'-3')
FXN-F	AACGTGGCCTCAACCAGATTT
FXN-R	GGTGGCCCAAAGTTCCAGATT
HRPT1-F	GCCAGACTTTGTTGGATTTG
HRPT1-R	CTCTCATCTTAGGCTTTGTATTTTG
BRN3A-F	GGGCAAGAGCCATCCTTTCAA
BRN3A-R	CTGTTCATCGTGTGGTACGTG
TRKA-F	GCTGGCTCTTCAATGGCTC
TRKA-R	GTGTAGTTGCCGTTGTTGACG
TRKB-F	TCGTGGCATTTCCGAGATTGG
TRKB-R	TCGTCAGTTTGTTTCGGGTAAA
TRKC-F	CTTTGCCCAGCCAAGTGTAGT
TRKC-R	CGTGATGTTGATACTGGCGTT
OCT4-F	CAATTTGCCAAGCTCCTGAAG
OCT4-R	AAAGCGGCAGATGGTCGTT

3.11. Cell Counting

All cell counting for HEK, fibroblast and iPSC experiments was performed with use of Solution 18 AO-DAPI Staining Reagent (Chemometec) and a Chemometec NucleoCounter NC-250™.

3.12. Statistical Analysis

All data are presented as mean ± SEM, unless otherwise stated. Sample sizes are detailed in figure legends. To determine statistical significance, a one-way ANOVA was used to compare the means of two or more independent groups. Statistical significance for all experiments was defined as a p-value < 0.05. All statistical tests were carried out using GraphPad prism data analysis software.

4. Results

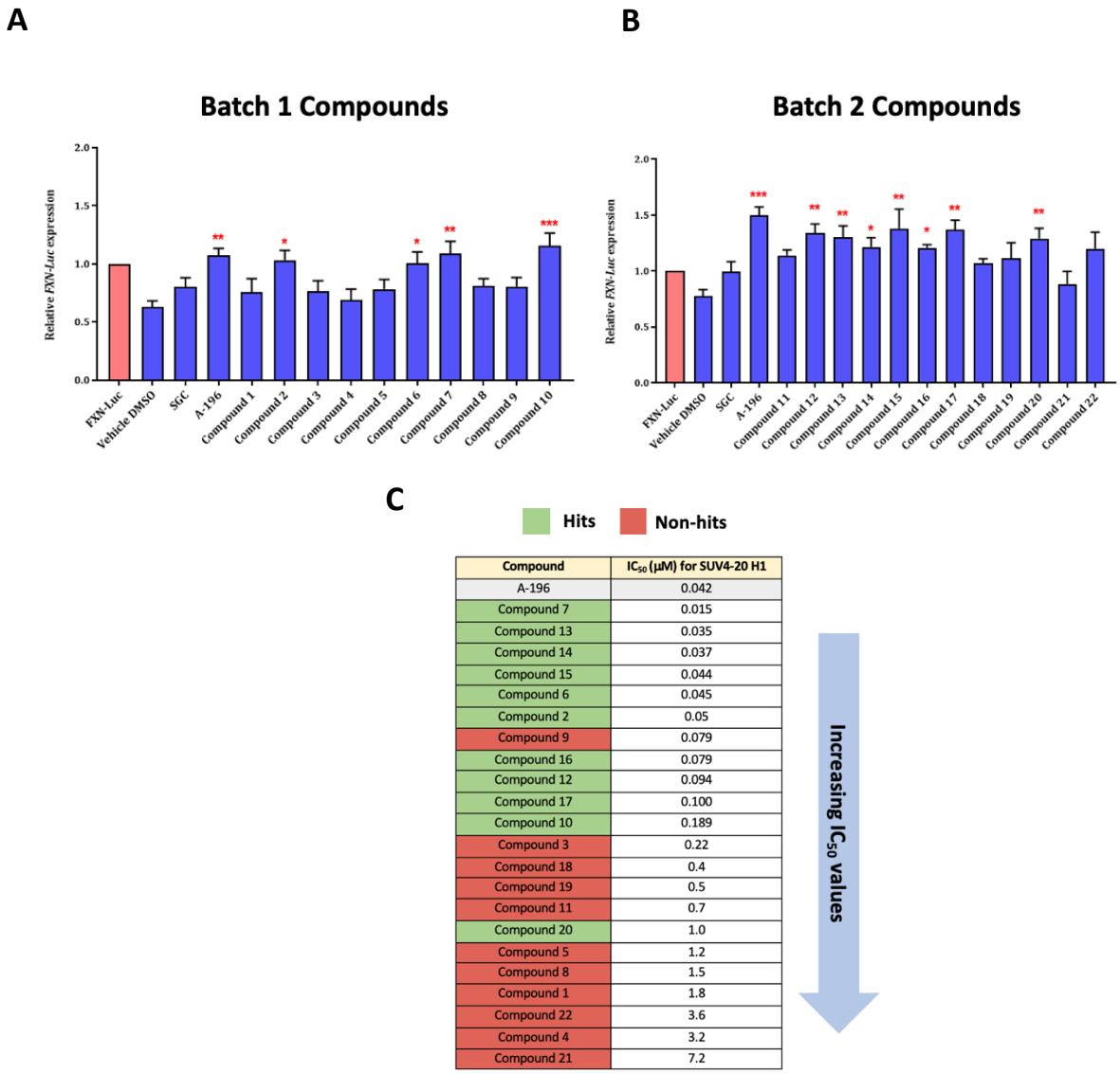
4.1. A-196 Structural Derivatives Increase *FXN* Expression in Cellular Models of FRDA

A-196 is a highly selective substrate-competitive inhibitor of both SUV4-20 H1 and H2 [142]. Prior work published from our laboratory has shown that inhibition of SUV4-20 enzymes with the tool compound A-196, results in a corresponding increase in *FXN* mRNA expression in a number of cellular models of FRDA [90]. Working in collaboration with medicinal chemists from the Oxford Target Discovery Institute, we sought to improve the potency and biostability of A-196 through chemical modification. We were provided with 22 structural derivatives of A-196 in two batches. These compounds possess the same A-196 structural backbone, with slight synthetic modifications made at exploitable chemical sites to increase stability and potentiate improved SUV4-20 inhibition. The first part of my project focused on identifying if any of these A-196 structural analogues were capable of increasing *FXN* expression in cellular models of FRDA, and if so, whether they display improved potency.

4.1.1. Select Structural Analogues of A-196 Increase *FXN* Expression in Initial Screen

The first batch of A-196 derivatives received consisted of 10 compounds, whilst the second batch contained 12 compounds. Compounds were initially screened utilising a *FXN*-GAA-

Luciferase HEK293 reporter cell line carrying the Luciferase gene inserted at the exon 5a region of a pathological 135kb human *FXN* locus. We treated our *FXN*-GAA-Luciferase reporter cell line with A-196 structural derivatives at 5 µM for 6 days before assaying frataxin-luciferase (*FXN*-Luc) protein expression to determine *FXN* expression. An untreated *FXN*-Luc wildtype cell line possessing a non-pathological number of GAA repeats was used as a reference for normal *FXN* levels. This initial screen identified 11 compounds that were capable of significantly increasing *FXN*-Luc expression in comparison to the DMSO (vehicle) control (see **Figures 6A** and **6B**). These 11 compounds were deemed to be "hits" and largely corresponded to the compounds with the greatest chemical potency, displaying the lowest IC_{50} values against SUV4-20 H1 (see **Figure 6C**).



Compound	IC_{50} (μM) for SUV4-20 H1
A-196	0.042
Compound 7	0.015
Compound 13	0.035
Compound 14	0.037
Compound 15	0.044
Compound 6	0.045
Compound 2	0.05
Compound 9	0.079
Compound 16	0.079
Compound 12	0.094
Compound 17	0.100
Compound 10	0.189
Compound 3	0.22
Compound 18	0.4
Compound 19	0.5
Compound 11	0.7
Compound 20	1.0
Compound 5	1.2
Compound 8	1.5
Compound 1	1.8
Compound 22	3.6
Compound 4	3.2
Compound 21	7.2

Figure 6. Initial Screen of A-196 Structural Analogues Identifies 11 Potential Hits

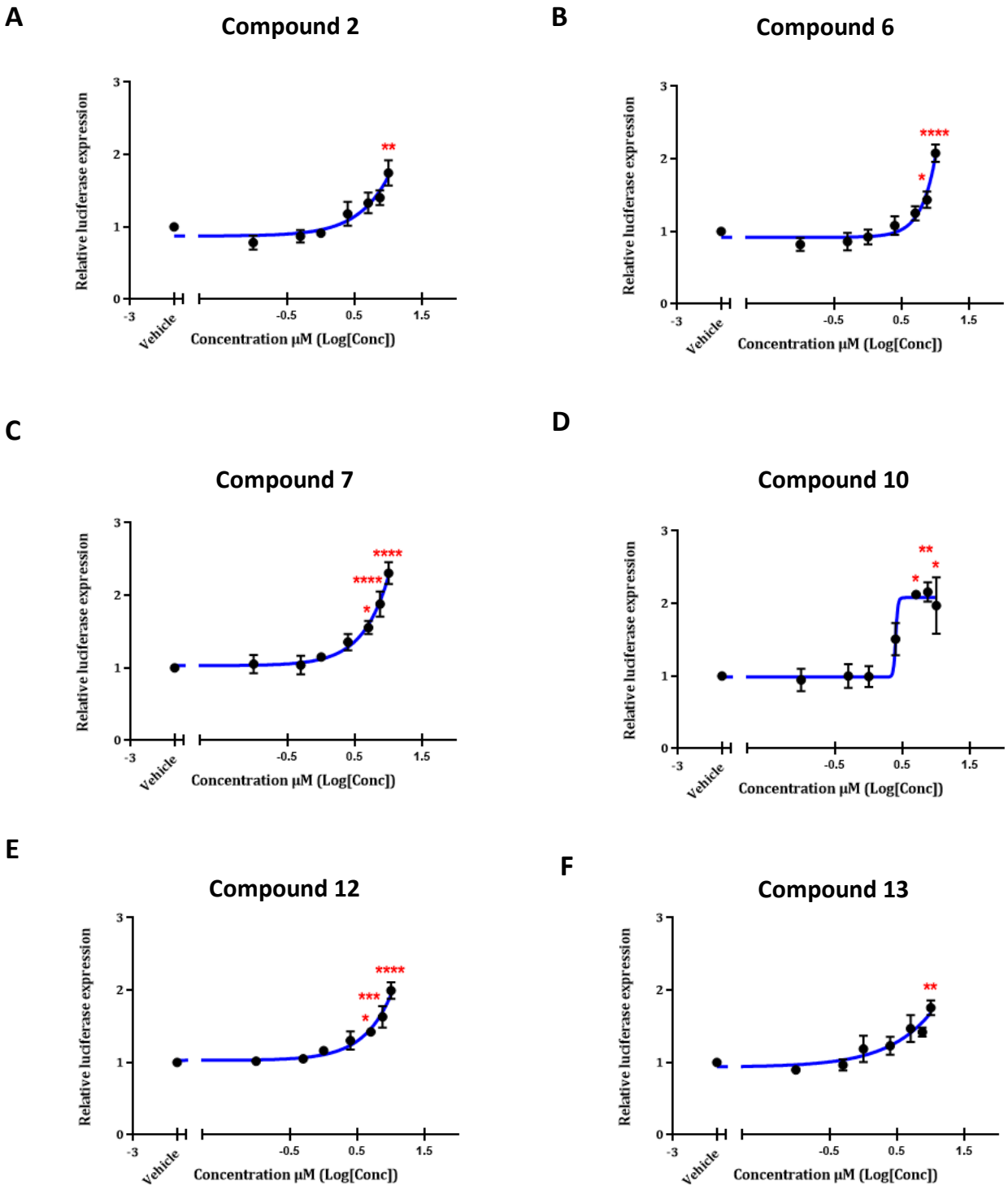
A: Relative *FXN*-Luc expression of *FXN*-GAA reporter cell line treated with batch 1 compounds quantified by luciferase assay. Four structural derivatives significantly increased relative *FXN*-Luc in comparison to the vehicle DMSO control (n= 4 performed in triplicate, one-way ANOVA followed by Bonferroni test). ***B:*** Relative *FXN*-Luc expression of *FXN*-GAA reporter cell line treated with batch 2 compounds quantified by luciferase assay. Seven structural derivatives significantly increased relative *FXN*-Luc in comparison to the vehicle DMSO control (n= 3 performed in triplicate, one-way ANOVA followed by Bonferroni test).

The data for *A* and *B* are represented as means ± SEM and is normalised to the untreated wildtype *FXN*-Luc line. ***C:*** Table detailing structural derivatives received from the chemist sorted by potency. Potential "hit" compounds (shown in green) corresponded largely to be the structural analogues with the lowest IC_{50} values (greatest potency). IC_{50} values were provided by medicinal chemist collaborators and calculated through chemical assay. *, $p < 0.05$; **, $p < 0.01$; ***, $p < 0.001$.

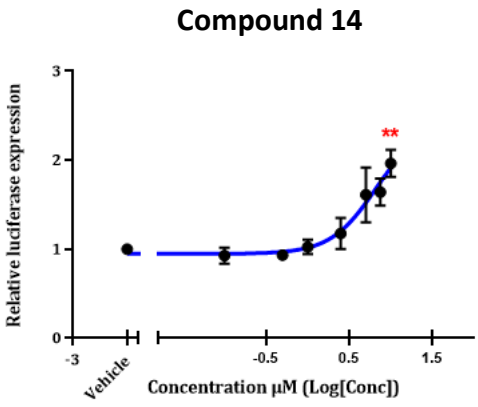
4.1.2. Structural Analogues of A-196 are Validated by Initial Concentration Response Testing

Following identification of potential hit compounds, we next aimed to validate hits with concentration-response data. To do this, we looked to investigate how the expression of the *FXN*-Luc protein in the *FXN*-GAA-Luciferase reporter cell line changed following treatment with an increasing concentration of each structural analogue. Initially, we treated our *FXN*-GAA-Luciferase reporter cell line with the 11 hit compounds at 7 concentrations ranging from 0.1-10 µM (0.1, 0.5, 1, 2.5, 5, 7.5 and 10 µM). *FXN*-Luc protein expression was assayed and concentration-response curves were plotted (see **Figures 7A-M**). A number of structural analogues showed positive responses to concentration-response testing, thus validating their effects. To compare the effectiveness of different structural analogues with one another, we then looked at the concentration of each compound required to achieve a relative 1.7-fold increase in *FXN*-Luc expression in comparison to the DMSO vehicle control (see Figure **7N**). The threshold of 1.7-fold was chosen as it was near the upper-end of expression that we had seen following treatment with A-196 in the reporter cell line, and represented an arbitrary value of expression that

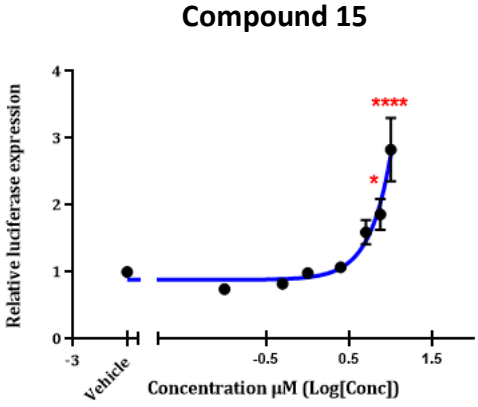
was achieved by most compounds. A total of 8 out of 11 compounds reached 1.7-fold expression, with 3 compounds achieving this expression value at concentrations lower than A-196.



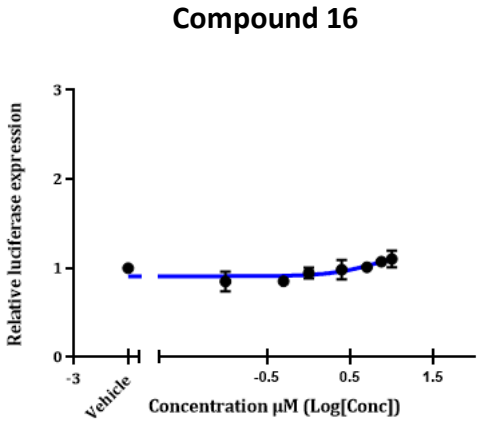
G


Compound 14
Relative luciferase expression
Vehicle
Concentration µM (Log[Conc])
**

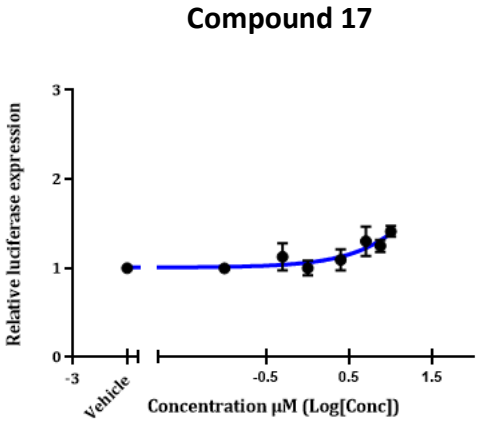
H


Compound 15
Relative luciferase expression
Vehicle
Concentration µM (Log[Conc])
****
*

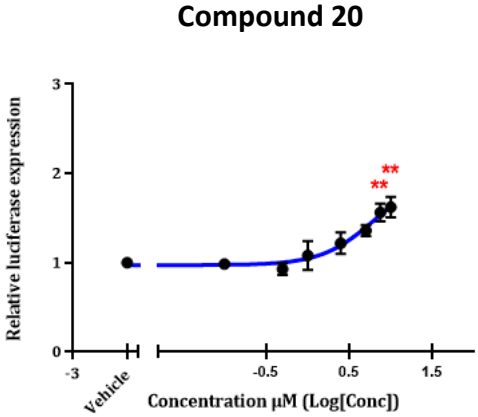
I


Compound 16
Relative luciferase expression
Vehicle
Concentration µM (Log[Conc])

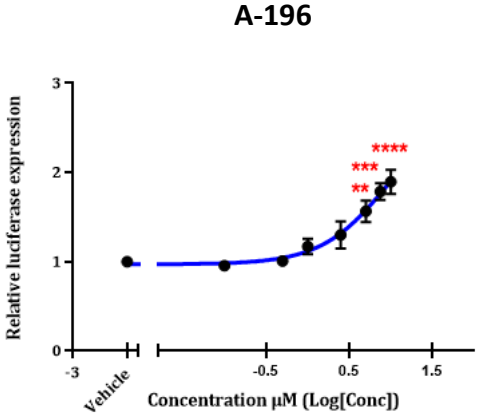
J


Compound 17
Relative luciferase expression
Vehicle
Concentration µM (Log[Conc])

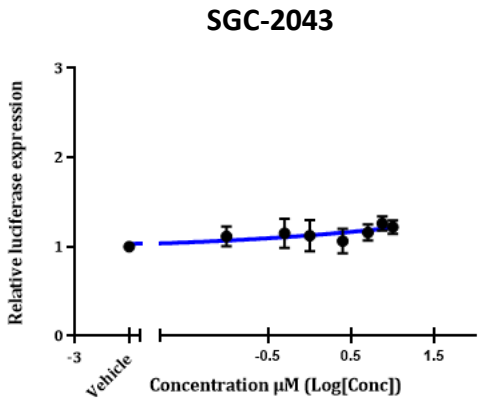
K


Compound 20
Relative luciferase expression
Vehicle
Concentration µM (Log[Conc])
**
**

L


A-196
Relative luciferase expression
Vehicle
Concentration µM (Log[Conc])
****
***
**

M



N

Compound	Concentration Required to Attain 1.7-Fold Expression (µM)
A-196	6.53
Compound 2	9.96
Compound 6	8.37
Compound 7	5.81
Compound 10	2.57
Compound 12	7.48
Compound 13	10.20
Compound 14	6.82
Compound 15	6.12
Compound 16	Did not reach
Compound 17	Did not reach
Compound 20	Did not reach

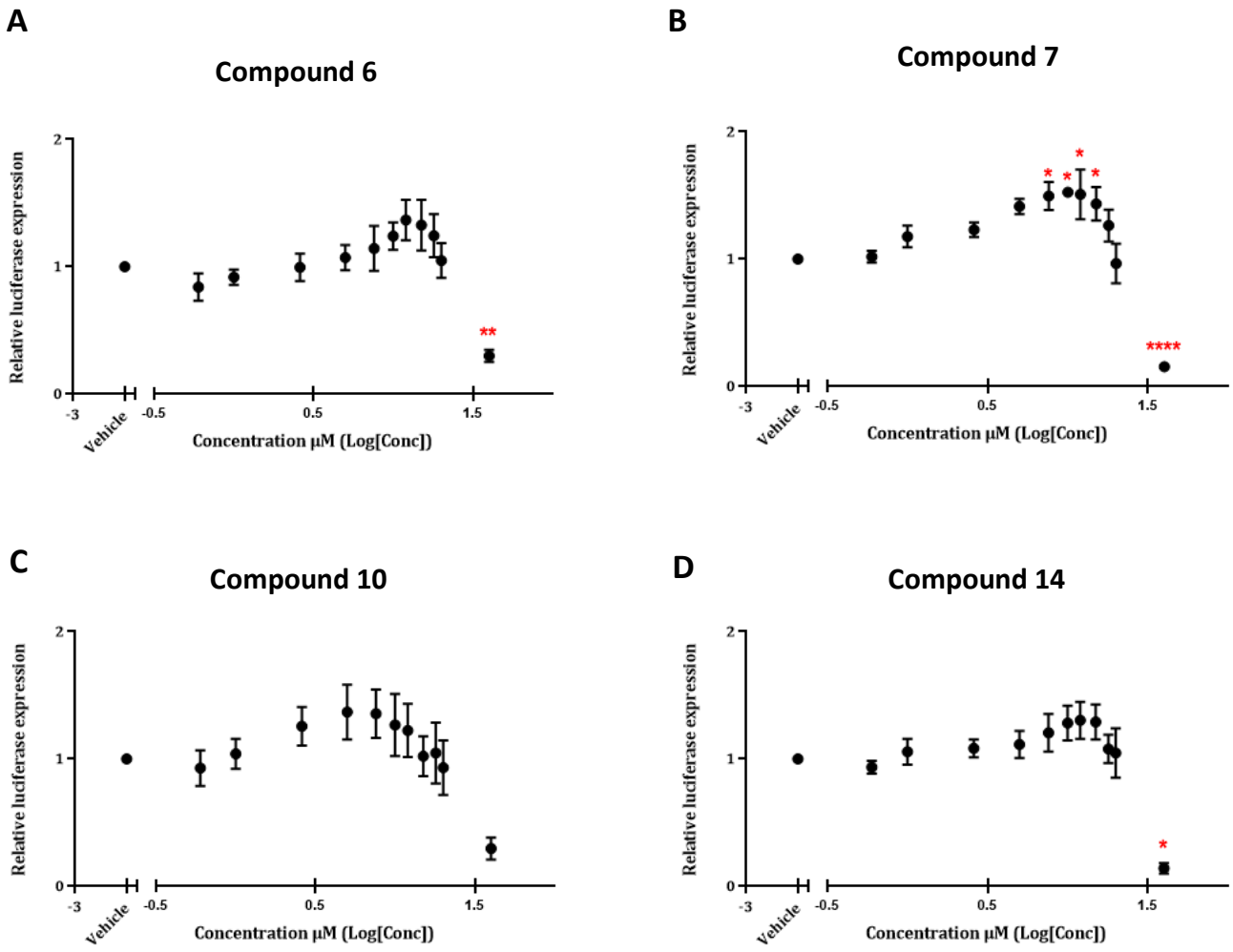
Figure 7. Several Potential Hits are Validated by Concentration Response Testing

A-M: Concentration-response curves obtained by luciferase assay of the *FXN*-GAA reporter cell line treated for 6 days with each of the 11 hit compounds at 7 concentrations ranging from 0.1-10 µM. Several structural analogues were validated by displaying an increase in relative *FXN*-Luc expression with increasing concentration of treatment. (n= 3 performed in triplicate, one-way ANOVA followed by Dunnett's test). The data are all represented as means ± SEM and is normalised to the vehicle DMSO. (*A*, compound 2; *B*, compound 6; *C*, compound 7; *D*, compound 10; *E*, compound 12; *F*, compound 13; *G*, compound 14; *H*, compound 15; I, compound 16; J, compound 17; K, compound 20; L, A-196; M, SGC-2043) ***N:*** Table detailing concentration of each structural derivative required to achieve a relative 1.7-fold expression in comparison to the DMSO vehicle control. Eight out of 11 compounds tested reached a relative 1.7-fold expression, with 3 compounds achieving this expression value at a concentration lower than required by A-196. *, $p < 0.05$; **, $p < 0.01$; ***, $p < 0.001$; ****, $p < 0.0001$.

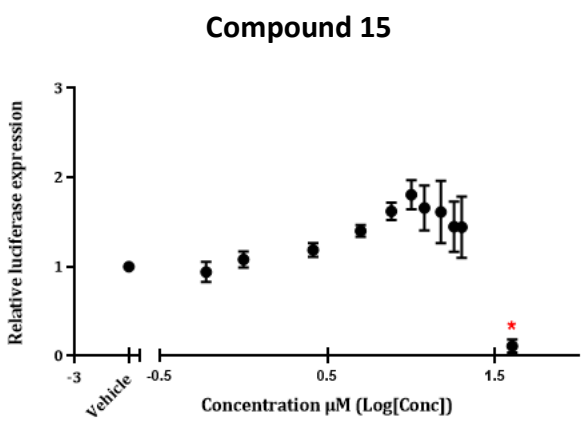
4.1.3. Structural Analogues Display Confirmed Toxicity at Higher Concentrations

The concentration-response curves for a number of structural analogues appeared to show an increasing trend in their ability to increase *FXN* expression as concentrations increased beyond 10 µM. For this reason, we then performed a second broader-range concentration-response screen of the 5 most promising structural analogues, in order to access whether increasing their concentration above 10 µM results in further significant increases in *FXN* expression. For the broader-range screen, we treated our reporter cell line with 5 structural analogues at 11 concentrations ranging from 0.6-40 µM (0.6, 1, 2.6, 5, 7.6, 10, 12, 15, 18, 20 and 40 µM). *FXN*-Luc protein expression was assayed and concentration-

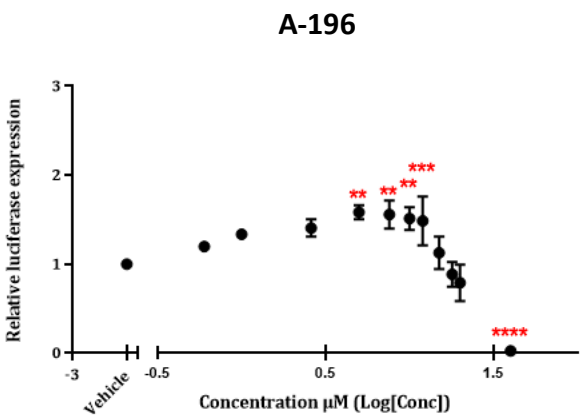
response curves were plotted (see **Figure 8A-G**). The 5 structural analogues tested were selected based on data from the initial concentration-response screen. As expected, our results showed that the trend of increasing *FXN* expression did not increase much further than 10 µM, with expression rapidly decreasing at higher concentrations. Additionally, images were taken of the wells containing cells treated with the structural analogues for the 2nd concentration-response screen at 10 and 40 µM (see Figure **8H-L**). The images largely show that wells treated with compounds at 10 µM contained densely populated and healthy-looking cells with normal morphology. However, wells that were treated at 40 µM had sparse (if any) cells, with clear signs of toxicity and cell death.



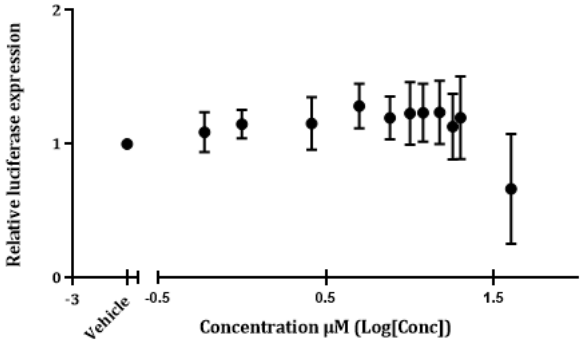
E



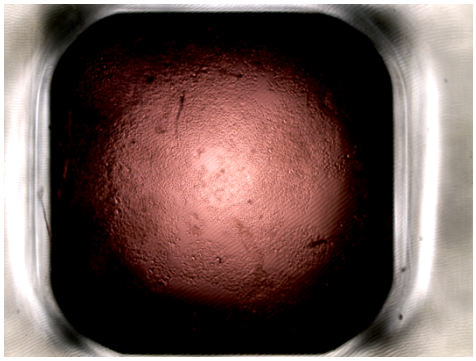
F



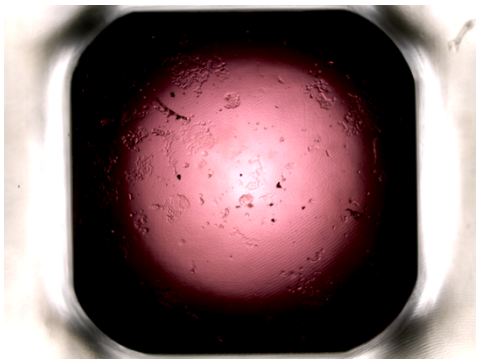
G



H

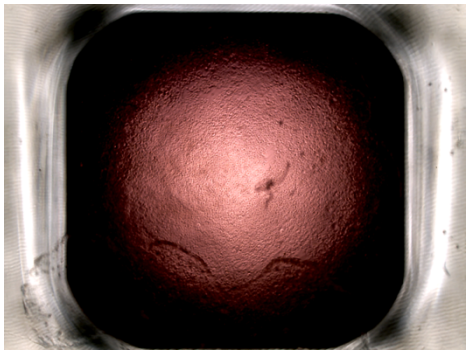


Compound 6 (10 µM)

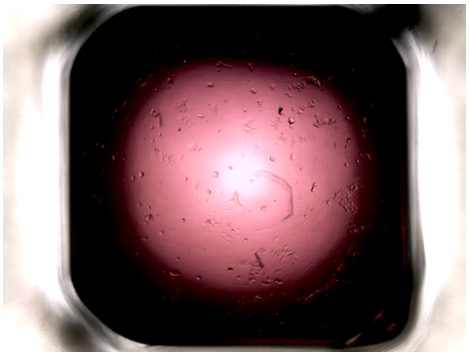


Compound 6 (40 µM)

I

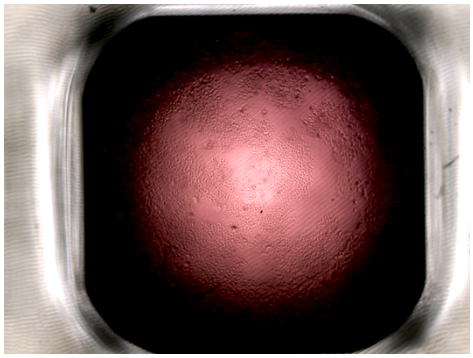


Compound 7 (10 µM)

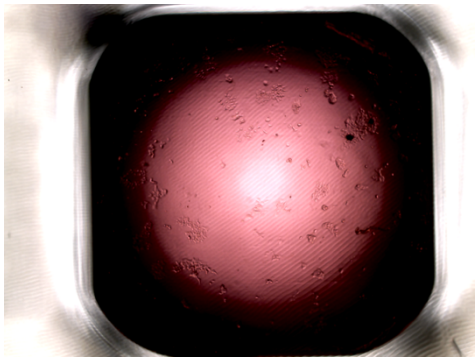


Compound 7 (40 µM)

J

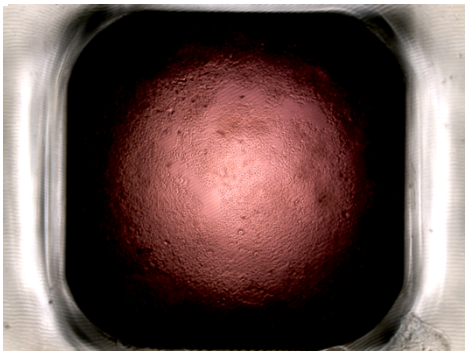


Compound 10 (10 µM)

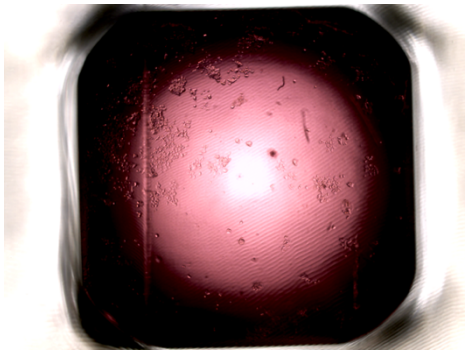


Compound 10 (40 µM)

K

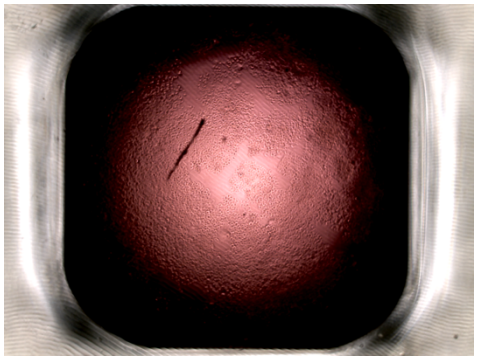


Compound 14 (10 µM)

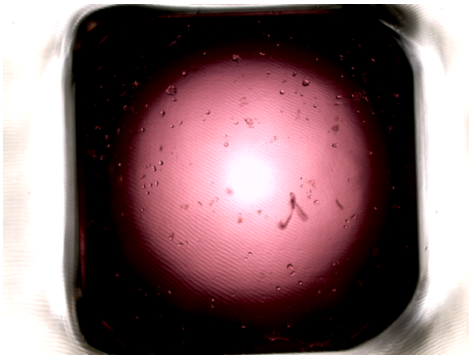


Compound 14 (40 µM)

L



Compound 15 (10 µM)



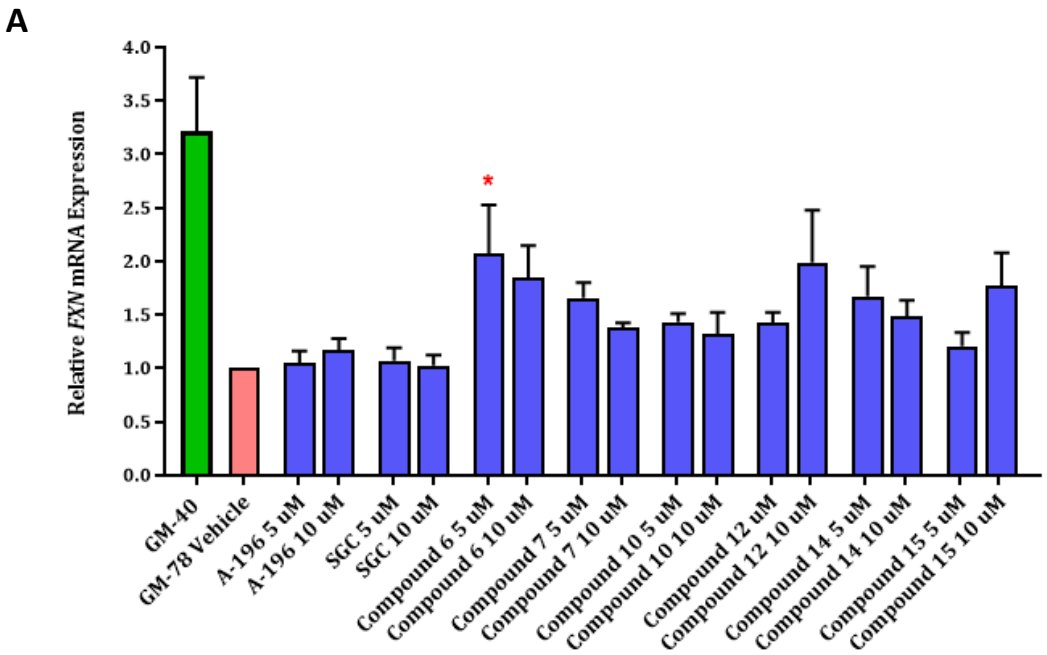
Compound 15 (40 µM)

Figure 8. Structural Analogues Display Signs of Toxicity at High Concentrations

A-G: Second-round of concentration-response curves obtained by luciferase assay of the *FXN*-GAA reporter cell line treated for 6 days with the selected 5 hit compounds at 11 concentrations ranging from 0.6-40 µM. Relative *FXN*-Luc expression is seen to fall for all structural derivatives at the highest concentrations of treatment (n= 3 performed in triplicate, one-way ANOVA followed by Dunnett's test). The data is all represented as means ± SEM and is normalised to the vehicle DMSO. (*A*, compound 6; *B*, compound 7; *C*, compound 10; *D*, compound 14; *E*, compound 15). ***H-L:*** Images of wells containing cells following treatment with structural analogues at 10 or 40 uM for the broader range concentration-response screen. Wells which contained cells treated at 40 uM show clear indications of toxicity in contrast to cells treated at 10 uM. All images were taken at 5X. (*H*, compound 6; *I*, compound 7; *J*, compound 10; *K*, compound 14; *L*, compound 15). *, $p < 0.05$; **, $p < 0.01$; ***, $p < 0.001$; ****, $p < 0.0001$.

4.1.4. Structural Analogues Potentially Increase *FXN* Expression in FRDA Patient-Derived Fibroblasts

Following concentration-response testing to validate potential hits in our reporter cell line, we then progressed to testing select structural analogues in two FRDA patient-derived primary fibroblast lines. We treated the primary patient fibroblast lines GM4078 and GM3816 with the 6 most promising structural analogues (selected from concentration-response data) at 2 concentrations, 5 and 10 µM, before assessing *FXN* mRNA expression via RNA extraction and RT-qPCR. For the GM4078 line, we found a trend of increased *FXN* mRNA expression in comparison to the vehicle DMSO, following treatment with several structural analogues. This increase in *FXN* mRNA expression was statistically significant for only one compound, drug 6 (see **Figure 9A**). The GM3816 line was less responsive to treatment, with no significant increases in FXN mRNA expression seen following treatment with any of the structural analogues (see **Figure 9B**).



B

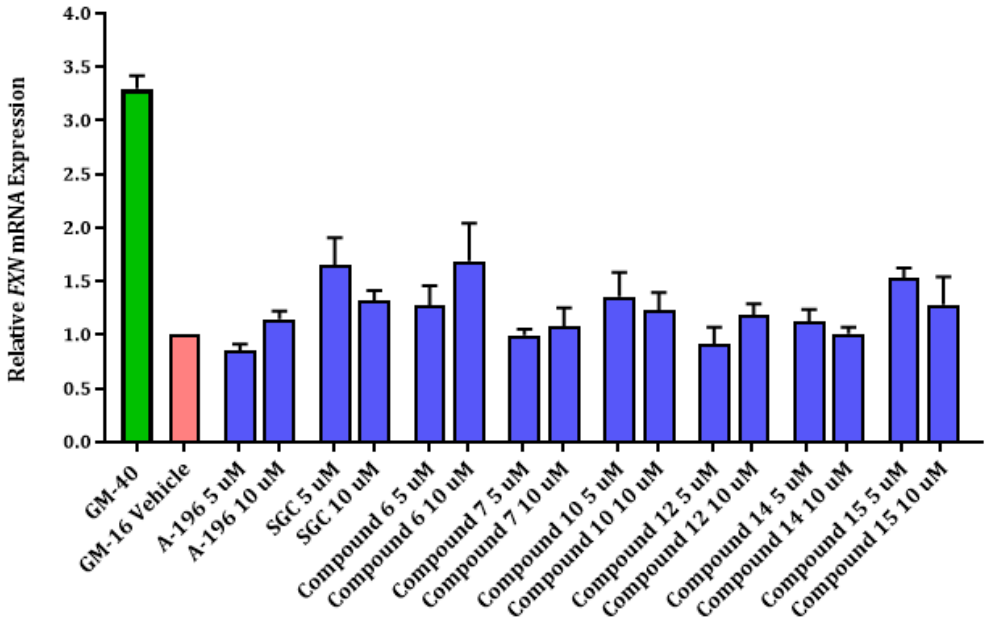


Figure 9. FRDA Patient-Derived Fibroblasts Treated with A-196 Structural Analogues

A: Relative FXN mRNA expression in FRDA patient-derived primary fibroblast line GM4078 following treatment with structural analogues at 5 and 10 uM. Compound 6 was shown to significantly increase relative *FXN* mRNA expression in comparison to the DMSO vehicle control. (n= 3, other than compound 10 (5 µM) and compound 12 (5 and 10 µM), where n=2, one-way ANOVA followed by Dunnett's test). ***B:*** Relative *FXN* mRNA expression in FRDA patient-derived primary fibroblast line GM4016 following treatment with structural analogues at 5 and 10 µM. No compounds were shown to significantly increase relative *FXN* mRNA expression in comparison to the DMSO vehicle control. (n= 3, other than compound 10 (5 µM) and compound 12 (5 and 10 uM), where n=2, one-way ANOVA followed by Dunnett's test). *, $p < 0.05$.

4.2. Establishing an iPSC-derived Sensory Neuronal Model of FRDA

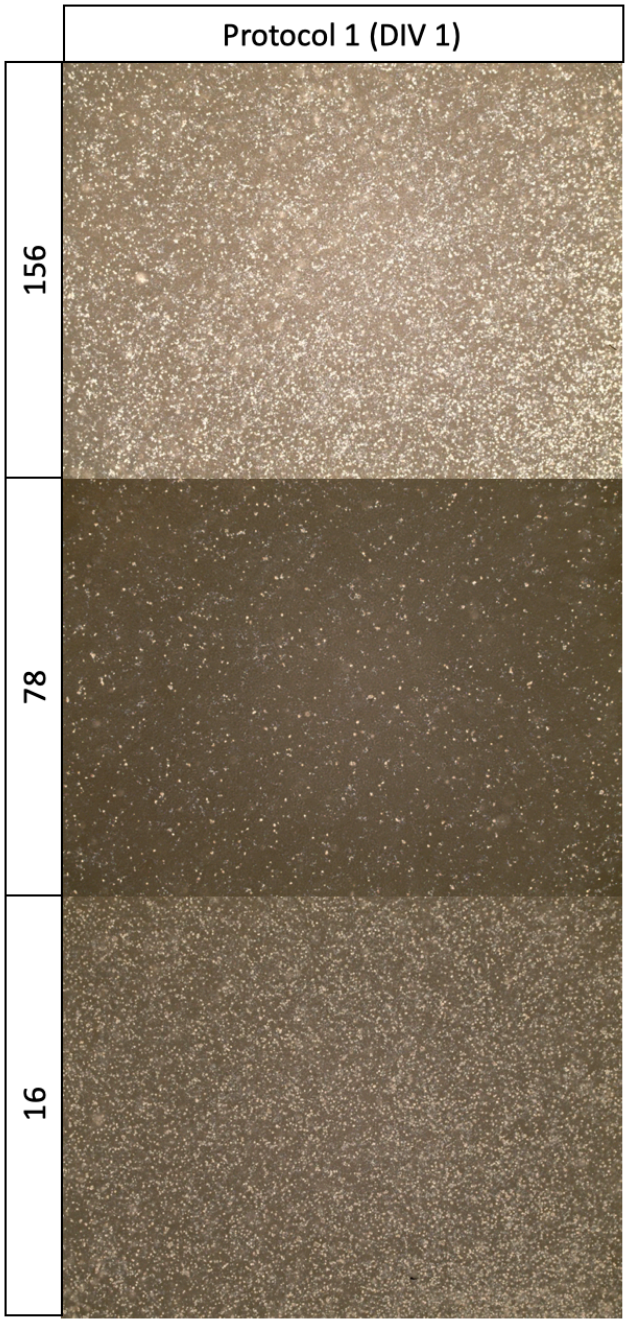
The second aim of this project was to establish an iPSC-derived sensory neuronal model of FRDA. This was achieved by utilising several well characterised control iPSC lines, alongside one previously characterised FRDA line (iPSC3816) [153] and another FRDA line still to be fully characterised (iPSC4078). We followed two previously published differentiation protocols for the generation of sensory neurons from these iPSCs. Protocol 1 describes a method to generate non-specific populations of PSNs, composed predominately of nociceptors, [157] whilst protocol 2 claims to generate PSN cultures enriched for proprioceptors [158] (see **Figure 5** for a summary of both protocols). For this project, we performed a total of three differentiations, optimising the process with each step. All the data presented were derived from the 3rd and final differentiation unless otherwise stated.

4.2.1. iPSCs Exhibit Clear Morphological Changes During Neurogenesis

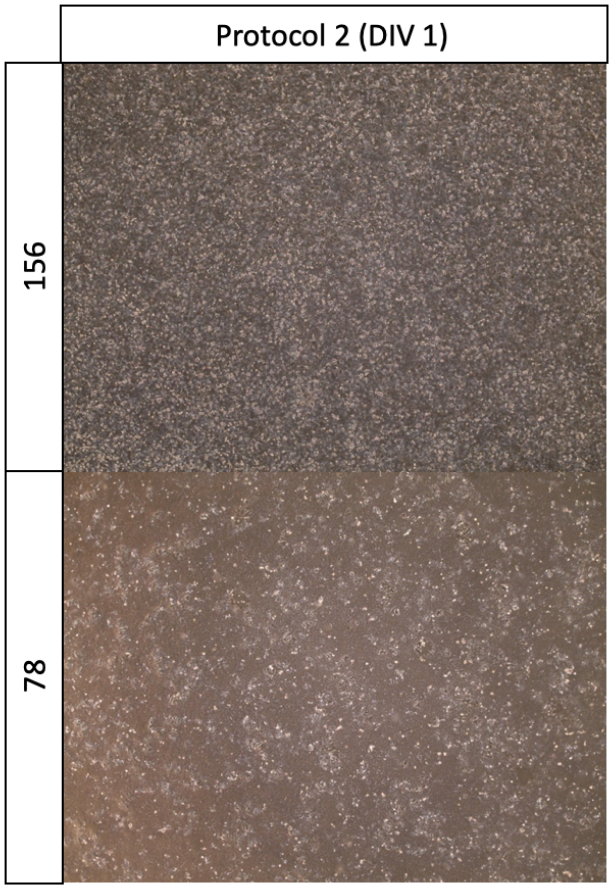
Prior to their differentiation, iPSCs were maintained in mTeSR1 basal culture medium, before the commencement of neurogenesis by the addition of small molecules and a change of culture medium. Both protocols lasted a total of 25 days, with images of the cells taken daily to monitor changes in morphology during the process. Figure 10 shows images of the cells taken on days 1, replating, 15, 20 and 25 for each protocol. The control iPSC line (SFC156-03-01) and two FRDA lines (iPSC4078 and iPSC3816) were used for the 3rd differentiation. The FRDA line iPSC3816 did not survive treatment with protocol 2 and thus no data is available for this line in relation to the 2nd protocol.

Initially, cells demonstrated clear signs of iPSC morphology, proliferating rapidly as a uniform and largely confluent layer (see **Figure 10A**). These iPSCs eventually began to exhibit properties representative of neural precursors, prior to their replating on day 9 (protocol 2) and day 12 (protocol 1) (see **Figure 10B**). Following replating, precursors were then treated with various neurotrophic factors, initiating a process of rapid adult neurogenesis, evidenced by clear morphological changes and obvious neurite formation (seen by day 15) (see **Figure 10C**). As they matured, neurons began clustering together, with their projections becoming elongated and denser. It was observed that by the final stages of the differentiation, protocol 2 tended to result in the generation of neurons which were slightly more representative of a pseudo-unipolar phenotype (see **Figures 10D-E**).

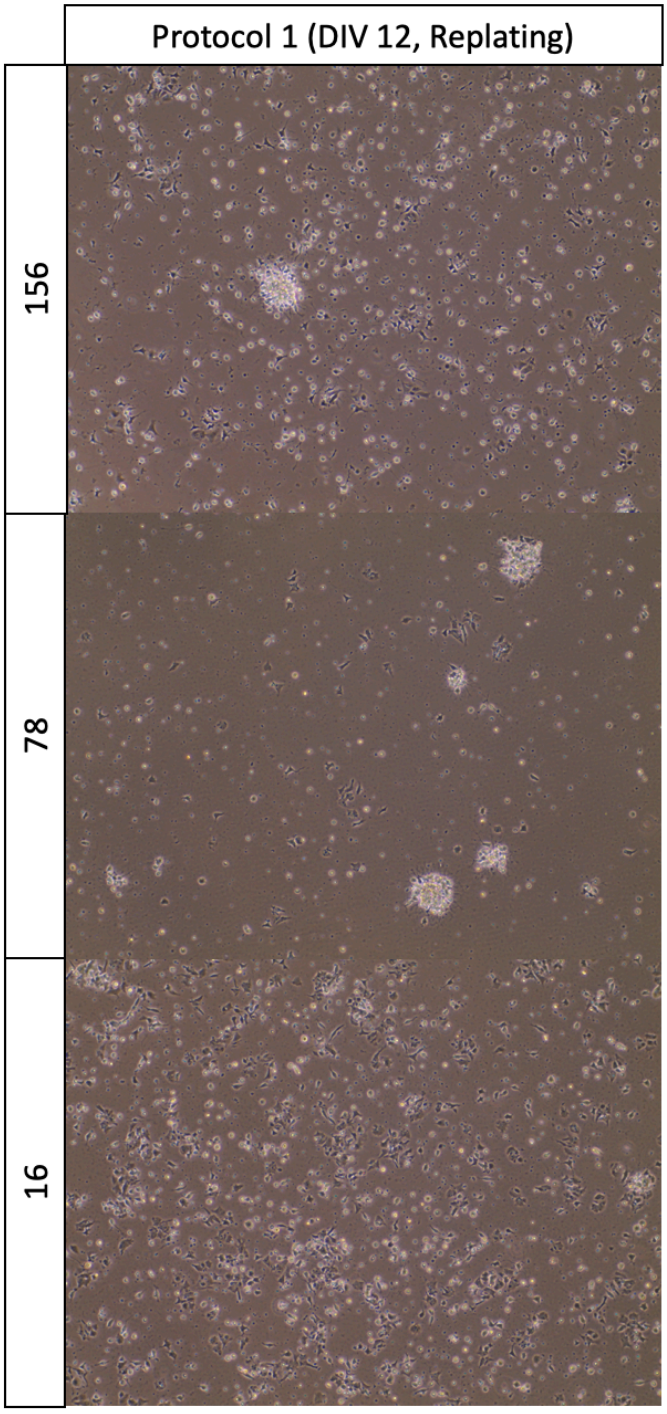
A



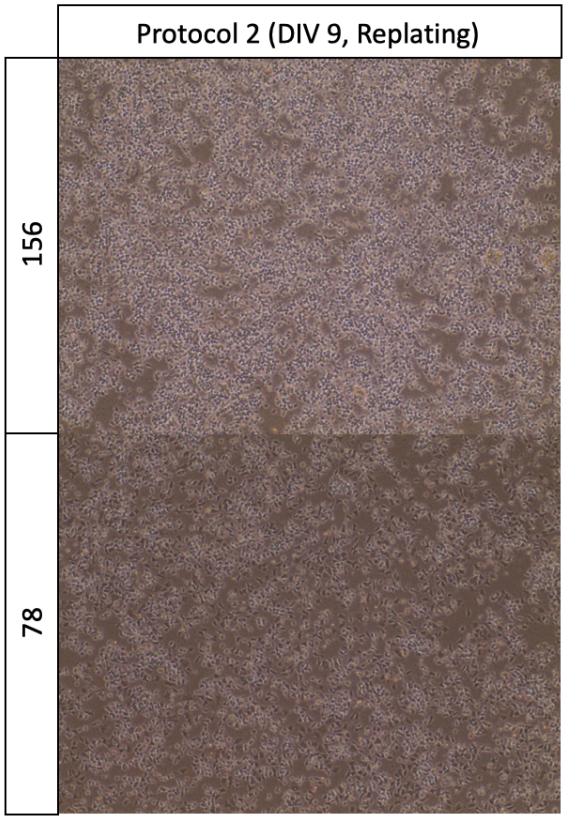
B



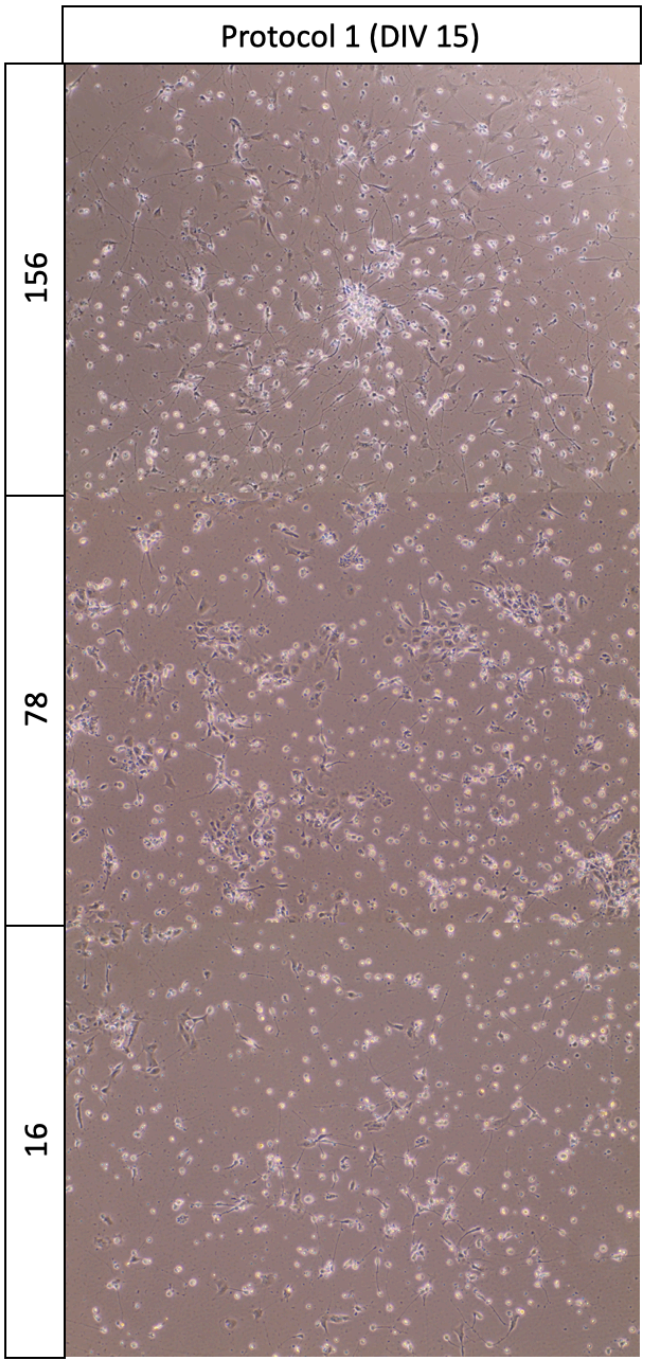
C


Protocol 1 (DIV 12, Replating)
156
78
16

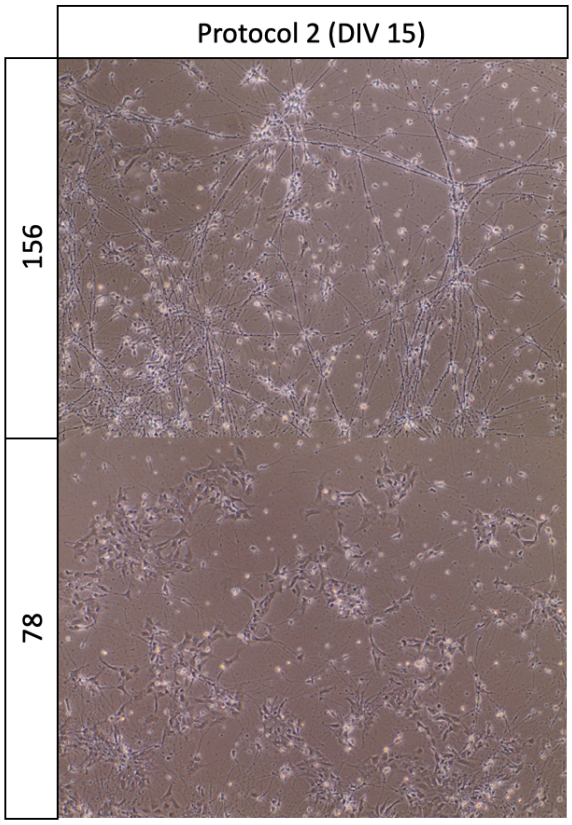
D


Protocol 2 (DIV 9, Replating)
156
78

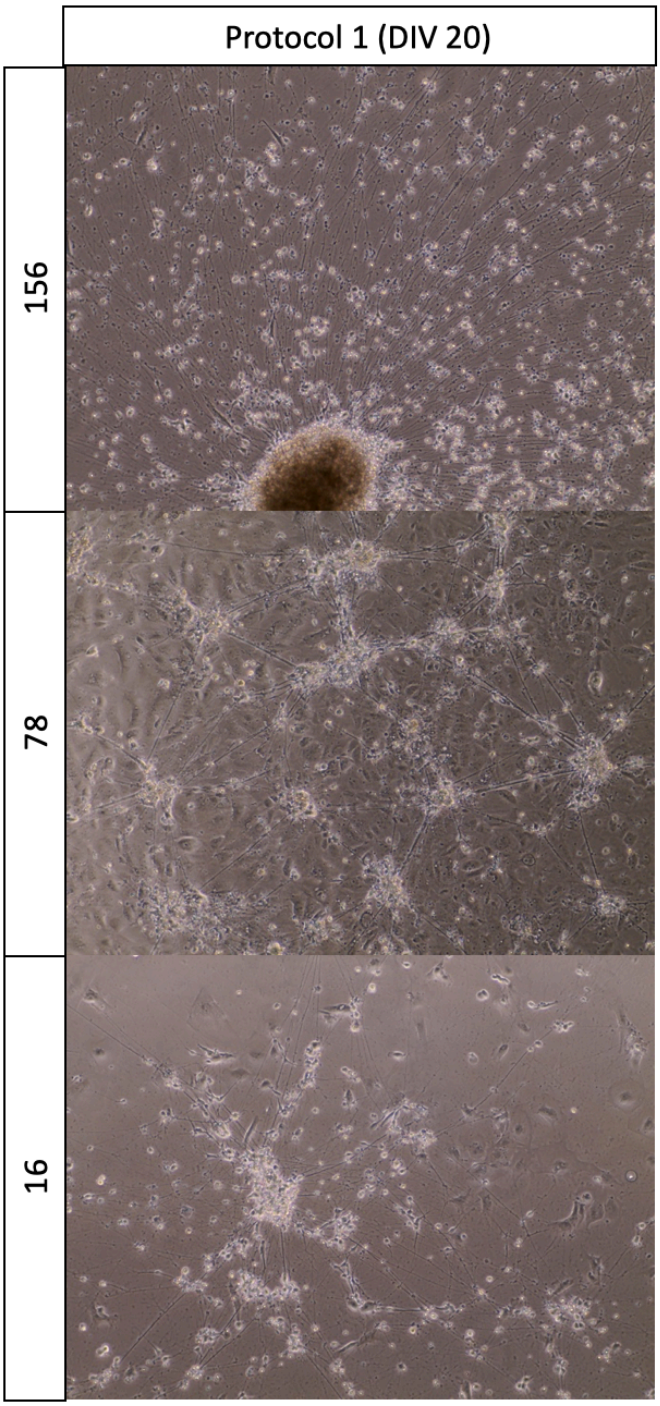
E



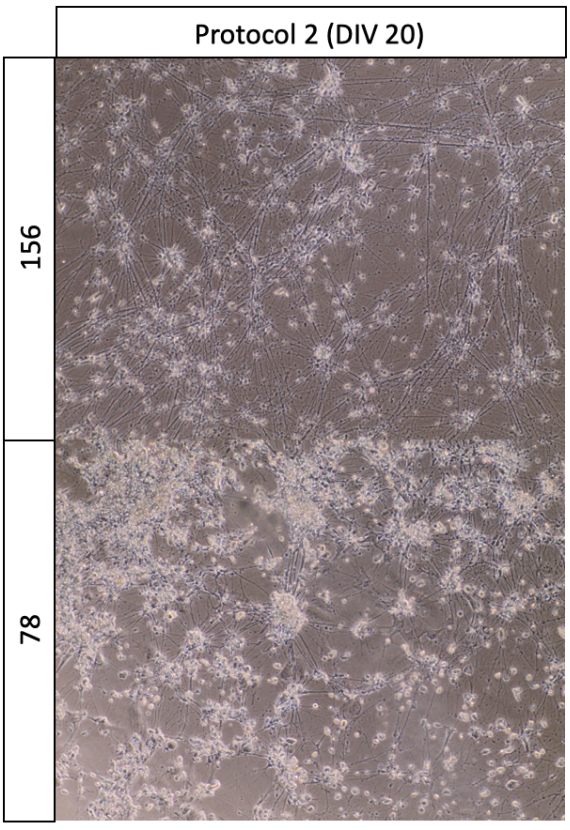
F



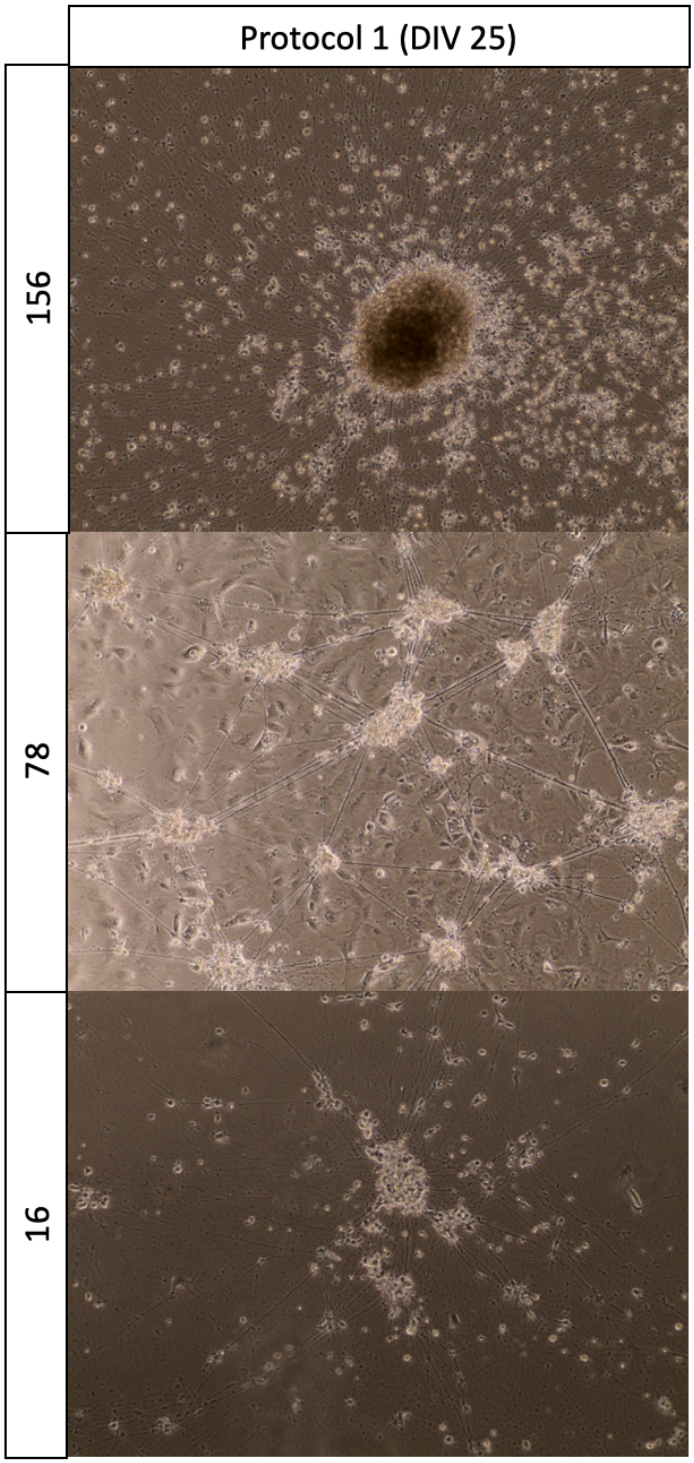
G



H



I



J

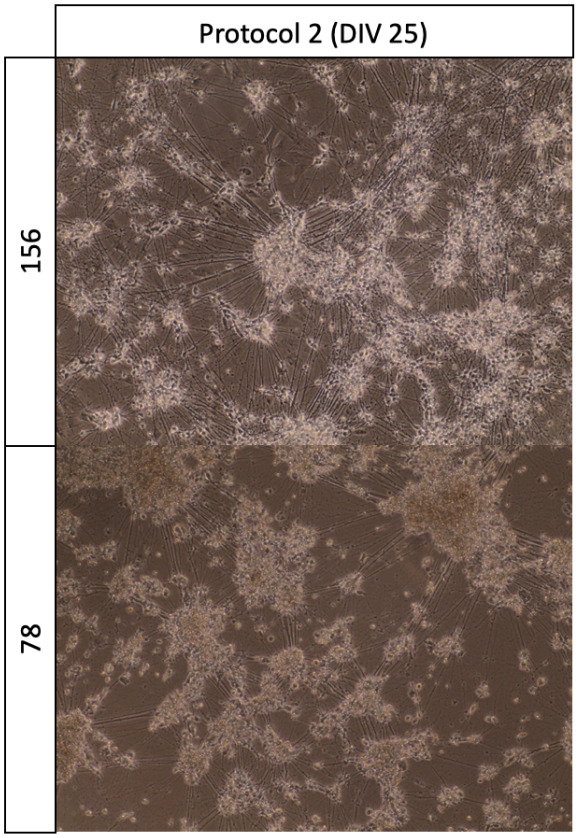


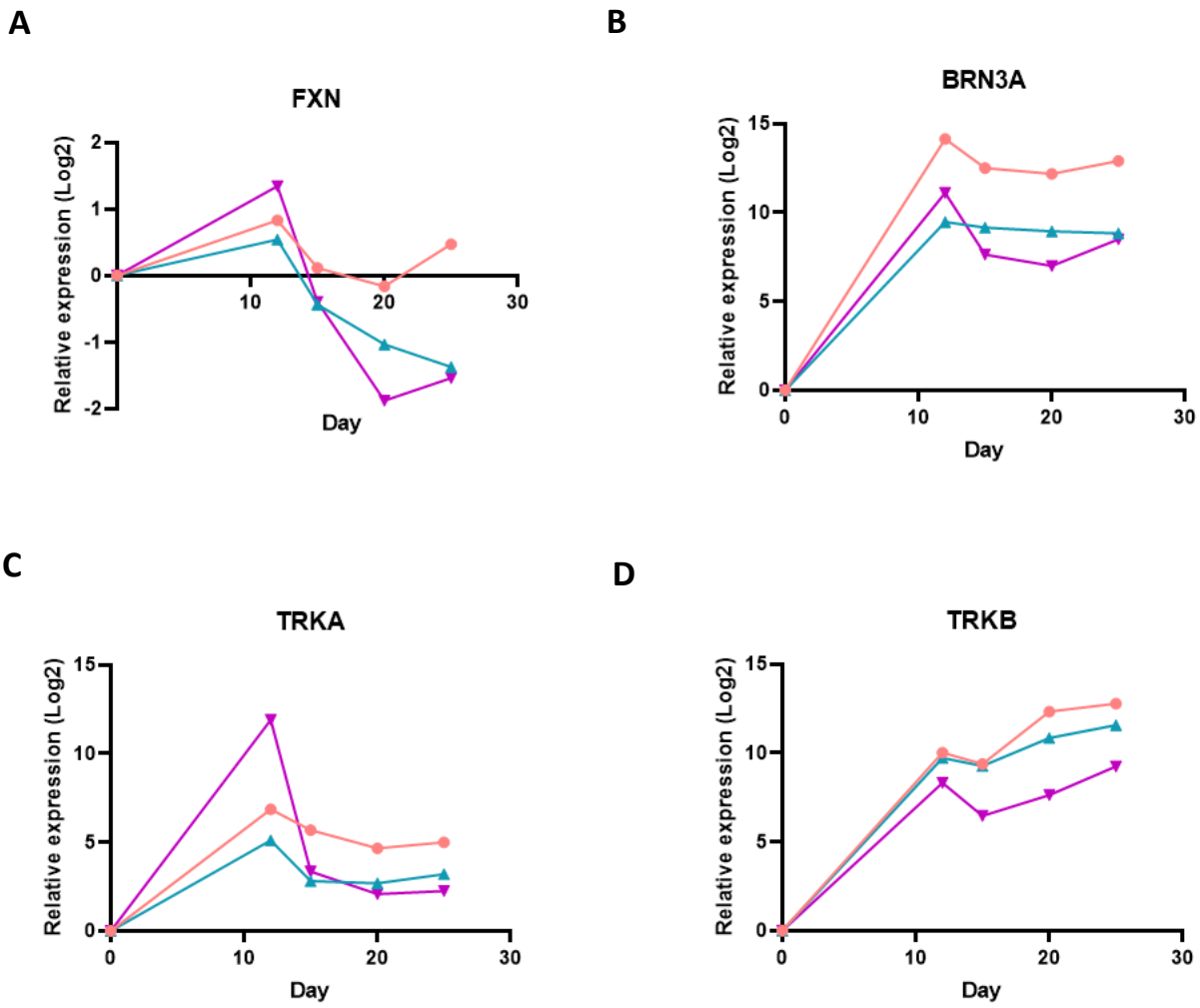
Figure 10: Morphological Changes Observable During Differentiation Process

Phase-contrast microscopy images of cells at various timepoints during the differentiation process. Clear signs of neuronal morphology and maturation are visible in the images following replating days (A-B, day 1; C, day 12; D, day 9; E-F, day 15; G-H, day 20; I-J, day 25). All images were taken from the 3rd differentiation and are at 10X. DIV: days *in vitro*

4.2.2. Cells Exhibit Sensory Neuronal Gene Expression Profiles During Differentiation

In addition to monitoring morphological changes of cells via imaging, the expression profiles of several key genes during the differentiation process was established by qRT-PCR. Cells were taken at the iPSC stage, replating days and days 15, 20 and 25 for analysis. The expression of *FXN*, alongside various sensory neuronal markers and transcription factors, was determined and graphed during the course of the differentiation (see **Figures 11 and 12**). For protocol 1, *FXN* expression was seen to be reduced in both FRDA patient lines compared to the control for all but one timepoint investigated (day 12, iPSC4078 line) (see **Figure 11A**). The iPSC4078 FRDA line also showed a greater *FXN* expression in comparison to the control for 2 timepoints when treated with protocol 2 (see **Figure 12A**). For both protocols, the expression of the pluripotent marker *OCT4* was seen to rapidly decline for all cell lines throughout the differentiation process, indicating a loss of pluripotency and the generation of mature cell types (see **Figures 11F and 12F**). Expression

of the pan-sensory neuronal marker *BRN3A* was strongly induced early on in the differentiation, before its levels plateaued surrounding the replating days (see **Figures 11B and 12B**). The observed rapid expression of the Trk receptors signposted the final stages of sensory neurogenesis. For protocol 1, expression of nociceptive-marker *TRKA* peaked at day 12 (replating day), before levels decreased. This was coupled with a mostly sustained increase in expression of the mechanoreceptive-marker *TRKB* and the proprioceptive-marker *TRKC* into the late stages of differentiation (see **Figure 11C-E**). A greater expression of *TRKB* and *TRKC* in comparison to *TRKA* during the final stages of differentiation was also observed for protocol 2 (see **Figure 12C-E**).



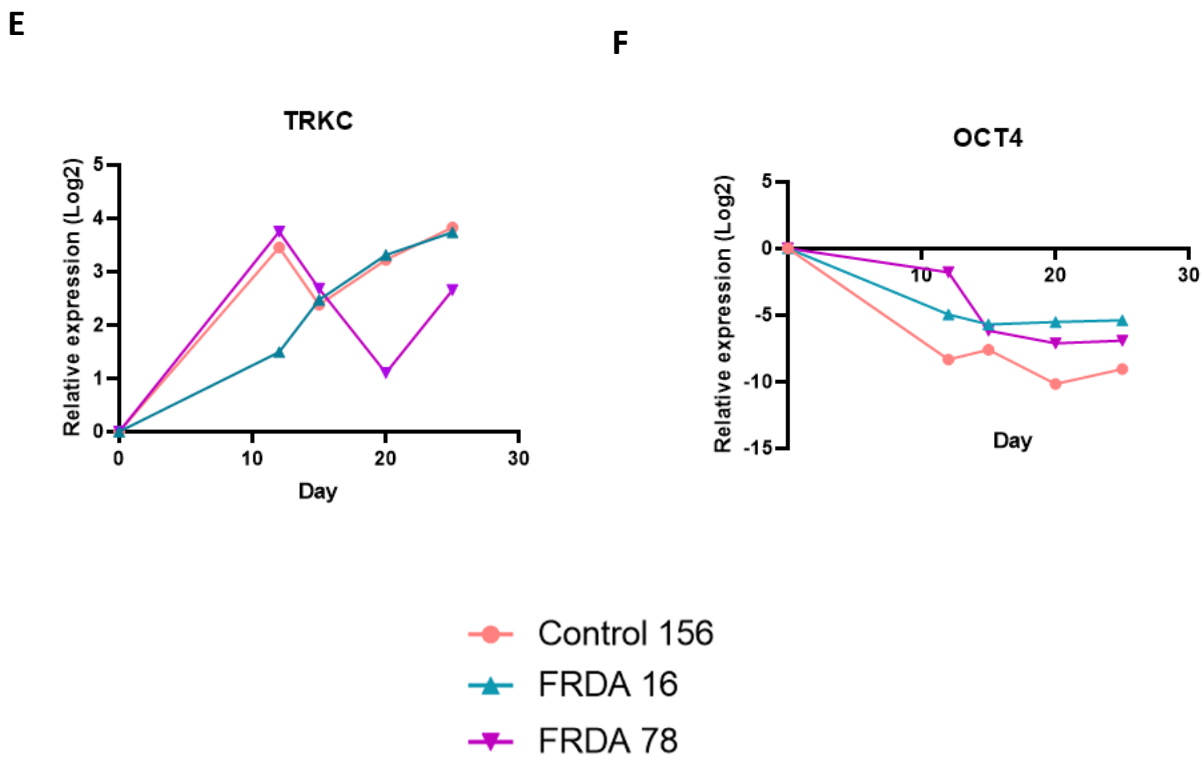


Figure 11: Gene Expression Profiles of Cells Treated with Protocol 1

Time course of gene expression profiles for several markers in control line SFC156-03-01 (control 156) and FRDA lines iPSC3816 (FRDA 16) and iPSC4078 (FRDA 78) treated with protocol 1. Several markers show significant changes in levels of their expression during the differentiation time course (A, FXN; B, BRN3A; C, TRKA; D, TRKB; E, TRKC; F, OCT4). Expression (log2 scale) is shown on the y-axis with the time course of the differentiation on the x-axis. All expression values are relative to day 0 (iPSC stage). mRNA expression was determined by RT-PCR. All expression profiles were derived from the 3rd differentiation.

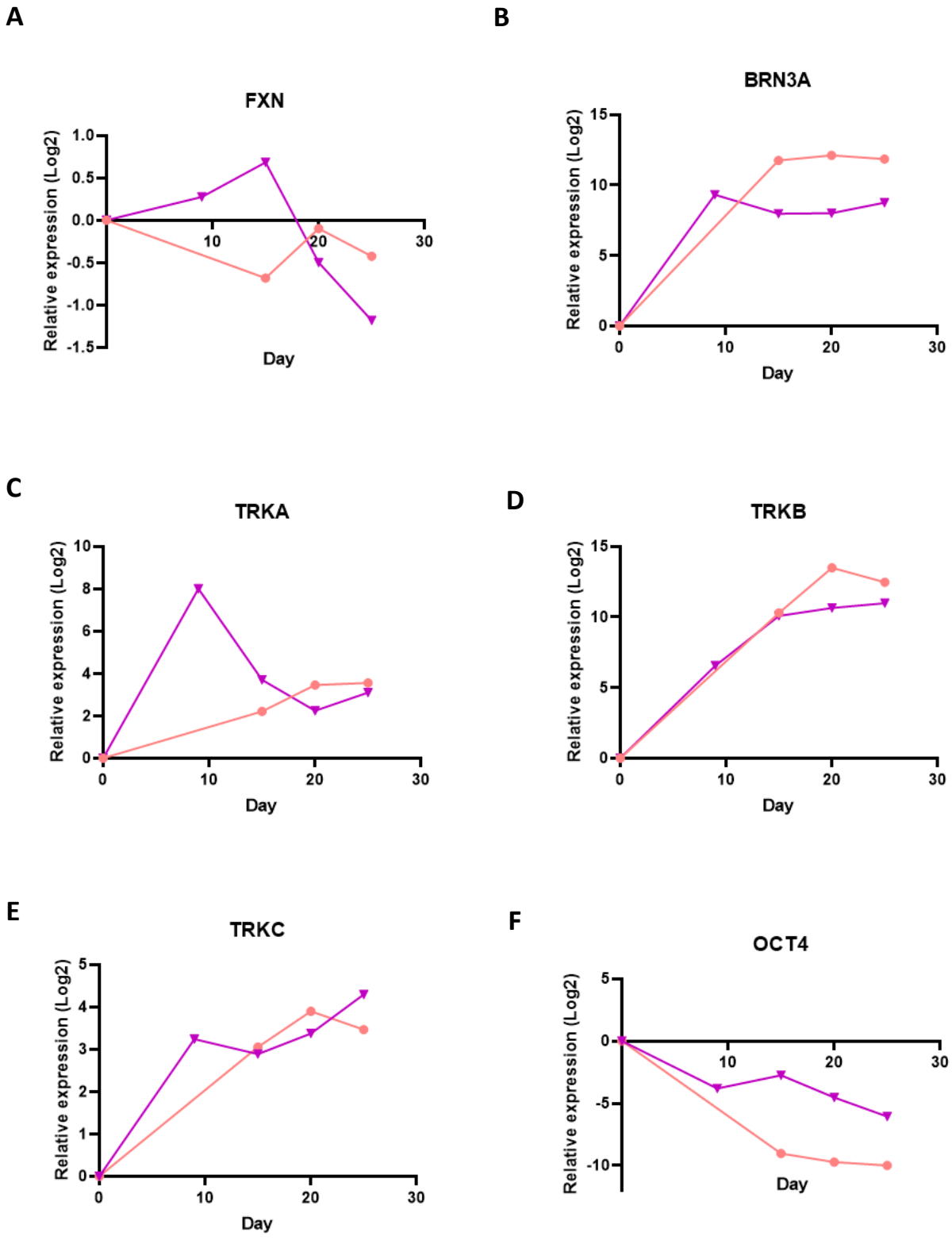

A
FXN
Relative expression (Log2)
1.0
0.5
0.0
-0.5
-1.0
-1.5
10
20
30
Day
B
BRN3A
Relative expression (Log2)
15
10
5
0
0
10
20
30
Day
C
TRKA
Relative expression (Log2)
10
8
6
4
2
0
0
10
20
30
Day
D
TRKB
Relative expression (Log2)
15
10
5
0
0
10
20
30
Day
E
TRKC
Relative expression (Log2)
5
4
3
2
1
0
0
10
20
30
Day
F
OCT4
Relative expression (Log2)
5
0
-5
-10
10
20
30
Day
Control 156
FRDA 78

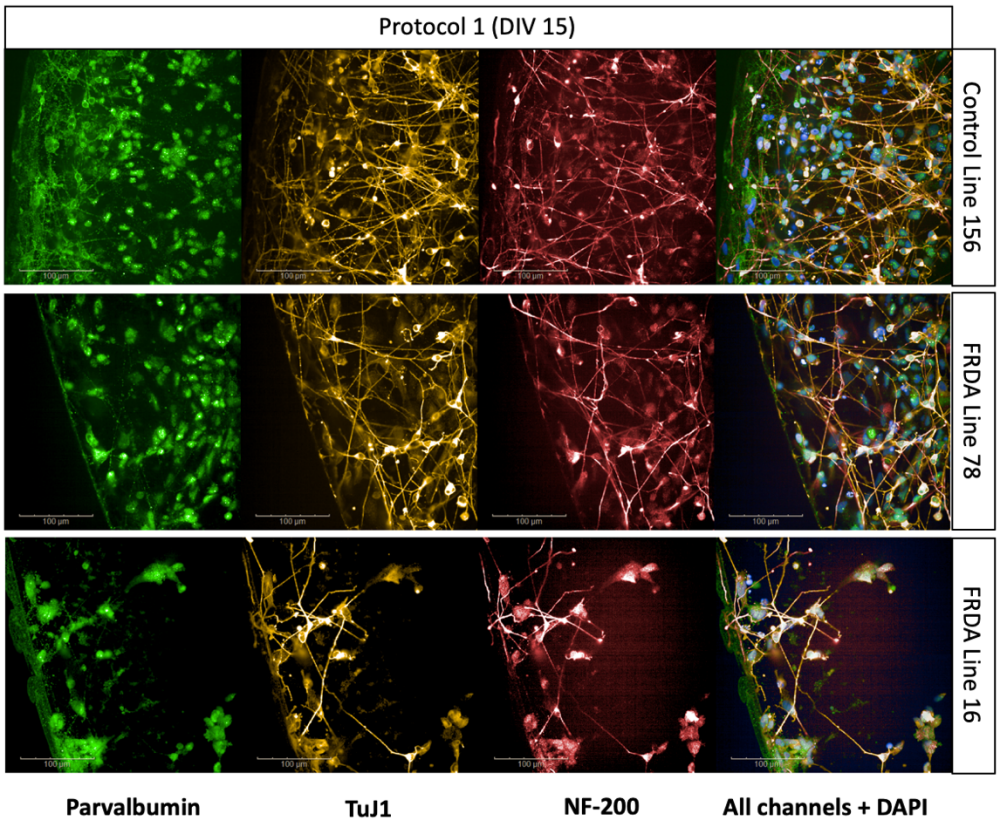
Figure 12: Gene Expression Profiles of Cells Treated with Protocol 2

Time course of gene expression profiles for several markers in control line SFC156-03-01 and FRDA line iPSC4078 (FRDA 78) treated with protocol 2. Several markers show significant changes in levels of their expression during the differentiation time course. (A, FXN; B, BRN3A; C, TRKA; D, TRKB; E, TRKC; F, OCT4). Expression (log2 scale) is shown on the y-axis with the time course of the differentiation on the x-axis. All expression values are relative to day 0 (iPSC stage). mRNA expression was determined by RT-PCR. All expression profiles were derived from the 3rd differentiation.

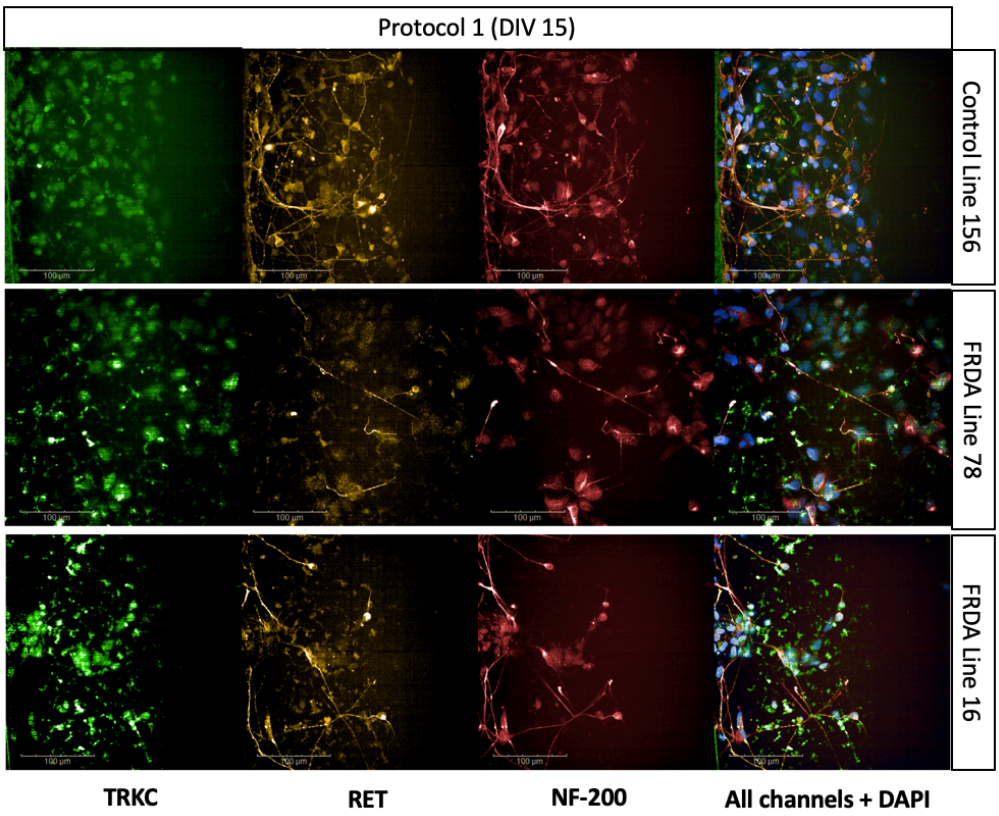
4.2.3. Immunocytochemistry Confirms Expression of Neuronal Markers

The expression of several key neuronal markers was also investigated with immunocytochemistry staining. For the 3rd differentiation, cells were taken on days 15 and 25 for staining and imaging. For protocol 1, all 3 cell lines (SFC156-03-01, iPSC4078 and iPSC3816) were shown to express the neuronal-specific marker TUJ1 at days 15 and 25. Additionally, all lines also exhibited expression of the primary sensory neuronal marker NF-200 and the proprioceptive DRG marker, parvalbumin (PV). All 3 cell lines also demonstrated expression of the nociceptive-marker RET and potential expression of TRKC (see **Figure 13**). For protocol 2, both investigated cell lines (SFC156-03-01 and iPSC4078) were also shown to express the markers TUJ1, NF-200, PV and RET at day 15. The control line additionally showed expression of these markers at day 25 (see **Figure 14**). Our ability to generate sensory neurons expressing key neuronal markers was reproducible, with Figure 15 showing ICC images of neurons derived utilising an alternative control cell line (SFC856-03-04) during a different differentiation (2nd differentiation).

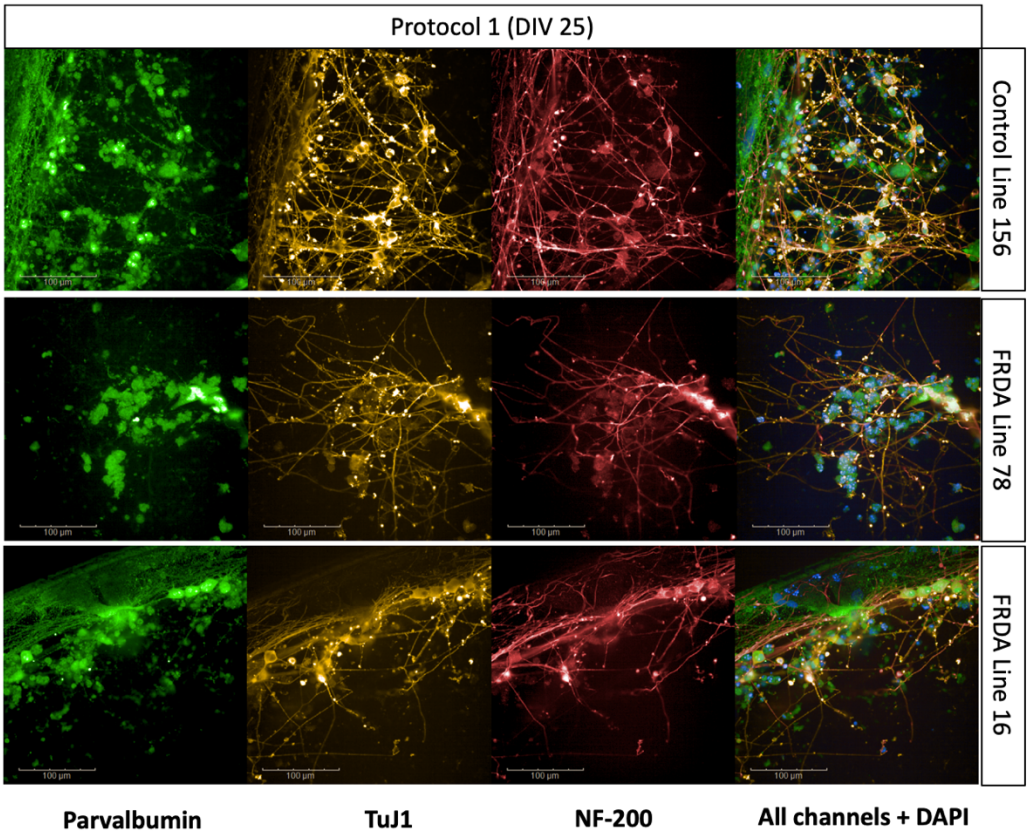
A


Protocol 1 (DIV 15)
Control Line 156
FRDA Line 78
FRDA Line 16
Parvalbumin
TuJ1
NF-200
All channels + DAPI

B


Protocol 1 (DIV 15)
Control Line 156
FRDA Line 78
FRDA Line 16
TRKC
RET
NF-200
All channels + DAPI

C


Protocol 1 (DIV 25)
Control Line 156
FRDA Line 78
FRDA Line 16
Parvalbumin
TuJ1
NF-200
All channels + DAPI

D

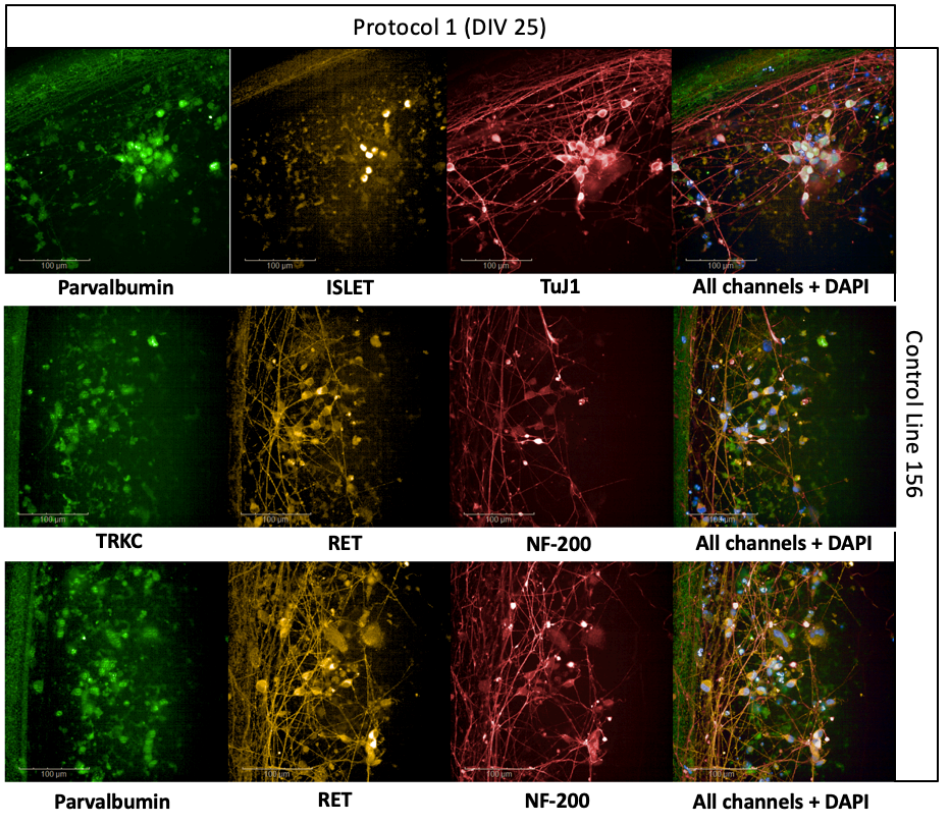
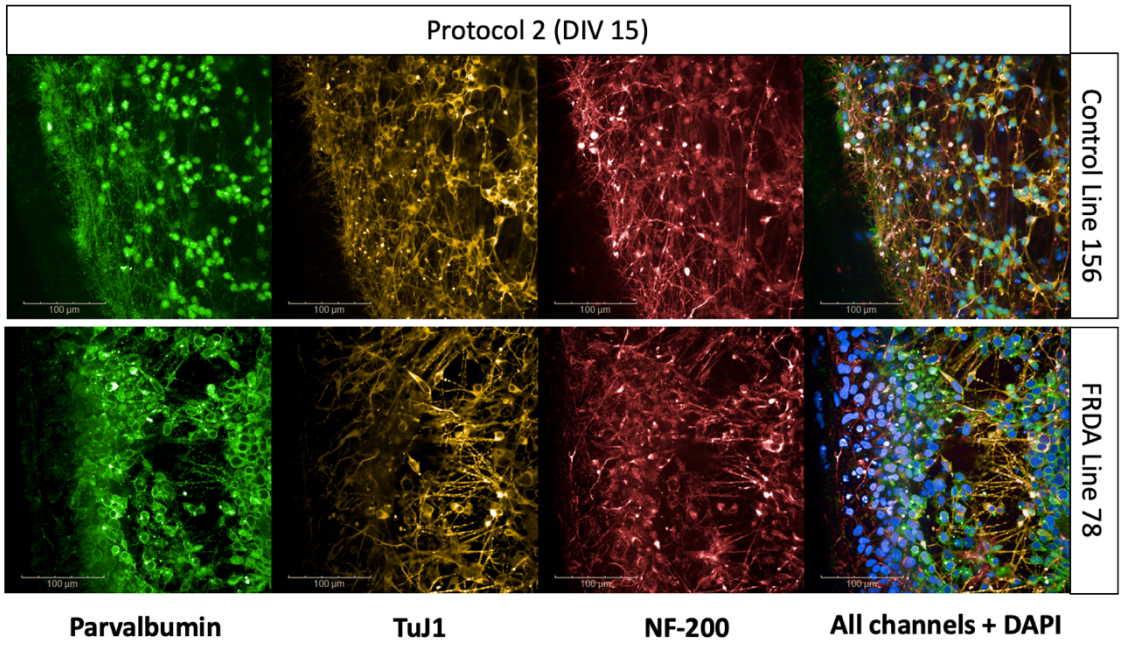

Protocol 1 (DIV 25)
Parvalbumin
ISLET
TuJ1
All channels + DAPI
TRKC
RET
NF-200
All channels + DAPI
Parvalbumin
RET
NF-200
All channels + DAPI
Control Line 156

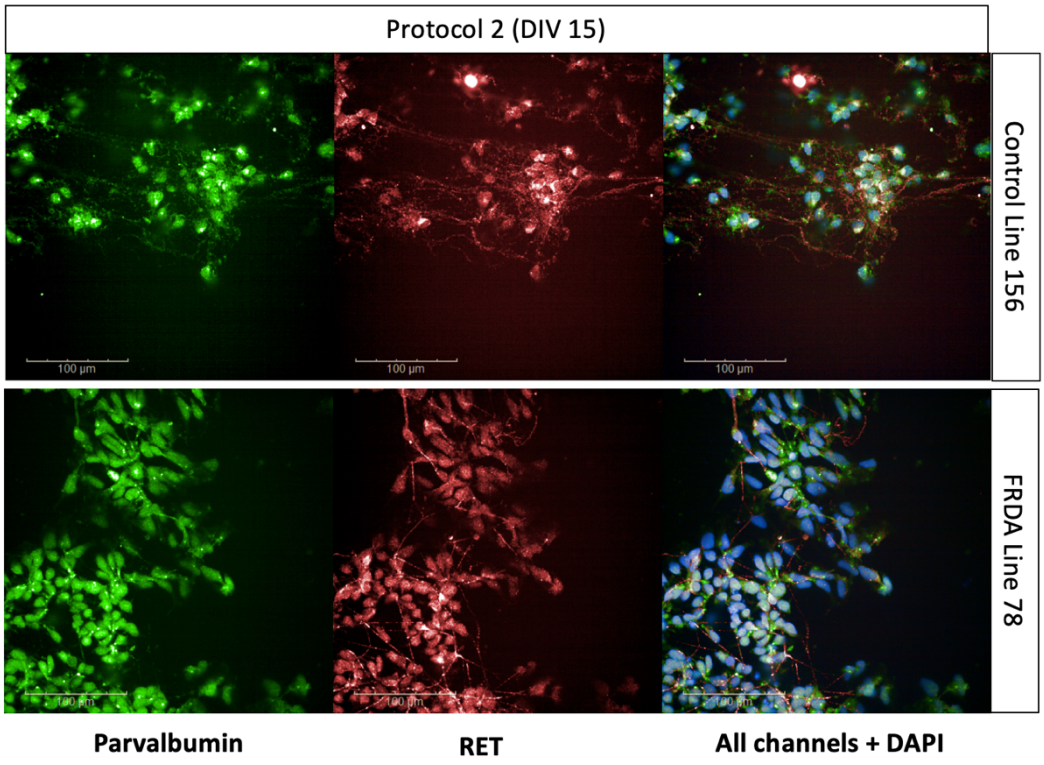
Figure 13: Cells Derived From Protocol 1 Exhibit Expression of Neuronal Markers on ICC

Expression of neuronal markers established by ICC staining and imaging of neurons following treatment with protocol 1. ***A:*** Expression of PV (green), TUJ1 (yellow) and NF-200 (red) at DIV 15 for cell lines SFC156-03-01 (control line 156), iPSC4078 (FRDA line 78) and iPSC3816 (FRDA line 16). Nuclei are shown in blue (DAPI). ***B:*** Expression of TRKC (green), RET (yellow) and NF-200 (red) at DIV 15 for cell lines SFC156-03-01 and iPSC4078. Nuclei are shown in blue (DAPI). ***C:*** Expression of PV (green), TUJ1 (yellow) and NF-200 (red) at DIV 25 for cell lines SFC156-03-01, iPSC4078 and iPSC3816. Nuclei are shown in blue (DAPI). ***D:*** Expression of various additional neuronal markers by the cell line SFC156-03-01 at DIV 25. Nuclei are shown in blue (DAPI). All images were from the 3rd differentiation and were taken using the 40X objective. Scale bar = 100µm. DIV: days *in vitro*.

A



B


Protocol 2 (DIV 15)
Control Line 156
FRDA Line 78
Parvalbumin
RET
All channels + DAPI

C

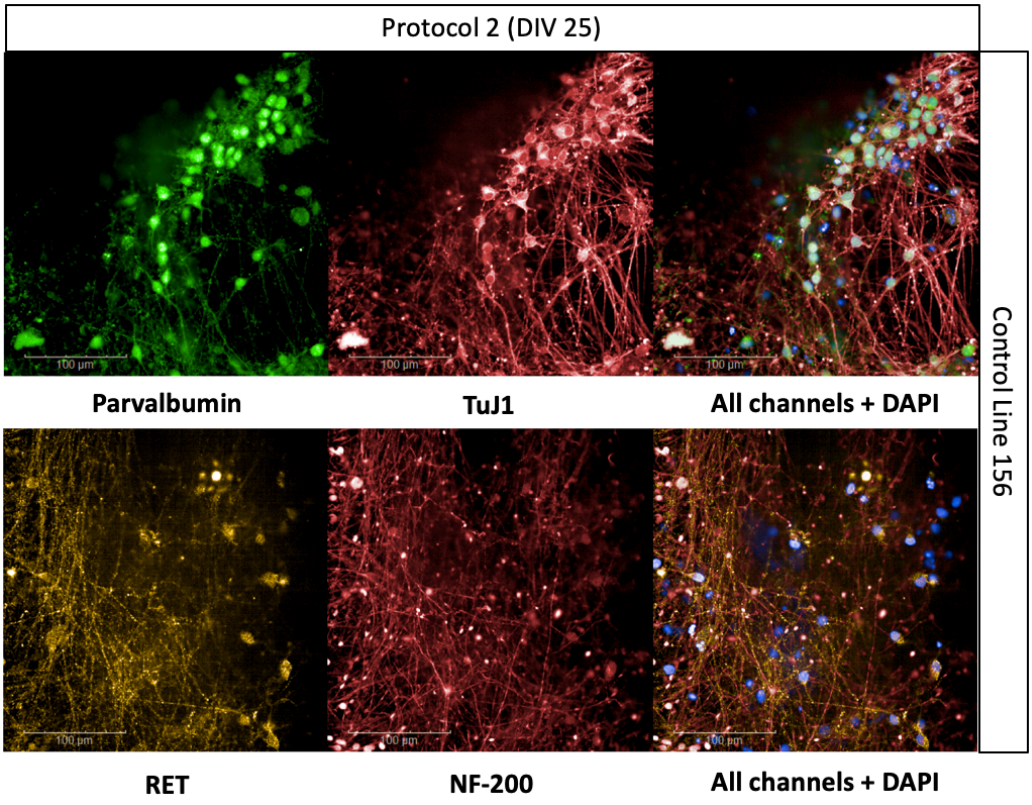

Protocol 2 (DIV 25)
Control Line 156
Parvalbumin
TuJ1
All channels + DAPI
RET
NF-200
All channels + DAPI

Figure 14: Cells Derived From Protocol 2 Exhibit Expression of Neuronal Markers on ICC

Expression of neuronal markers established by ICC staining and imaging of neurons following treatment with protocol 2. ***A:*** Expression of PV (green), TUJ1 (yellow) and NF-200 (red) at DIV 15 for cell lines SFC156-03-01 (control line 156) and iPSC4078 (FRDA line 78). Nuclei are shown in blue (DAPI). ***B:*** Expression of PV (green) and RET (red) at DIV 15 for cell lines SFC156-03-01 and iPSC4078. Nuclei are shown in blue (DAPI). ***C:*** Expression of various additional neuronal markers by the cell line SFC156-03-01 and iPSC4078 at DIV 25. Nuclei are shown in blue (DAPI). All images were from the 3rd differentiation and were taken using the 40X objective. Scale bar = 100µm. DIV: days *in vitro.*

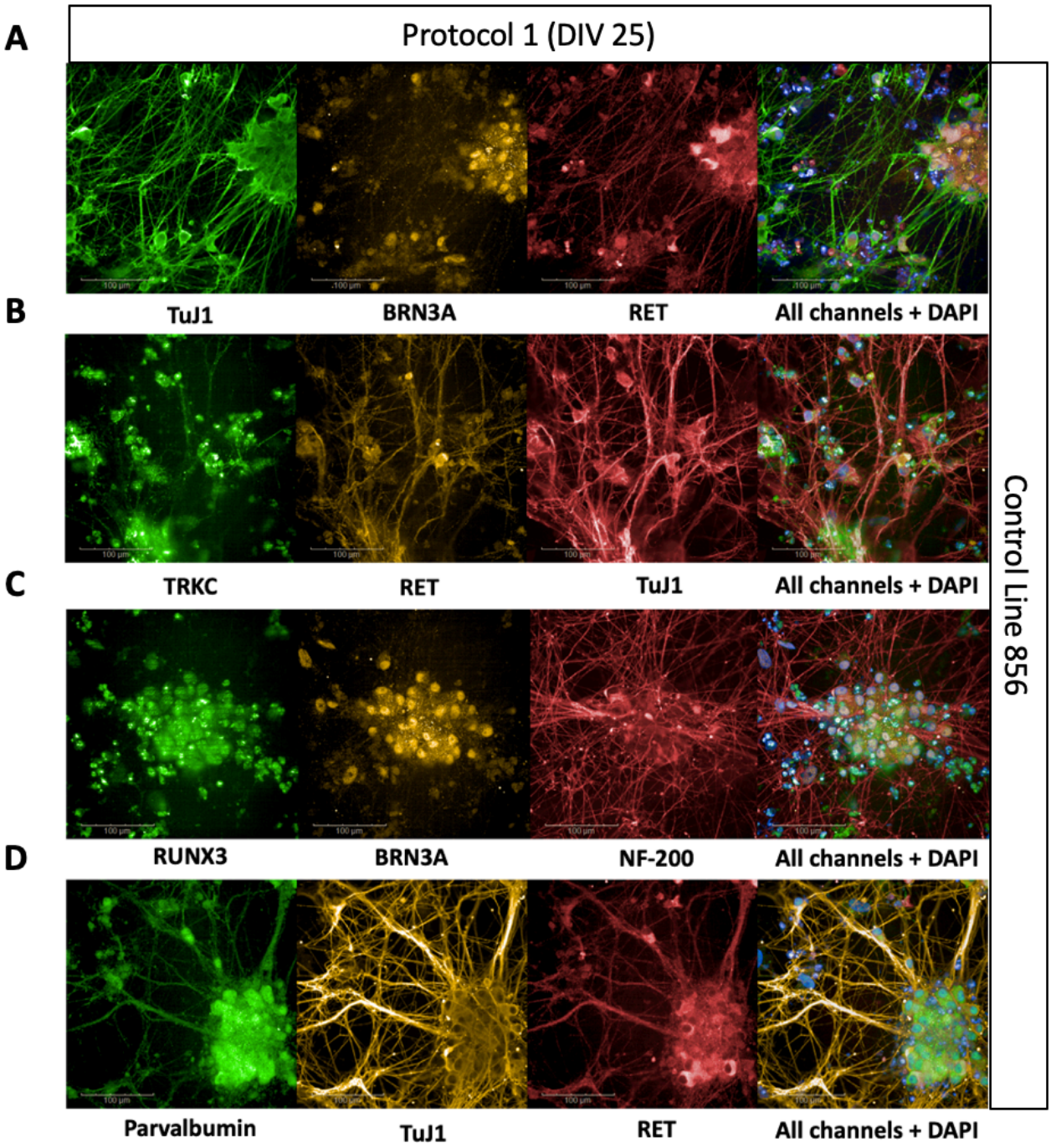

A
Protocol 1 (DIV 25)
B
TuJ1
BRN3A
RET
All channels + DAPI
C
TRKC
RET
TuJ1
All channels + DAPI
D
RUNX3
BRN3A
NF-200
All channels + DAPI
Parvalbumin
TuJ1
RET
All channels + DAPI
Control Line 856

Figure 15: Generation of Neurons Expressing Key Markers is Reproducible

Expression of neuronal markers established by ICC staining and imaging of neurons following treatment with protocol 1. ***A:*** Expression of TUJ1 (green), BRN3A (yellow) and RET (red). Nuclei are shown in blue (DAPI). ***B:*** Expression of TRKC (green), RET (yellow) and TUJ1 (red). Nuclei are shown in blue (DAPI). ***C:*** Expression of RUNX3 (green), BRN3A (yellow) and NF-200 (red). Nuclei are shown in blue (DAPI). ***D:*** Expression of Parvalbumin (green), TUJ1 (yellow) and RET (red). Nuclei are shown in blue (DAPI). All images are from the 2nd differentiation and were taken using the 40X objective, showing the control cell line SFC856-03-04 (control line 856) at DIV25. Scale bar = 100µm. DIV: days *in vitro.*

5. Discussion

Significant progress has been made within the field of therapeutic development for FRDA, yet despite intense research efforts, the disease still currently remains without an effective treatment. This is likely due to an incomplete understanding of disease pathology, coupled with a historic lack of applicable disease models to exploit for drug discovery. This project focuses on approaching both of these major challenges. Firstly, we looked to advance our understanding of the epigenetic mechanisms underpinning *FXN* repression, by exploring the inhibition of the therapeutic target SUV4-20 H1 with novel A-196 structural derivatives. We then worked to optimise and establish an iPSC-derived sensory neuronal model of FRDA. This phenotypically relevant cell model is more capable of accurately recapitulating disease pathology and will eventually be used for the testing of our novel compounds. Thus, overall this project builds on the already extensive progress of drug development for FRDA, looking to contribute to accelerating the discovery of a cure for the disease.

5.1. A-196 Structural Derivatives Increase *FXN* Expression in Cellular Models of FRDA

5.1.1. The Potential of Targeting Histone Methyltransferases SUV4-20 H1

Over the past 20 years, significant progress in our understanding of the role of the epigenome in FRDA pathology has resulted in extensive research efforts investigating epigenetic-based therapies as a potential avenue for the treatment of FRDA. Of significant

interest has been histone deacetylase inhibitors (HDACi), which present the most investigated epigenetic-based therapy for FRDA [74,89]. However, only one other study has investigated HMTases as a therapeutic target for FRDA [159], with the SUV4-20 family of methyltransferase representing an entirely novel target. HMTase inhibitors, and in particular A-196, are particularly exciting due to their highly-selective inhibitory activity, and thus potential ability to evade concerns surrounding global epigenome-wide effects which may result from inhibition seen with other epigenetic-based therapies such as HDACis. This is because a significant number (> 50) non-histone proteins, including several transcription factors and DNA repair proteins, are known to be potential HDAC substrates, thus potentially being altered by HDACi therapy [160]. On the contrary, HMTases possess very few non-histone protein substrates, with neither of the SUV4-20 methyltransferases being reported to methylate non-histone proteins [90,161–163]. A-196 has been shown to selectively inhibit SUV4-20 and no other protein lysine methyltransferases at concentrations up to 10 µM, as well as demonstrating reduced genome-wide perturbations in gene expression when compared to a well-investigated HDACi. Previous data from our lab analysing ~ 14,000 genes, showed treatment with 1-10 uM A-196 resulted in 193-1098 differentially expressed genes (DEGs) compared to previously published data showing 3478 DEGs following treatment with 5 uM HDACi 109 [90,164]. The high-specificity of A-196, presents an exciting reason to warrant its further investigation as an epigenetic based therapy for FRDA, potentially capable of fewer adverse side-effects in comparison to extensively researched HDACis.

5.1.2. Development of A-196 Structural Analogues

Recently published work from our laboratory identified methyltransferase SUV4-20 H1 as a novel and hugely promising epigenetic target for the treatment of FRDA. We have shown that the inhibition of SUV4-20 enzymes with the highly-selective tool compound A-196, results in a corresponding increase in *FXN* mRNA expression in a number of cellular models of FRDA [90]. However, our pilot data looking at the metabolic stability of A-196 indicate a half-life of 10.8 and 48 minutes in the hepatocytes of mice and humans respectively (see **Appendix 1**). If we are to use A-196 as a potential therapeutic, we would want to improve its biostability and pharmacokinetic properties, in order to enable its synthesis as an effective drug capable of instigating long-lasting upregulation of frataxin in patients. For this reason, we looked to develop A-196 structural derivative compounds with enhanced biostability as well as improved SUV4-20 inhibition. By also developing more potent derivatives, we could theoretically lower treatment doses, reducing potential off-target effects and limiting unintended modifications to the epigenome.

These improvements were achieved by working in collaboration with medicinal chemists from the Oxford Target Discovery Institute. Primary data describing the chemical structure of A-196 and the key structural components required for facilitating its inhibitory activity was already available [142]. By utilising data surrounding the structure-activity relationship of A-196 and further investigating the crystal structure of A-196 bound to SUV4-20 H1, chemists were able to identify several potentially exploitable avenues for chemical modification. These included modifications to the molecules cyclopentane ring, addition of chemical groups such as OH and CF_2H to engage the active site water and the introduction

of methylcyclopropyl group. By making these changes, chemists were able to derive A-196 structural analogues with theoretically improved chemical potency and biostability. We were provided with 22 of these newly synthesised derivatives for initial screening. Interestingly, IC_{50} data provided by the chemists and presented as part of **Figure 6C**, showed that 3 of these compounds (compound 7, 13 and 14) had lower IC_{50} values than A-196 for SUV4-20 H1 when investigated with biochemical assays. Several other compounds had IC_{50} values very similar to A-196. These data indicate that our collaborators were successfully able to generate improved structural derivatives, with potentially greater potency than A-196. We are still in the process of performing metabolic stability analysis for our newly synthesised A-196 structural derivatives compounds, but initial data indicates that select derivatives show improved half-life data when compared to A-196. Taken together, these data are hugely exciting and bring the potential use of A-196 as an effective therapy for FRDA one step closer to reality.

5.1.3. Select Structural Analogues of A-196 Increase *FXN* Expression in Initial Screen

We initially screened these 22 compounds using our previously described *FXN*-GAA-Luciferase reporter cell line. We found that 50% of compounds were able to significantly increase *FXN*-Luc expression in comparison to the DMSO treated vehicle control and were classed as positive hits from the initial screen (see **Figures 6A** and **6B**). We utilised A-196 as a positive control, which demonstrated a robust increase in relative *FXN* expression as previously reported in our reporter cell line. When we sorted all 22 structural derivatives in order of their IC_{50} values received from the chemists, we saw a strong correlation

between potency and positive hit compounds. All hit compounds were seen to have lower IC_{50} values than the non-hits, other than compounds 9 and 20. Compound 9 did not return as a hit following initial screening, despite having a lower IC_{50} value (0.079) than several positive hits. On the contrary, compound 20 appeared as a hit after screening, despite possessing a greater IC_{50} value (1.0) than a number of non-hits (see **Figure 6C**). One explanation for this inconsistency may be due to the discrepancy between data generated via biochemical assay and the reporter cell line. The IC_{50} values provided by chemists were calculated using a biochemical scintillation proximity assay utilising recombinant protein. Whilst this data provides a useful preliminary indication of chemical potency, it is unlikely to translate perfectly to biological testing in cell lines. Additionally, whereas compound 9 was shown to be relatively potent biochemically, it may possess unique structural modifications affecting its ability to obtain adequate cell penetrance, or affecting its solubility and stability in solution. The consequences of such characteristics may have not been apparent during biochemical testing, and only presented when utilising the drug for treatment in our reporter cell line. Furthermore, as with all biochemical assays, there is a margin of error expected, which may have also played a contributory role to the small discrepancy seen in our results. Ideally, we would like to repeat our experiments screening both compounds 9 and 20, to further investigate this discrepancy. However, the otherwise strong correlation seen between hit compounds and their stated chemical potency, provided evidence that the data generated from our reporter cell line likely provides a sound indication for the efficacy of the investigated structural analogues.

5.1.4. Validation of Structural Analogues by Initial Concentration-Response Testing

The next step involved progressing identified hit compounds into concentration-response testing. This was performed in order to validate whether the positive data seen from our initial screen was due to a true effect and not the result of some form of experimental artefact. With an increasing treatment concentration of our compounds, we would expect to see a corresponding increase in *FXN* expression, indicating true inhibition of SUV4-20 H1 and not the involvement of an alternative pathway or interaction which results in inconsistent or chance increases in expression. All 11 hit compounds showed increases in *FXN* expression with increasing treatment concentration to largely varying extents (see **Figure 7A-M**). As the majority of curves did not plateau, we were unable to calculate conventional EC_{50} values for each compound. Thus, we were required to devise an alternative method for the comparison of structural analogues with one another. To do this, we interpolated the concentration of each compound required to achieve a relative 1.7-fold increase in *FXN*-Luc expression in comparison to the DMSO vehicle control. The threshold value of 1.7-fold was chosen as it represented an arbitrary value close to the upper-end of expression we had seen following treatment with A-196 in the reporter cell line. In total, 8 out of 11 hits reached 1.7-fold expression, with 3 compounds (compounds 7, 10 and 15) achieving this expression value at concentrations lower than A-196 (6.53 µM) (see **Figure 7N**). One of these compounds (compound 7) also showed a lower IC_{50} value than A-196 in biochemical assays. Of particular note, was that compound 20 (the hit

compound with the greatest IC_{50} value) was one of the compounds which failed to reach 1.7-fold relative expression.

5.1.5. Broader Range Concentration-Response Screen Confirms High-Dose Toxicity

For our initial concentration-response screen, 10 µM was selected as the highest treatment concentration due to previous reports of the emergence of off-target effects at A-196 treatment concentrations greater than 10 µM [142]. Interestingly, prior data published from our lab found that treatment with A-196 at 10 µM and below results in insignificant gene perturbation [90]. Thus, we concluded that 10 µM presented a relatively safe maximum dosage for treatment with our structural analogues. Interestingly, data from our initial concentration-response screen appeared to show that the effects of A-196, alongside the majority of structural derivatives, did not appear to plateau around 10 µM, but rather the curves appeared to show a trend of continually increasing *FXN* expression (see **Figure 7A-M**). As we had not previously tested A-196 or any of the structural derivatives at treatment concentrations greater than 10 µM, we decide to perform a 2nd broader-range concentration-response screen. This was to investigate how the effects of A-196 and its structural derivatives change beyond 10 µM and determine an optimum range of treatment concentrations for our compounds. Using the previously described interpolation data, we selected the 5 most promising hit compounds and A-196 for this screen. We found that for the majority of compounds, maximal *FXN* expression was obtained in the treatment region of 7.6-12 µM, before expression began to rapidly decline with increasing concentrations, implicating high-dosage associated toxicity. For all compounds, a

treatment concentration of 40 µM resulted in a sharp crash in relative *FXN* expression (close to 0-fold), indicating extensive cellular death (see **Figure 8A-G**). This was confirmed by images of wells treated at 40 µM, which contained sparse cells with abnormal morphologies (see **Figure 8H-L**). Altogether these data indicate that 10 µM likely presents a safe ceiling dosage for treatment with our structural analogues. Additional gene perturbation studies investigating the off-target effects of each structural analogue, would provide valuable data to fully establish the optimum range of treatment concentrations for each of our novel compounds.

5.1.6. The GAA-*FXN*-Luciferase Reporter Cell Line as a Model for FRDA

We utilised our previously described *FXN*-GAA-Luciferase reporter cell line for all initial compound screening and concentration-response validation. This strategy provided a relatively cost-efficient and rapid method to assess the initial efficacy of our structural derivatives. Our reporter line is constructed utilising the entire *FXN* genomic DNA locus, including introns, exons and a native promotor region. With the *FXN* loci being placed in its natural genomic context, we are able to effectively model physiologically relevant gene silencing due to the presence of the GAA repeat expansion [148]. This provides a huge advantage over several historically used alternative reporter lines for FRDA drug discovery, which either lack the relevant *FXN* sequence [143,145], or only carry a select region of its 1st intron [144]. However, reporter cell lines do carry several limitations, which are important to consider when interpreting any data which they generate. One such limitation is the use of bioluminescence for the assessment of *in vitro* transcriptional activity. The luciferase gene provides a versatile reporter target, which is relatively simple to assay for the

measurement of gene expression. However, luciferase has been shown to have a half-life of ~ 2 hours in live HEK 293 cells [165] (background cell used for our reporter line) and ~ 3 hours in cell lysate [166]. The half-life of the *FXN*-Luc fusion construct is still to be established. It is possible that the determination of *FXN* expression in our reporter line may be underestimated due to turnover of the fusion construct throughout the treatment protocol. Additionally, structural derivatives with a shorter half-life may also present a reduced signal by the point of assay. We partly tackled this issue by incubating cells with fresh media (made with new compounds) 2 days following their initial treatment. However, it is still important to consider the general limitations of bioluminescence as a technique for assaying gene expression when interpreting our screening data.

Another important consideration is that reporter cell lines have been immortalised to evade normal cellular senescence and enable unlimited cellular proliferation. Their continual division means they have the opportunity to accumulate more mutations, potentially decreasing their physiological relevance. It was therefore important that we eventually progress evaluation of our compounds to FRDA patient cells. As these are primary cells taken directly from FRDA patients (and have not been immortalised) they provide a more accurate representation for disease modelling. Interestingly, previous reports from our lab found that A-196 was capable of increasing *FXN* expression in both our GAA-expanded and non-expanded reporter cell lines. This was an unusual finding, as we would expect upregulated expression to be specific to the pathological expanded line. Further research utilising primary fibroblast cells, showed that A-196 selectively increased *FXN* expression in pathological expanded FRDA cells and not wildtype controls [90]. These

data indicate that our reporter cell line may not perfectly represent the true nature of the endogenous WT locus and that patient-derived primary fibroblast lines likely characterise a more physiologically relevant disease model.

5.1.7. Structural Analogues Potentially Increase *FXN* Expression in FRDA Patient-Derived Fibroblasts

Utilising interpolation data from our initial concentration-response screen, we then selected the 6 most promising hits for testing in two FRDA patient-derived primary fibroblast lines GM4078 and GM3816. We used the wildtype control line GM03440 as a reference for normal *FXN* expression. This GM03440 line exhibited ~ 3-fold the *FXN* mRNA expression of vehicle-treated expanded lines (see **Figure 9A-B**), consistent with previous reports in the literature indicating that FRDA cells produce ~ 30% of normal *FXN* protein levels [10,13,14]. When testing our 6 structural analogues in the GM4078 line, we saw a trend of increased *FXN* mRNA expression in comparison to the vehicle DMSO for all structural analogues. However, this increase in expression was statistically significant for only compound 6 at 5 uM (see **Figure 9A**). Interestingly, compound 6 did not have the lowest IC_{50} value of the derivatives tested, providing a further indication for the divergence of cell behaviour in cellular assays compared with biochemical testing. The GM3816 line was seen to be less responsive to treatment, with no structural analogues returning significant increases in *FXN* mRNA expression (see **Figure 9B**).

5.1.8. The Influence of Repeat Length on Compound Effect Sensitivity

One explanation for the discrepancy in compound effect seen between cell lines is to do with repeat expansion length. The GM4078 line was derived from an FRDA patient with *FXN* alleles carrying an average of 481 repeats, whilst GM03816 was derived from an FRDA patient with *FXN* alleles carrying an average of 355 repeats. It has been well documented that the length of the GAA repeat expansion has a strong inverse correlation with *FXN* expression and the severity of disease phenotype [17–22,32]. The larger repeat expansion of the GM4078 line may explain the more potent effects of our structural derivatives in this line. It is plausible that GM4078 fibroblasts possess a more severe phenotype and thus are more susceptible and receptive to therapies aimed at upregulating *FXN* expression. Additionally, raw data from our experiments (not shown) indicated a slightly greater *FXN* expression in the GM03816 line when compared to the GM4078 line, consistent with its smaller repeat expansion. As all the expression data were normalised to vehicle controls, the effect of the structural derivatives in the GM03816 line may have been subdued owing to its already increased *FXN* expression. These finding raise several interesting questions surrounding whether there is an optimum repeat expansion length for *FXN* upregulation therapy. It may be the case that patients with a greater number of GAA repeats, and thus the lowest existing *FXN* production and most severe phenotypes, may present the most promising candidates to potentially benefit from treatment targeting SUV4-20 H1 inhibition. Patient repeat expansion length presents a difficult to control but important characteristic to consider, when testing novel therapies in FRDA clinical trials. Further

research is required to establish whether the number of GAA repeats significantly influences treatment outcomes of *FXN* upregulation therapy in both cell lines and patients.

5.1.9. Evaluating the Optimal Treatment Concentration

Another interesting observation from testing in fibroblasts was that overall there were no major improvements in treatment efficacy between 5 and 10 µM, with the majority of structural derivatives performing better when used at 5 µM (see Figure **9A-9B**). This finding is consistent with data previously published from our laboratory, showing no significant differences in *FXN* protein expression following treatment of the GM4078 fibroblast line with A-196 at 5 and 10 µM [90]. Interestingly, data from our 2nd concentration-response screen also shows A-196 reaching maximum efficacy at 5 µM (see **Figure 8F**). Further analysis of the data from the 2nd concentration-response screen, indicates that the toxic effects of a number of structural derivatives start to become apparent at treatment doses just above 10 µM, with *FXN* expression beginning to decline (see **Figure 8A-G**). It may be the case that treatment of primary FRDA fibroblasts with our structural analogues at 10 µM, might already be at a dose which is capable of stressing the cells. Additionally, these compounds may have already approached some form of saturation effect at 10 µM in patient fibroblasts.

5.1.10. A-196 as a Variable Positive Control

One key area of discussion following analysis of our fibroblast drug response data was the failure of A-196 to significantly upregulate *FXN* expression in comparison to the vehicle control. We used A-196 as a positive control for our experiment, as we know that it is

capable of increasing *FXN* expression in FRDA patient-derived fibroblasts. However, our data showed treatment with 10 µM resulted in only an insignificant ~ 1.15-fold expression in comparison to the DMSO control for both cell lines (see Figure **9A-B**). Interestingly, whilst prior work investigating A-196 treatment in the GM4078 line has shown significant increases in *FXN* mRNA expression, this effect size was relatively small, with published data demonstrating a ~ 1.25-fold increase in expression following 10 µM treatment. It appears to be the case that the efficacy of A-196 is much more apparent in a number of other cell types, such as our reporter cell line and FRDA PBMCs [90]. Additionally, throughout our experimentation we have observed that the effect of A-196 in fibroblasts can vary between experiments, sometimes producing a strong response, whilst other times failing to upregulate *FXN*. In the case of my project, A-196 appeared to produce a positive response for the first 2 replicates of my fibroblast experiments, whilst having no effect for my 3rd and final replicate. The lack of effect in my 3rd replicate likely contributed to the failure of A-196 to demonstrate statistically significant upregulation of *FXN* expression. This experimental variability in fibroblasts presents a key point of discussion and requires further investigation. One potential source for this variability includes the passage number of the fibroblasts used. Whilst I aimed to use a relatively low passage number for all my fibroblast experiments, the passage number varied between experimental replicates. As the GAA repeat expansion is reported to be unstable across generations [23,24], increasing passage number lengths may have influenced GAA repeat length through expansion or contraction, thus causing experimental variability. As the effect size of A-196 is relatively small, batch variability between A-196 vials may also have contributed to the experimental results seen. Increasing the number of experimental repeats may enable us to account for

some of this overall variability, whilst also allowing a better statistical assessment of the effects of our structural analogues (data for compound 10 at 5 µM and compound 12 at 5 and 10 µM was only n=2). In future experiments it would also be worthwhile to measure frataxin protein expression following treatment via a technique such as western blotting. This would provide another means to investigate whether A-196 and our compounds are capable of upregulating *FXN* in fibroblasts, whilst also allowing us to assess whether we are capable of not only increasing *FXN* mRNA, but also frataxin protein expression.

5.1.11. Target Upregulation Required for Therapeutic Benefit

It is also worth mentioning that all structural analogues investigated outperformed A-196 in fibroblast testing. These results indicate that we have likely been successful in our aim of synthesising select novel A-196 derivatives displaying improved potency. Particularly exciting is compound 6, which demonstrated a statistically significant ~ 2-fold increase in *FXN* mRNA expression in comparison to the vehicle DMSO, and was capable of upregulating *FXN* expression to ~ 64% of the levels seen in our wildtype control (see **Figure 9A**). This notably large effect size begs the question as to what levels of *FXN* upregulation we should be aiming for in order to facilitate effective therapy. Since FRDA patients typically possess such reduced levels of *FXN* protein, it is often thought that even a slight increase in *FXN* expression will likely have a positive effect on patient outcomes. Additionally, asymptomatic carriers of FRDA, have been shown to possess 30-80% of the *FXN* protein levels seen in healthy controls [10–14]. As these individuals do not display a disease phenotype, increasing *FXN* expression to target levels similar to those seen in carriers, is likely to have a significant therapeutic benefit for FRDA patients. In the GM4078 line,

compound 6 was capable of upregulating *FXN* mRNA expression to ~ 64% of wildtype levels (see **Figure 9A**), well within the upper-range of this target therapeutic window for significant benefit. These are very promising results, but further research is required to establish associated toxicity, as well as investigating how treatment with compound 6 influences *FXN* expression in a number of other cell types, before it can confidently be progressed to *in vivo* testing.

5.2. Establishing an iPSC-derived Sensory Neuronal Model of FRDA

5.2.1. Why Develop iPSC-derived Models for FRDA?

The phenotypic relevance of historically used cell models for FRDA drug discovery has presented a major hurdle to developing an effective therapy for the disease. Whilst readily accessible primary patient cells, such as fibroblasts and PBMCs, enable more accurate disease representation than reporter cell lines, they are not severely affected by the consequences of *FXN* deficiency. Neurons and cardiomyocytes represent the most vulnerable cell populations, although are not feasibly accessible from live FRDA patients. It is for these reasons that researchers have struggled to find a phenotypically relevant FRDA *in vitro* model for the testing of novel therapeutic compounds. The recent advent of iPSC technology has revolutionised the field of FRDA drug discovery, enabling researchers to generate a number of traditionally elusive cell types from FRDA iPSCs (see **Figure 3**). These cell types are the most phenotypically relevant to FRDA pathology, thus representing the current gold-standard *in vitro* models for researchers to study the effects of novel

therapeutics. During this project, we were able to optimise and establish our own FRDA iPSC-derived sensory neuronal model in the laboratory. This model will eventually be used to evaluate our most promising A-196 structural derivatives, providing us with valuable data to evaluate the efficacy of our compounds in a physiologically relevant model of FRDA.

5.2.2. Generation of Specific Neuronal Subpopulations of the DRG

FRDA neuropathology has been shown to disproportionately affect the DRG. This structure contains the cell bodies of PSNs, including nociceptors, mechanoreceptors, proprioceptors, thermoreceptors and chemoreceptors. These are large, pseudo-unipolar neurons, responsible for relaying sensory information from the peripheries to the CNS [38,167]. With the natural disease course, the DRG of FRDA patients undergoes extensive neurodegeneration, indicating particular susceptibility of these neuronal subpopulations to *FXN* deficiency. For this reason, when establishing our iPSC-derived neuronal model of FRDA we chose to adapt 2 previously published differentiation protocols, both of which had described the successful generation of sensory neuronal subpopulations commonly found within the DRG. Protocol 1 has been shown to generate mixed populations of PSNs, composed predominately of nociceptors, [157] whilst protocol 2 has described the generation of PSN cultures which are greatly enriched for proprioceptors [158]. The generation of proprioceptors is of particular research interest, due to the fact they comprise only 7.5% of PSNs found in the DRG, yet are responsible for the majority of *FXN* expression within the structure[108,156]. This indicates that they are likely the PSN subpopulation most vulnerable to FRDA pathology.

5.2.3. Inter-Protocol Differences in Neuronal Generation

Utilising both protocols, we were able to successfully generate sensory neurons from control and FRDA iPSCs. Daily inspection of the cells and examination of phase-contrast microscopy images highlighted various differences between the neurons derived from each protocol. Both protocols showed the gradual differentiation of iPSCs to neural precursors, initially generating bipolar-looking neurons, before maturing to a more adult pseudo-unipolar phenotype. This sequence of maturation is in keeping with reports of DRG embryological PSN maturation [167]. Interestingly, protocol 2 was seen to generate cells demonstrating neuronal morphological characteristics earlier in the differentiation, but generally resulted in overall fewer neurons compared with protocol 1 at DIV 25 (see **Figure 10**). This was somewhat expected, due to the fact that neuronal maturation and neurotrophic treatment was commenced earlier with protocol 2, with its replating day being 3 days prior (day 9) to that of protocol 1 (day 12). However, this prompt neurogenesis likely placed cells under greater stress and explains the higher levels of cell death which were observed for protocol 2. This was particularly apparent with the FRDA iPSC3816 line, which was unable to survive treatment with protocol 2, but for which we were capable of generating neurons at DIV 25 when treating with protocol 1. However, the variability of each cellular differentiation means that ideally we would like to repeat differentiations using the iPSC3816 line treated with protocol 2, to see if we can successfully generate sensory neurons. Of further interest, was that whilst protocol 2 would often overall produce fewer neurons by DIV 25, the neurons which were generated appeared to be slightly more representative of a pseudo-unipolar phenotype. This raises interesting

questions surrounding selecting a protocol that is able to balance the generation of neuronal subpopulations of interest exhibiting the most relevant phenotypes, whilst also maximising cell number and viability. Protocol 1 appears to result in greater neuronal generation, whilst protocol 2 appears to generate more phenotypically relevant neurons. This indicates the optimal protocol may present in the form of a hybrid protocol, combining the neuronal maturation of protocol 2, with the timescales of protocol 1. Further investigation is required to fully establish whether protocol 1, protocol 2 or indeed a hybrid protocol, will enable us to generate the most suitable iPSC-derived sensory neuronal model of FRDA.

5.2.4. Protocol Optimisation

Over the course of this project, I performed a total of 3 differentiations, altering a number of conditions with each differentiation in order to optimise protocols for the successful generation of sensory neurons. One important change which was made was the basement membrane matrix used to coat plates for cellular replating. In the initial 2 differentiations, plates were coated with Corning Matrigel matrix. However, despite this coating I still noticed a substantial degree of cell-peeling following replating. For our 3rd and final differentiation we performed a poly-l-ornthine coating in addition to utilising Geltrex matrix to coat plates for replating day. Following this change, we observed a decrease in cell-peeling, with a more uniform layer of neuronal growth. We also changed the number of cells plated on replating day and the size of some of the microplates used for replating. This was done in order to increase cellular density and thus improve cell growth and viability. In our initial 2 differentiations, we noticed that sparse plating of cells on replating

days resulted in greater levels of cellular death. For this reason, by our 3rd differentiation we had increased the number of cells plated to 15,000 cells/well for the 96 well plates and 100,000 cells/well for the 12 well plates. Additionally we changed from using 6 well plates for RNA extraction in the 1st differentiation, to 12 well plates by the 3rd.

5.2.5. Cells Exhibit Sensory Neuronal Gene Expression Profiles During Differentiation

We further investigated the efficiency of sensory neuronal differentiation process by analysing the expression profiles of several key genes, obtained via RT-qPCR. Throughout the differentiation process, we witnessed a rapid decline in the expression of the pluripotent marker *OCT4* for all cell lines in both protocols, indicating successful differentiation of mature cell types (see **Figures 11F and 12F**). The pan-sensory transcription factor *BRN3A* is expressed in developing sensory neurons during embryogenesis, whilst also having been shown to play a role in the specification of mature DRG PSN subtypes. In our cultures, the expression of *BRN3A* was strongly induced early in differentiation, indicating increasing sensory neuronal development. Levels of *BRN3A* were then seen to plateau towards and remain fairly constant following the replating days, confirming the sustained presence of maturing sensory neurons in our cultures (see **Figures 11B and 12B**). Taken together the rapid and sustained decreases in *OCT4* expression and increases in *BRN3A* expression indicate that we were successfully able to generate sensory neurons from our iPSC lines using both differentiation protocols.

5.2.6. Determination of Neuronal Subpopulations Derived

Analysis of the gene expression profile for the Trk receptors, which signposted the final stages of sensory neurogenesis, allows us to further assess the nature of the subpopulations of sensory neurons derived. For all cell lines treated with protocol 1, expression of nociceptive-marker *TRKA* peaked at day 12 (replating day), before its levels decreased. This was matched with a large sustained increase in expression of the mechanoreceptive-marker *TRKB* (for all cell lines) and the proprioceptive-marker *TRKC* (for control 156 and FRDA 16 lines) into the late stages of differentiation (see **Figure 11C-E**). The greater levels of *TRKB* and *TRKC* expression in comparison to *TRKA* during the final stages of differentiation was also observed for protocol 2 (see **Figure 12C-E**). These results potentially indicate that following a period of neuronal maturation, both protocols are capable of generating cultures with reduced numbers of nociceptors and a greater proportion of mechanoreceptors and proprioceptors. However, it is important to mention that we are unable to determine to what extent our cultures are composed of $TrkC^+$ proprioceptors, $TrkB^+$ mechanoreceptors and double-positive $TrkB^+$/ $TrkC^+$ mechanoreceptors. As we have concordant upregulation of *TRKB* and *TRKC*, it could be that we have either generated mixed neuronal populations of mechanoreceptors and proprioceptors, or that the observed *TRKC* expression is due only to the presence of $TrkB^+$/ $TrkC^+$ mechanoreceptors in our final cultures. For future differentiations, assessing the gene expression profile of the neuronal marker *RUNX3* alongside *TRKB* and *TRKC* would provide vital information to help discern neuronal subpopulations. RUNX3 is responsible for the generation of $TrkC^+$ proprioceptors from starting $TrkB^+$/ $TrkC^+$ populations of

neurons, via the maintenance of *TRKC* expression and the repression of *TRKB* [158]. Therefore, TrkC$^+$ proprioceptors show upregulated *RUNX3* expression, whilst TrkB$^+$/ TrkC$^+$ mechanoreceptors do not express *RUNX3*. Determining the gene expression profile of *RUNX3* in our derived neurons, could hence help establish whether we have successfully been able to generate proprioceptors in our cultures. See **Figure 16** for a visual representation of how the expression of key markers drives the sensory neurogenesis process.

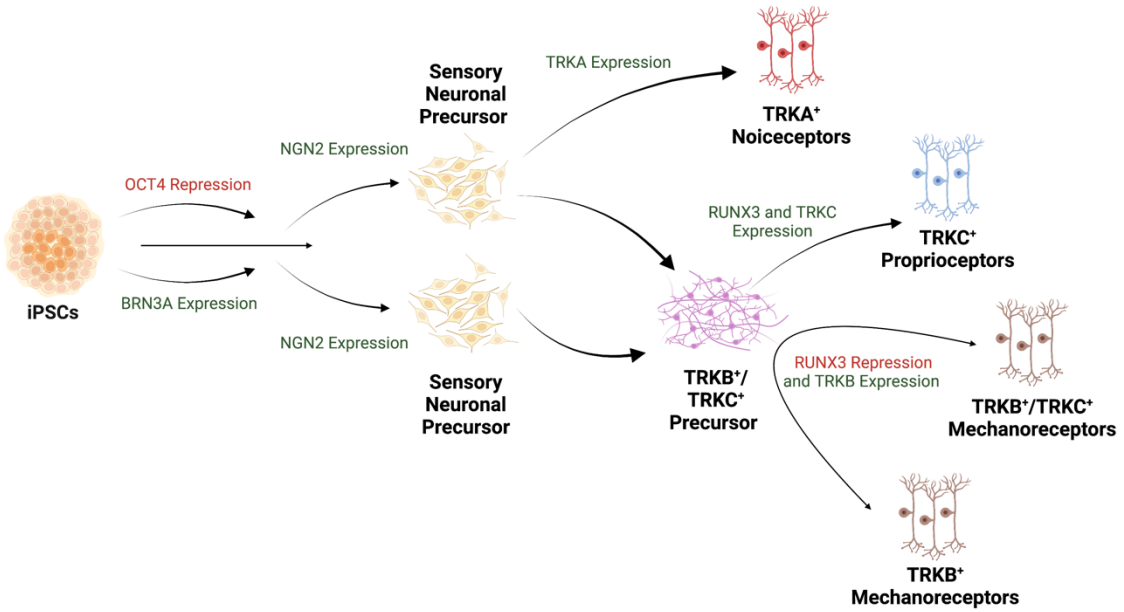


Figure 16: Visual Overview of Sensory Neurogenesis

A visual representation of how the gene expression and repression of key markers drives the process of sensory neurogenesis from iPSCs to differing populations of peripheral sensory neurons. Initial *OCT4* repression, *BRN3A* expression and either neurogenin 1 (NGN1) or neurogenin 2 (NGN2) expression results in 2 types of sensory neuronal precursors. Expression of *NGN1* followed by *TRKA* expression results in nociceptor neurogenesis. Expression of *NGN2* results in TRKB$^+$/C$^+$ neuronal precursors. Levels

of *RUNX3* expression/repression then drives neurogenesis of these double positive neurons to either TRKC$^+$ proprioceptors, TRKB$^+$/C$^+$ double positive mechanoreceptors or TRKB$^+$ mechanoreceptors. Green and red text indicate expression and repression of key markers respectively. Figure adapted from Marmigère and Ernfors [168] and created using BioRender.com.

5.2.7. Analysis of *FXN* Gene Expression Profiles

Alongside the assessment of key neuronal markers, we also looked to quantify *FXN* expression to determine if there were any observed differences in expression between control and FRDA iPSC-derived neurons. For protocol 1, the FRDA iPSC3816 line showed reduced *FXN* levels in comparison to the control at all time points investigated, indicating that these neurons were able to successfully recapitulate an FRDA phenotype (see **Figure 11A**). However, the FRDA iPSC3816 line did not survive treatment with protocol 2 and thus further experimentation is required to establish whether these results are reproducible utilising our 2nd protocol. For protocol 1, the FRDA iPSC4078 line showed reduced *FXN* expression in comparison to the control for all but one timepoint investigated (day 12) (see **Figure 11A**). The FRDA iPSC4078 line also showed a greater *FXN* expression in comparison to the control at 2 timepoints (see **Figure 12A**) for protocol 2. These results were unexpected, as we would anticipate seeing reduced *FXN* expression by the FRDA iPSC4078 line for all time points when compared to the control. However, it is crucial to note that whilst the FRDA iPSC3816 line has been well characterised and previously published [169], the FRDA iPSC4078 line remains uncharacterised. We are still in the process of its characterisation, and it may subsequently be established that the line does not accurately

represent an FRDA genotype, thus providing a potential explanation for its unusual *FXN* gene expression profile. Interestingly, it is also worth mentioning that the timepoints where expression of *FXN* by the FRDA iPSC4078 line was greater than the control, were all early in the differentiation process (protocol 1 day 12 and protocol 2 days 9 and 15). The nature of extensive cell division at this point of the differentiation, coupled with the instability of the trinucleotide expansion, may have also contributed to the *FXN* gene expression profile for the FRDA iPSC4078 line. This ties in with another interesting point of discussion, which is why the majority of our data appears to show *FXN* expression peaking early in the differentiation before gradually declining. This upregulation may also potentially be explained by significant levels of early cell division. It is possible that the increased energy requirements of rapidly dividing cells lead to a temporary upregulation in the expression of the mitochondrial protein frataxin.

5.2.8. Interpretation of ICC Staining

ICC staining was utilised as an additional method to determine the presence of expression of several key neuronal markers. For both protocols, we saw strong expression signals for the neuronal marker TUJ1 and the primary sensory neuronal marker NF-200, confirming the successful generation of PSNs (see **Figure 13** and **Figure 14**). Our ability to generate sensory neurons expressing key neuronal markers was reproducible, as demonstrated by images of the control cell line SFC856-03-04 (see **Figure 15**). For the 3rd differentiation, expression of the nociceptive marker RET and the proprioceptive-specific calcium-binding protein parvalbumin, was also seen in neurons derived from both protocols (see **Figure 13** and **Figure 14**). Interestingly, several images also showed neurons displaying

immunoreactivity to both RET and either parvalbumin or TrkC. This was somewhat unexpected, as we would anticipate neurons expressing these markers to be differentiable from one another. One explanation may be that our secondary antibodies are not capable of specifically staining subpopulations of PSNs. In future differentiations, a method we could employ to check for true staining would involve staining a well containing cells with our secondary antibody in the absence of its corresponding primary antibody. No signal should be detected from this well, with the presence of any signal indicating non-specific binding. Interestingly, inhibitory interneurons found in the dorsal horn, responsible for the regulation of pain perception, have also been separately reported to show immunoreactivity to parvalbumin [170] and RET [171]. Another explanation for co-expression of these markers in our images may be that we have generated populations of these inhibitory interneurons within our cultures. Further experimentation is required to determine the subtype specificity of neurons generated by both protocols. Ideally, we would like to extensively investigate the expression of a number of other key markers by ICC such as the Trk receptors and RUNX3. Additionally, we would also want to utilise ICC staining as another method to confirm *FXN* expression in our neuronal subpopulations.

5.2.9. Limitations of iPSCs: Cell Variability

Whilst iPSCs provide researchers with an exciting tool with enormous potential for FRDA drug discovery, they are not without their limitations. One such drawback is their significant cell line-to-line variability, making comparisons between lines difficult to interpret. This variability may be within the FRDA population (e.g. in repeat expansion length) or FRDA-extrinsic, like the presence of single nucleotide polymorphisms (SNPs)

which can influence a cell lines responsiveness to pharmacological intervention. This variability makes the interpretation of data between cell lines challenging, and is made particularly apparent by the difficulty in matching patient and control iPSC lines. An exciting and novel approach for tackling this issue, involves the ability to generate isogenic cell lines, thanks to significant advances in the field of genetic engineering. FRDA isogenic control cell lines are generated from the same individual from whom the diseased line is derived, but have been genetically altered to differ only in their GAA expansion length at intron 1 *FXN* loci [152]. This overcomes issues surrounding inter-individual variability when traditionally comparing results obtained from patient and healthy control iPSC-derived cells. Additionally, the ability to specifically modify GAA expansion length provides researchers with a potential tool to investigate how variation in the number of GAA repeats, influences treatment response in an otherwise theoretically genetically identical cell line. Isogenic corrected patient iPSC lines have already been utilised for FRDA research [152,164] and as their generation becomes easier, it is likely that isogenic controls will soon present a commonly used tool for FRDA drug discovery. It is worth mentioning that our lab possess an isogenic corrected control line for FRDA iPSC3816, and that this line will likely be of enormous value when we eventually evaluate our structural derivatives in iPSC-derived sensory neurons.

5.2.10. Limitations of iPSCs: Age-Related Maturity

Another importation limitation of FRDA iPSC-derived models relates to their inability to effectively capture age-related maturity. FRDA is a disorder of late-adolescent onset, with the mean age of symptom onset being between 10-15 years of age [32]. Meanwhile, cellular

models derived from FRDA iPSCs are immature, possessing a neonatal resemblance which restricts their ability to accurately recapitulate the disease phenotype. This is due to the nature of the reprogramming process, which effectively resets the "developmental clock" of patient cells back to an embryonic state. Thus, iPSC-derived models may fail to demonstrate overt FRDA phenotypes until they have matured to a later stage in their growth. The natural ageing process allows cells the necessary time to be sufficiently exposed to would-be environmental stressors as well as accumulate the progressive degenerative pathology classically seen with FRDA disease. It is plausible that testing potential therapeutic compounds in FRDA iPSC-derived cellular models may not accurately elucidate the response seen as when the same compounds are tested in aged patient cells. However, several exciting solutions are being developed to tackle this issue, including the direct lineage conversion of patient fibroblasts to create artificially-aged induced neurons (iNs) [172,173], as well the *in vitro* stimulation of rapid ageing via progerin exposure [174]. For this project, a point of further investigation would be to see how extending the length of our differentiation protocols affects the sensory neuronal cultures we derive and the data that they generate. Allowing neurons a longer period of maturation may influence the expression of key markers, as well as potentially affecting the specificity of PSN subpopulations derived.

5.2.11. iPSCs and a New Paradigm for FRDA Drug Discovery

Translating promising *in vitro* data to positive clinical trials presents an enormous challenge for scientists when developing novel therapeutics. This is particularly difficult for FRDA drug discovery, due to the nature of conventionally used models for *in vitro* testing. These

have often included fibroblasts and lymphoblast cell lines, which possess limited phenotypic relevance to FRDA pathology. Thus, preclinical data generated in these cell lines is often uncertain and does not always accurately predict drug efficacy in the clinic. Thanks to iPSC technology, we are now able to generate FRDA neurons and cardiomyocytes. These cell types present a previously inaccessible and phenotypically relevant *in vitro* model for the disease, which can be utilised to provide further insight into novel therapeutics prior to their progression into expensive and time-consuming clinical trials. The potential efficacy, toxicity and teratogenicity of drugs can be better evaluated in these models, improving safety and likely increasing the translational success of bench-to-bedside drug development in FRDA. The utility of these novel models was made particularly apparent from studies of the initially promising FRDA drug, resveratrol. Whilst resveratrol returned very promising preclinical data from testing in fibroblast and lymphoblastic FRDA patient lines, the drug performed underwhelmingly in a subsequent clinical trial [134,146,175]. Following its examination in the clinic, a recent study investigating the effects of resveratrol treatment in FRDA iPSC-derived neurons, found only a modest (~ 1.3-fold) increase in *FXN* mRNA expression 48 following treatment with 25 uM resveratrol, with no significant increases in frataxin protein expression [176]. These data highlight the enormous importance of the role iPSC-derived models could play in accelerating FRDA drug discovery. For this reason, we have proposed a new paradigm for drug discovery and development in FRDA, which utilises iPSC-derived models for additional preclinical validation and screening of potential treatments (see **Figure 17**). This enables only the most promising agents to progress to the clinic, saving time, money and resources, whilst hopefully accelerating the discovery of a potential cure.

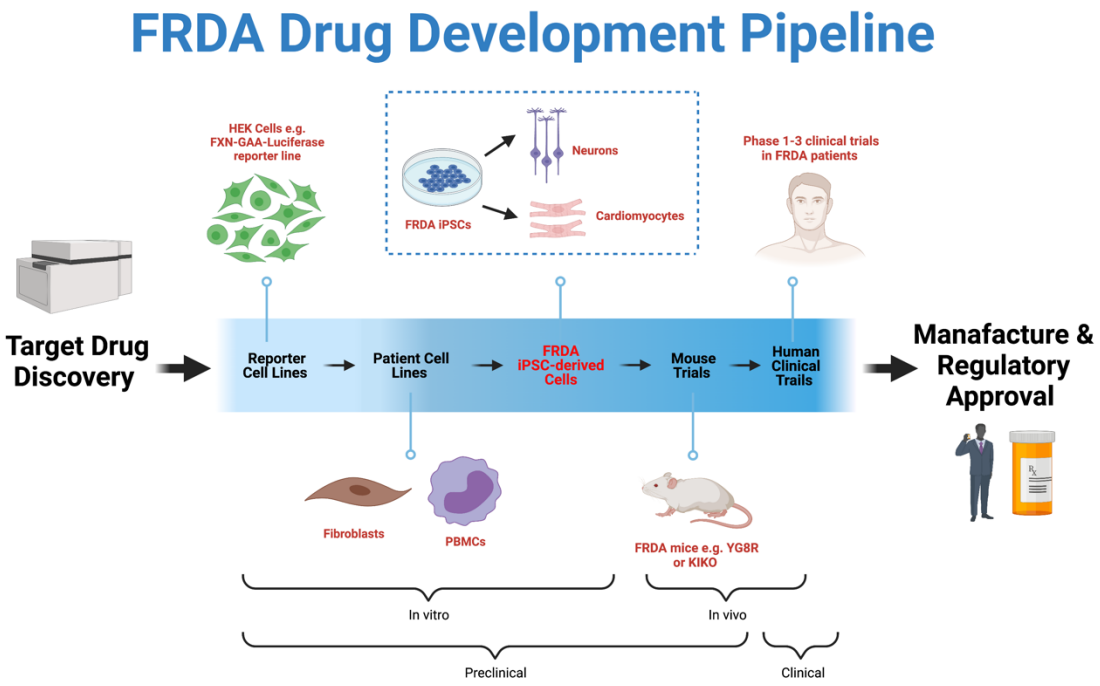


Figure 17: A New Paradigm for FRDA Drug Discovery

Traditionally, novel therapeutic agents progress through a series of *in vitro* testing in reporter and patient primary cell lines, prior to *in vivo* mouse and human trials. This new paradigm consists of an additional step involving the evaluation of compounds in iPSC-derived models (e.g. FRDA neurons and cardiomyocytes) prior to progression to *in vivo* studies. This extra step allows the validation of drugs in a phenotypically relevant model of FRDA, providing researchers with valuable data which can be used to accelerate FRDA drug discovery, whilst minimising resource wastage. Figure taken from (Maheshwari, Vilema-Enríquez and Wade-Martins, in preparation) and was created using BioRender.com.

6. Conclusion and Future Perspectives

6.1. Conclusions

6.1.1. A-196 Structural Derivatives Increase *FXN* Expression in Cellular Models of FRDA

We received 22 structural derivatives of A-196 from chemist collaborators, all of which had been chemically modified to improve potency and biostability. We found that 11 (50%) of these compounds increased *FXN* expression following an initial screen utilising our GAA-Luciferase reporter cell line. The effect of several of these compounds was then subsequently validated through 2 rounds of concentration-response testing, before the 6 most promising compounds were progressed to testing in 2 lines of primary FRDA fibroblasts. Several structural analogues showed a trend of increasing *FXN* expression in the GM4078 line, with one compound (compound 6) significantly increasing *FXN* mRNA expression.

6.1.2. Establishing an iPSC-derived Sensory Neuronal Model of FRDA

We utilised 2 previously published differentiation protocols to derived sensory neurons from 2 control (SFC856-03-04, SFC156-03-01) and 2 FRDA iPSC lines (iPSC4078 and iPSC3816). We examined derived cells via transmitted light microscopy, alongside evaluating the gene expression profiles and ICC staining of several key neuronal markers. The generation of sensory neurons from iPSCs in our cultures was confirmed by increased

expression of BRN3A, in addition to ICC staining of TUJ1 and RET. Evaluation of the gene expression profiles of the Trk receptors, alongside ICC staining of parvalbumin may indicate that we were successful in generating proprioceptors in our cultures. However, further investigation is required to fully establish the specific neuronal subpopulations of derived cells, with data indicating our cultures likely contain a mix of nociceptors, mechanoreceptors and potentially proprioceptors.

Neurons derived from the iPSC3816 line using protocol 1 showed reduced *FXN* expression in comparison to the control iPSC-derived neurons at all timepoints investigated, indicating that these neurons are capable of representing an FRDA phenotype. These data suggest that we were successfully able to establish an iPSC-derived sensory neuronal model of FRDA utilising protocol 1. Neurons derived from the iPSC4078 line demonstrated an unusual *FXN* gene expression profile, with increased *FXN* expression in comparison to the controls observed at several early timepoints for both protocols. Further work is required to fully characterise this line, as well as repeating differentiations for both FRDA lines with both protocols.

6.2. Future Perspectives

6.2.1. Altering Treatment Length

The treatment protocols derived for our structural analogue compounds is based on the SGC probe guidance for treatment with the tool compound A-196. It would be interesting to assess whether altering the incubation period of our compounds may have a residual effect on their efficacy in our cellular models. Further investigation testing the structural

analogues in our reporter cell lines with both shorter and longer incubation periods would provide us with useful data to give us a better indication of how these compounds work. Of particular interest would be to assess whether we can upregulate *FXN* expression with a similar magnitude following a shorter treatment period, as well as attempting to determine the optimum incubation period to maximise an increase in *FXN* expression.

6.2.2. Evaluation of Phenotypes

Investigating whether our FRDA iPSC-derived neurons show reduced *FXN* expression in comparison to control neurons provides us with just one method to evaluate whether they are capable of demonstrating an FRDA phenotype. Beyond just *FXN* gene expression, several other phenotypic characteristics can be assessed to give an indication of how well these models truly recapitulate FRDA pathology. Numerous studies have already characterised several observable phenotypes in FRDA iPSC-derived neurons and cardiomyocytes, including reduced mitochondrial membrane potential, delayed development of electrophysiological functionality, increased beat-rate variability and aberrant calcium handling [155,177–179]. By investigating whether our generated neurons display representative FRDA phenotypes, we can further determine whether a reduced *FXN* expression results in pathological changes for our models. These phenotypes will also provide us with an immensely valuable tool which we can utilise when it comes to assessing the effects of treatment with our structural analogues in our iPSC-derived model of FRDA. In future work, we would want to evaluate whether the treatment of our FRDA sensory neurons with the most promising structural derivatives (such as compound 6) can upregulate *FXN* gene expression. Having several well-characterised phenotypes for our

models would also allow us to evaluate whether treatment with these compounds can result in a phenotypic rescue. If treatment with our structural analogues is able to reverse pathological phenotypes in our FRDA sensory neurons, we will have strong and exciting evidence to warrant the progression of their investigation to *in vivo* studies.

6.2.3. Alternative Therapeutic Approaches

Our laboratory and many others worldwide have focused efforts on developing an epigenetic therapy for FRDA. Alternative therapeutic approaches involve the exploration of gene therapy alongside other non-epigenetic based pharmacological methods for the treatment of FRDA. These future approaches have yielded some exciting advances and may present an alternate means for the development of a cure for FRDA.

Beyond epigenetic based therapy, several other promising classes of drugs are being investigated in the hope to develop an effective pharmacological therapy for FRDA. These compounds belong to various drug classes and are in differing stages of development, with several in late-stage clinical testing. These include antioxidant drugs (idebenone and resveratrol) [175,180], iron chelators (deferiprone) [120] and Nrf2 activators (omaveloxolone) [181], amongst others. Several other non-epigenetic pharmacological approaches have also returned encouraging preclinical data warranting further development and investigation in human trials.

Gene therapy involves modulating the expression of crucial genes to restore function, aiming to directly cure patients, in contrast to chronic pharmacological approaches. Characterised as a single-gene disorder, FRDA presents a candidate disease for which gene

therapy may provide significant potential. Several preclinical gene therapy studies for FRDA have returned promising results, with a multiplicity of approaches aiming to upregulate *FXN* gene expression. These include the use of zinc finger nuclease-mediated excision of the pathological repeat expansion [182,183], delivery of antisense oligonucleotide activators [184], CRISPR Cas9 gRNA mediated knockdown [185] and treatment with FXN expressing plasmids [186].

Bibliography

1. Schulz, J. B. *et al.* Diagnosis and treatment of Friedreich ataxia: a European perspective. *Nat. Rev. Neurol.* **5,** 222–234 (2009).

2. Reetz, K. *et al.* Biological and clinical characteristics of the European Friedreich's Ataxia Consortium for Translational Studies (EFACTS) cohort: a cross-sectional analysis of baseline data. *Lancet Neurol.* **14,** 174–182 (2015).

3. Campuzano, V. *et al.* Friedreich's ataxia: autosomal recessive disease caused by an intronic GAA triplet repeat expansion. *Science* **271,** 1423–1427 (1996).

4. Friedreich, N. Ueber degenerative Atrophie der spinalen Hinterstränge. *Archiv f. pathol. Anat.* **26,** 391–419 (1863).

5. Koeppen, A. H. Friedreich's ataxia: pathology, pathogenesis, and molecular genetics. *J. Neurol. Sci.* **303,** 1–12 (2011).

6. Delatycki, M. B., Williamson, R. & Forrest, S. M. Friedreich ataxia: an overview. *J. Med. Genet.* **37,** 1–8 (2000).

7. Friedreich, N. Ueber Ataxie mit besonderer Berücksichtigung der hereditären Formen. *Archiv f. pathol. Anat.* **70,** 140–152 (1877).

8. Andermann, E. *et al.* Genetic and family studies in Friedreich's ataxia. *Can J Neurol Sci* **3,** 287–301 (1976).

9. Harding, A. E. Friedreich's ataxia: a clinical and genetic study of 90 families with an analysis of early diagnostic criteria and intrafamilial clustering of clinical features.

Brain **104,** 589–620 (1981).

10. Deutsch, E. C. *et al.* A rapid, noninvasive immunoassay for frataxin: utility in assessment of Friedreich ataxia. *Mol. Genet. Metab.* **101,** 238–245 (2010).

11. Saccà, F. *et al.* Clinical use of frataxin measurement in a patient with a novel deletion in the FXN gene. *J. Neurol.* **260,** 1116–1121 (2013).

12. Nachbauer, W. *et al.* Correlation of frataxin content in blood and skeletal muscle endorses frataxin as a biomarker in Friedreich ataxia. *Mov. Disord.* **26,** 1935–1938 (2011).

13. Saccà, F. *et al.* A combined nucleic acid and protein analysis in Friedreich ataxia: implications for diagnosis, pathogenesis and clinical trial design. *PLoS One* **6,** e17627 (2011).

14. Lazaropoulos, M. *et al.* Frataxin levels in peripheral tissue in Friedreich ataxia. *Ann Clin Transl Neurol* **2,** 831–842 (2015).

15. Al-Mahdawi, S. *et al.* Large interruptions of GAA repeat expansion mutations in friedreich ataxia are very rare. *Front. Cell Neurosci.* **12,** 443 (2018).

16. Long, A. *et al.* Somatic instability of the expanded GAA repeats in Friedreich's ataxia. *PLoS One* **12,** e0189990 (2017).

17. Campuzano, V. *et al.* Frataxin is reduced in Friedreich ataxia patients and is associated with mitochondrial membranes. *Hum. Mol. Genet.* **6,** 1771–1780 (1997).

18. Filla, A. *et al.* The relationship between trinucleotide (GAA) repeat length and clinical features in Friedreich ataxia. *Am. J. Hum. Genet.* **59,** 554–560 (1996).

19. Dürr, A. *et al.* Clinical and genetic abnormalities in patients with Friedreich's ataxia. *N. Engl. J. Med.* **335,** 1169–1175 (1996).

20. Montermini, L. *et al.* Phenotypic variability in Friedreich ataxia: role of the associated GAA triplet repeat expansion. *Ann. Neurol.* **41,** 675–682 (1997).

21. Lamont, P. J., Davis, M. B. & Wood, N. W. Identification and sizing of the GAA trinucleotide repeat expansion of Friedreich's ataxia in 56 patients. Clinical and genetic correlates. *Brain* **120 (Pt 4),** 673–680 (1997).

22. Monrós, E. *et al.* Phenotype correlation and intergenerational dynamics of the Friedreich ataxia GAA trinucleotide repeat. *Am. J. Hum. Genet.* **61,** 101–110 (1997).

23. De Michele, G. *et al.* Parental gender, age at birth and expansion length influence GAA repeat intergenerational instability in the X25 gene: pedigree studies and analysis of sperm from patients with Friedreich's ataxia. *Hum. Mol. Genet.* **7,** 1901–1906 (1998).

24. Delatycki, M. B. *et al.* Sperm DNA analysis in a Friedreich ataxia premutation carrier suggests both meiotic and mitotic expansion in the FRDA gene. *J. Med. Genet.* **35,** 713–716 (1998).

25. Epplen, C. *et al.* Differential stability of the (GAA)n tract in the Friedreich ataxia (STM7) gene. *Hum. Genet.* **99,** 834–836 (1997).

26. Pandolfo, M. Friedreich ataxia. *Arch. Neurol.* **65,** 1296–1303 (2008).

27. Brigatti, K. W., Deutsch, E. C., Lynch, D. R. & Farmer, J. M. Novel diagnostic paradigms for Friedreich ataxia. *J. Child Neurol.* **27,** 1146–1151 (2012).

28. Cossée, M. *et al.* Friedreich's ataxia: point mutations and clinical presentation of compound heterozygotes. *Ann. Neurol.* **45,** 200–206 (1999).

29. McCabe, D. J. H. *et al.* Intrafamilial phenotypic variability in Friedreich ataxia associated with a G130V mutation in the FRDA gene. *Arch. Neurol.* **59,** 296–300 (2002).

30. Kostrzewa, M., Klockgether, T., Damian, M. S. & Müller, U. Locus heterogeneity in Friedreich ataxia. *Neurogenetics* **1,** 43–47 (1997).

31. Christodoulou, K. *et al.* Mapping of the second Friedreich's ataxia (FRDA2) locus to chromosome 9p23-p11: evidence for further locus heterogeneity. *Neurogenetics* **3,** 127–132 (2001).

32. Delatycki, M. B. *et al.* Clinical and genetic study of Friedreich ataxia in an Australian population. *Am. J. Med. Genet.* **87,** 168–174 (1999).

33. Alvarez, V., Arnold, P. & Kuntzer, T. Very late-onset Friedreich ataxia: later than life expectancy? *J. Neurol.* **260,** 1408–1409 (2013).

34. Indelicato, E. *et al.* Onset features and time to diagnosis in Friedreich's Ataxia. *Orphanet J Rare Dis* **15,** 198 (2020).

35. Tsou, A. Y. *et al.* Mortality in Friedreich ataxia. *J. Neurol. Sci.* **307,** 46–49 (2011).

36. Leone, M. *et al.* Friedreich's disease: survival analysis in an Italian population. *Neurology* **38,** 1433–1438 (1988).

37. De Michele, G. *et al.* Age of onset, sex, and cardiomyopathy as predictors of disability and survival in Friedreich's disease: a retrospective study on 119 patients.

Neurology **47,** 1260–1264 (1996).

38. Koeppen, A. H. & Mazurkiewicz, J. E. Friedreich ataxia: neuropathology revised. *J. Neuropathol. Exp. Neurol.* **72,** 78–90 (2013).

39. Schöls, L. *et al.* Friedreich's ataxia. Revision of the phenotype according to molecular genetics. *Brain* **120 (Pt 12),** 2131–2140 (1997).

40. McCabe, D. J. *et al.* Typical Friedreich's ataxia without GAA expansions and GAA expansion without typical Friedreich's ataxia. *J. Neurol.* **247,** 346–355 (2000).

41. Weidemann, F. *et al.* The heart in Friedreich ataxia: definition of cardiomyopathy, disease severity, and correlation with neurological symptoms. *Circulation* **125,** 1626–1634 (2012).

42. Pousset, F. *et al.* A 22-Year Follow-up Study of Long-term Cardiac Outcome and Predictors of Survival in Friedreich Ataxia. *JAMA Neurol.* **72,** 1334–1341 (2015).

43. Delatycki, M. B. *et al.* G130V, a common FRDA point mutation, appears to have arisen from a common founder. *Hum. Genet.* **105,** 343–346 (1999).

44. Regner, S. R. *et al.* Analysis of echocardiograms in a large heterogeneous cohort of patients with friedreich ataxia. *Am. J. Cardiol.* **109,** 401–405 (2012).

45. Schadt, K. A. *et al.* Cross-sectional analysis of electrocardiograms in a large heterogeneous cohort of Friedreich ataxia subjects. *J. Child Neurol.* **27,** 1187–1192 (2012).

46. Thoren, C. Diabetes mellitus in Friedreich's ataxia. *Acta Paediatr Suppl* **135,** 239–247 (1962).

47. Hewer, R. L. & Robinson, N. Diabetes mellitus in Friedreich's ataxia. *J. Neurol. Neurosurg. Psychiatry* **31,** 226–231 (1968).

48. Labelle, H., Tohmé, S., Duhaime, M. & Allard, P. Natural history of scoliosis in Friedreich's ataxia. *J. Bone Joint Surg. Am.* **68,** 564–572 (1986).

49. Noval, S., Contreras, I., Sanz-Gallego, I., Manrique, R. K. & Arpa, J. Ophthalmic features of Friedreich ataxia. *Eye (Lond.)* **26,** 315–320 (2012).

50. Corben, L. A., Ho, M., Copland, J., Tai, G. & Delatycki, M. B. Increased prevalence of sleep-disordered breathing in Friedreich ataxia. *Neurology* **81,** 46–51 (2013).

51. Musegante, A. F. A., Almeida, P. N. S., Monteiro, R. T. M. & Barroso, U. Urinary symptoms and urodynamics findings in patients with Friedreich's ataxia. *Int Braz J Urol* **39,** 867–874 (2013).

52. Martinez, A. R. M. *et al.* Nonneurological Involvement in Late-Onset Friedreich Ataxia (LOFA): Exploring the Phenotypes. *Cerebellum* **16,** 253–256 (2017).

53. Bhidayasiri, R., Perlman, S. L., Pulst, S.-M. & Geschwind, D. H. Late-onset Friedreich ataxia: phenotypic analysis, magnetic resonance imaging findings, and review of the literature. *Arch. Neurol.* **62,** 1865–1869 (2005).

54. Ackroyd, R. S., Finnegan, J. A. & Green, S. H. Friedreich's ataxia. A clinical review with neurophysiological and echocardiographic findings. *Arch. Dis. Child.* **59,** 217–221 (1984).

55. Coppola, G. *et al.* Why do some Friedreich's ataxia patients retain tendon reflexes? A clinical, neurophysiological and molecular study. *J. Neurol.* **246,** 353–357 (1999).

56. Corben, L. A. *et al.* Consensus clinical management guidelines for Friedreich ataxia. *Orphanet J Rare Dis* **9,** 184 (2014).

57. Bidichandani, S. I. & Delatycki, M. B. in *GeneReviews(®)* (eds. Pagon, R. A. et al.) (University of Washington, Seattle, 1993).

58. Cossée, M. *et al.* Inactivation of the Friedreich ataxia mouse gene leads to early embryonic lethality without iron accumulation. *Hum. Mol. Genet.* **9,** 1219–1226 (2000).

59. Condò, I. *et al.* In vivo maturation of human frataxin. *Hum. Mol. Genet.* **16,** 1534–1540 (2007).

60. Schmucker, S., Argentini, M., Carelle-Calmels, N., Martelli, A. & Puccio, H. The in vivo mitochondrial two-step maturation of human frataxin. *Hum. Mol. Genet.* **17,** 3521–3531 (2008).

61. Gakh, O. *et al.* Normal and Friedreich ataxia cells express different isoforms of frataxin with complementary roles in iron-sulfur cluster assembly. *J. Biol. Chem.* **285,** 38486–38501 (2010).

62. Koutnikova, H., Campuzano, V. & Koenig, M. Maturation of wild-type and mutated frataxin by the mitochondrial processing peptidase. *Hum. Mol. Genet.* **7,** 1485–1489 (1998).

63. Koutnikova, H. *et al.* Studies of human, mouse and yeast homologues indicate a mitochondrial function for frataxin. *Nat. Genet.* **16,** 345–351 (1997).

64. Babcock, M. *et al.* Regulation of mitochondrial iron accumulation by Yfh1p, a putative homolog of frataxin. *Science* **276,** 1709–1712 (1997).

65. Bencze, K. Z. *et al.* The structure and function of frataxin. *Crit Rev Biochem Mol Biol* **41,** 269–291 (2006).

66. Branda, S. S., Yang, Z. Y., Chew, A. & Isaya, G. Mitochondrial intermediate peptidase and the yeast frataxin homolog together maintain mitochondrial iron homeostasis in Saccharomyces cerevisiae. *Hum. Mol. Genet.* **8,** 1099–1110 (1999).

67. Radisky, D. C., Babcock, M. C. & Kaplan, J. The yeast frataxin homologue mediates mitochondrial iron efflux. Evidence for a mitochondrial iron cycle. *J. Biol. Chem.* **274,** 4497–4499 (1999).

68. Isaya, G. Mitochondrial iron-sulfur cluster dysfunction in neurodegenerative disease. *Front. Pharmacol.* **5,** 29 (2014).

69. Vaubel, R. A. & Isaya, G. Iron-sulfur cluster synthesis, iron homeostasis and oxidative stress in Friedreich ataxia. *Mol. Cell. Neurosci.* **55,** 50–61 (2013).

70. Wilson, R. B. Iron dysregulation in Friedreich ataxia. *Semin Pediatr Neurol* **13,** 166–175 (2006).

71. Puccio, H. *et al.* Mouse models for Friedreich ataxia exhibit cardiomyopathy, sensory nerve defect and Fe-S enzyme deficiency followed by intramitochondrial iron deposits. *Nat. Genet.* **27,** 181–186 (2001).

72. Stehling, O., Elsässer, H.-P., Brückel, B., Mühlenhoff, U. & Lill, R. Iron-sulfur protein maturation in human cells: evidence for a function of frataxin. *Hum. Mol. Genet.* **13,** 3007–3015 (2004).

73. Tan, G., Napoli, E., Taroni, F. & Cortopassi, G. Decreased expression of genes involved in sulfur amino acid metabolism in frataxin-deficient cells. *Hum. Mol.*

Genet. **12,** 1699–1711 (2003).

74. Sandi, C., Sandi, M., Anjomani Virmouni, S., Al-Mahdawi, S. & Pook, M. A. Epigenetic-based therapies for Friedreich ataxia. *Front. Genet.* **5,** 165 (2014).

75. Wells, R. D. DNA triplexes and Friedreich ataxia. *FASEB J.* **22,** 1625–1634 (2008).

76. Sakamoto, N., Ohshima, K., Montermini, L., Pandolfo, M. & Wells, R. D. Sticky DNA, a self-associated complex formed at long GAA*TTC repeats in intron 1 of the frataxin gene, inhibits transcription. *J. Biol. Chem.* **276,** 27171–27177 (2001).

77. Grabczyk, E. & Usdin, K. The GAA*TTC triplet repeat expanded in Friedreich's ataxia impedes transcription elongation by T7 RNA polymerase in a length and supercoil dependent manner. *Nucleic Acids Res.* **28,** 2815–2822 (2000).

78. Sakamoto, N. *et al.* Sticky DNA: self-association properties of long GAA.TTC repeats in R.R.Y triplex structures from Friedreich's ataxia. *Mol. Cell* **3,** 465–475 (1999).

79. Ohshima, K., Montermini, L., Wells, R. D. & Pandolfo, M. Inhibitory effects of expanded GAA.TTC triplet repeats from intron I of the Friedreich ataxia gene on transcription and replication in vivo. *J. Biol. Chem.* **273,** 14588–14595 (1998).

80. Bidichandani, S. I., Ashizawa, T. & Patel, P. I. The GAA triplet-repeat expansion in Friedreich ataxia interferes with transcription and may be associated with an unusual DNA structure. *Am. J. Hum. Genet.* **62,** 111–121 (1998).

81. Grabczyk, E., Mancuso, M. & Sammarco, M. C. A persistent RNA.DNA hybrid formed by transcription of the Friedreich ataxia triplet repeat in live bacteria, and by T7 RNAP in vitro. *Nucleic Acids Res.* **35,** 5351–5359 (2007).

82. Saveliev, A., Everett, C., Sharpe, T., Webster, Z. & Festenstein, R. DNA triplet repeats mediate heterochromatin-protein-1-sensitive variegated gene silencing. *Nature* **422,** 909–913 (2003).

83. Greene, E., Mahishi, L., Entezam, A., Kumari, D. & Usdin, K. Repeat-induced epigenetic changes in intron 1 of the frataxin gene and its consequences in Friedreich ataxia. *Nucleic Acids Res.* **35,** 3383–3390 (2007).

84. Al-Mahdawi, S. *et al.* The Friedreich ataxia GAA repeat expansion mutation induces comparable epigenetic changes in human and transgenic mouse brain and heart tissues. *Hum. Mol. Genet.* **17,** 735–746 (2008).

85. Evans-Galea, M. V. *et al.* FXN methylation predicts expression and clinical outcome in Friedreich ataxia. *Ann. Neurol.* **71,** 487–497 (2012).

86. Al-Mahdawi, S., Sandi, C., Mouro Pinto, R. & Pook, M. A. Friedreich ataxia patient tissues exhibit increased 5-hydroxymethylcytosine modification and decreased CTCF binding at the FXN locus. *PLoS One* **8,** e74956 (2013).

87. Kumari, D., Biacsi, R. E. & Usdin, K. Repeat expansion affects both transcription initiation and elongation in friedreich ataxia cells. *J. Biol. Chem.* **286,** 4209–4215 (2011).

88. Herman, D. *et al.* Histone deacetylase inhibitors reverse gene silencing in Friedreich's ataxia. *Nat. Chem. Biol.* **2,** 551–558 (2006).

89. Sandi, C., Al-Mahdawi, S. & Pook, M. A. Epigenetics in friedreich's ataxia: challenges and opportunities for therapy. *Genet Res Int* **2013,** 852080 (2013).

90. Vilema-Enríquez, G. *et al.* Inhibition of the SUV4-20 H1 histone methyltransferase

increases frataxin expression in Friedreich's ataxia patient cells. *J. Biol. Chem.* **295,** 17973–17985 (2020).

91. Huang, M. L.-H. *et al.* Elucidation of the mechanism of mitochondrial iron loading in Friedreich's ataxia by analysis of a mouse mutant. *Proc. Natl. Acad. Sci. USA* **106,** 16381–16386 (2009).

92. Rötig, A. *et al.* Aconitase and mitochondrial iron-sulphur protein deficiency in Friedreich ataxia. *Nat. Genet.* **17,** 215–217 (1997).

93. Delatycki, M. B. *et al.* Direct evidence that mitochondrial iron accumulation occurs in Friedreich ataxia. *Ann. Neurol.* **45,** 673–675 (1999).

94. Sanchez-Casis, G., Cote, M. & Barbeau, A. Pathology of the heart in Friedreich's ataxia: review of the literature and report of one case. *Can J Neurol Sci* **3,** 349–354 (1976).

95. Lamarche, J. B., Côté, M. & Lemieux, B. The cardiomyopathy of Friedreich's ataxia morphological observations in 3 cases. *Can J Neurol Sci* **7,** 389–396 (1980).

96. Lamarche, J. B., Shapcott, D. & Cote, M. Cardiac iron deposits in Friedreich's ataxia. ... *disease and therapy* (1993).

97. Pandolfo, M. Iron and Friedreich ataxia. *J Neural Transm Suppl* 143–146 (2006). doi:10.1007/978-3-211-45295-0_22

98. Emond, M., Lepage, G., Vanasse, M. & Pandolfo, M. Increased levels of plasma malondialdehyde in Friedreich ataxia. *Neurology* **55,** 1752–1753 (2000).

99. Schulz, J. B. *et al.* Oxidative stress in patients with Friedreich ataxia. *Neurology* **55,**

1719–1721 (2000).

100. Bradley, J. L., Homayoun, S., Hart, P. E., Schapira, A. H. V. & Cooper, J. M. Role of oxidative damage in Friedreich's ataxia. *Neurochem. Res.* **29,** 561–567 (2004).

101. Fridovich, I. Superoxide radical and superoxide dismutases. *Annu. Rev. Biochem.* **64,** 97–112 (1995).

102. De Michele, G. & Filla, A. Movement disorders: Friedreich ataxia today—preparing for the final battle. *Nat. Rev. Neurol.* **11,** 188–190 (2015).

103. *The hereditary ataxias and related disorders*. (Churchill Livingstone, 1984).

104. Murayama, S., Bouldin, T. W. & Suzuki, K. Pathological study of corticospinal-tract degeneration in Friedreich's ataxia. *Neuropathol Appl Neurobiol* **18,** 81–86 (1992).

105. Koeppen, A. H., Morral, J. A., McComb, R. D. & Feustel, P. J. The neuropathology of late-onset Friedreich's ataxia. *Cerebellum* **10,** 96–103 (2011).

106. Hughes, J. T., Brownell, B. & Hewer, R. L. The peripheral sensory pathway in friedreich's ataxia. An examination by light and electron microscopy of the posterior nerve roots, posterior root ganglia, and peripheral sensory nerves in cases of friedreich's ataxia. *Brain* **91,** 803–818 (1968).

107. Inoue, K., Hirano, A. & Hasson, J. Friedreich's ataxia selectively involves the large neurons of the dorsal root ganglia. *Trans Am Neurol Assoc* **104,** 75–76 (1979).

108. Koeppen, A. H. *et al.* The dorsal root ganglion in Friedreich's ataxia. *Acta Neuropathol.* **118,** 763–776 (2009).

109. Koeppen, A. H. *et al.* Friedreich ataxia: metal dysmetabolism in dorsal root ganglia.

Acta Neuropathol. Commun. **1,** 26 (2013).

110. Martelli, A. & Puccio, H. Dysregulation of cellular iron metabolism in Friedreich ataxia: from primary iron-sulfur cluster deficit to mitochondrial iron accumulation. *Front. Pharmacol.* **5,** 130 (2014).

111. Pagani, E. *et al.* Assessment of brain white matter fiber bundle atrophy in patients with Friedreich ataxia. *Radiology* **255,** 882–889 (2010).

112. Akhlaghi, H. *et al.* Superior cerebellar peduncle atrophy in Friedreich's ataxia correlates with disease symptoms. *Cerebellum* **10,** 81–87 (2011).

113. Boddaert, N. *et al.* Selective iron chelation in Friedreich ataxia: biologic and clinical implications. *Blood* **110,** 401–408 (2007).

114. Koeppen, A. H. *et al.* The dentate nucleus in Friedreich's ataxia: the role of iron-responsive proteins. *Acta Neuropathol.* **114,** 163–173 (2007).

115. Lamarche, J. B., Lemieux, B. & Lieu, H. B. The neuropathology of "typical" Friedreich's ataxia in Quebec. *Can J Neurol Sci* **11,** 592–600 (1984).

116. Friedreich, N. *XVII. Leber degenerative Atrophie der spinalen Hinterstränge*. (De Gruyter, 2021).

117. Koeppen, A. H. *et al.* The pathogenesis of cardiomyopathy in Friedreich ataxia. *PLoS One* **10,** e0116396 (2015).

118. de la Grandmaison, G. L., Clairand, I. & Durigon, M. Organ weight in 684 adult autopsies: new tables for a Caucasoid population. *Forensic Sci. Int.* **119,** 149–154 (2001).

119. Pandolfo, M. *et al.* Deferiprone in Friedreich ataxia: a 6-month randomized controlled trial. *Ann. Neurol.* **76,** 509–521 (2014).

120. Pandolfo, M. & Hausmann, L. Deferiprone for the treatment of Friedreich's ataxia. *J. Neurochem.* **126 Suppl 1,** 142–146 (2013).

121. Torii, H., Yoshida, K., Kobayashi, T., Tsukamoto, T. & Tanayama, S. Disposition of idebenone (CV-2619), a new cerebral metabolism improving agent, in rats and dogs. *J. Pharmacobiodyn.* **8,** 457–467 (1985).

122. Bürk, K. Friedreich Ataxia: current status and future prospects. *Cerebellum Ataxias* **4,** 4 (2017).

123. Lynch, D. R., Perlman, S. L. & Meier, T. A phase 3, double-blind, placebo-controlled trial of idebenone in friedreich ataxia. *Arch. Neurol.* **67,** 941–947 (2010).

124. Parkinson, M. H., Schulz, J. B. & Giunti, P. Co-enzyme Q10 and idebenone use in Friedreich's ataxia. *J. Neurochem.* **126 Suppl 1,** 125–141 (2013).

125. Di Prospero, N. A., Baker, A., Jeffries, N. & Fischbeck, K. H. Neurological effects of high-dose idebenone in patients with Friedreich's ataxia: a randomised, placebo-controlled trial. *Lancet Neurol.* **6,** 878–886 (2007).

126. Sturm, B. *et al.* Carbamylated erythropoietin increases frataxin independent from the erythropoietin receptor. *Eur. J. Clin. Invest.* **40,** 561–565 (2010).

127. Sturm, B. *et al.* Recombinant human erythropoietin: effects on frataxin expression in vitro. *Eur. J. Clin. Invest.* **35,** 711–717 (2005).

128. Mariotti, C. *et al.* Erythropoietin in Friedreich ataxia. *J. Neurochem.* **126 Suppl 1,**

80–87 (2013).

129. Rufini, A. *et al.* Highly specific ubiquitin-competing molecules effectively promote frataxin accumulation and partially rescue the aconitase defect in Friedreich ataxia cells. *Neurobiol. Dis.* **75,** 91–99 (2015).

130. Vyas, P. M. *et al.* A TAT-frataxin fusion protein increases lifespan and cardiac function in a conditional Friedreich's ataxia mouse model. *Hum. Mol. Genet.* **21,** 1230–1247 (2012).

131. Perdomini, M. *et al.* Prevention and reversal of severe mitochondrial cardiomyopathy by gene therapy in a mouse model of Friedreich's ataxia. *Nat. Med.* **20,** 542–547 (2014).

132. Chutake, Y. K., Lam, C. C., Costello, W. N., Anderson, M. P. & Bidichandani, S. I. Reversal of epigenetic promoter silencing in Friedreich ataxia by a class I histone deacetylase inhibitor. *Nucleic Acids Res.* **44,** 5095–5104 (2016).

133. Sandi, C. *et al.* Prolonged treatment with pimelic o-aminobenzamide HDAC inhibitors ameliorates the disease phenotype of a Friedreich ataxia mouse model. *Neurobiol. Dis.* **42,** 496–505 (2011).

134. Chan, P. K. *et al.* Heterochromatinization induced by GAA-repeat hyperexpansion in Friedreich's ataxia can be reduced upon HDAC inhibition by vitamin B3. *Hum. Mol. Genet.* **22,** 2662–2675 (2013).

135. Libri, V. *et al.* Epigenetic and neurological effects and safety of high-dose nicotinamide in patients with Friedreich's ataxia: an exploratory, open-label, dose-escalation study. *Lancet* **384,** 504–513 (2014).

136. Nageshwaran, S. & Festenstein, R. Epigenetics and Triplet-Repeat Neurological Diseases. *Front. Neurol.* **6,** 262 (2015).

137. Jørgensen, S., Schotta, G. & Sørensen, C. S. Histone H4 lysine 20 methylation: key player in epigenetic regulation of genomic integrity. *Nucleic Acids Res.* **41,** 2797–2806 (2013).

138. Schotta, G. *et al.* A silencing pathway to induce H3-K9 and H4-K20 trimethylation at constitutive heterochromatin. *Genes Dev.* **18,** 1251–1262 (2004).

139. Gonzalo, S. *et al.* Role of the RB1 family in stabilizing histone methylation at constitutive heterochromatin. *Nat. Cell Biol.* **7,** 420–428 (2005).

140. Regha, K. *et al.* Active and repressive chromatin are interspersed without spreading in an imprinted gene cluster in the mammalian genome. *Mol. Cell* **27,** 353–366 (2007).

141. Kim, E., Napierala, M. & Dent, S. Y. R. Hyperexpansion of GAA repeats affects post-initiation steps of FXN transcription in Friedreich's ataxia. *Nucleic Acids Res.* **39,** 8366–8377 (2011).

142. Bromberg, K. D. *et al.* The SUV4-20 inhibitor A-196 verifies a role for epigenetics in genomic integrity. *Nat. Chem. Biol.* **13,** 317–324 (2017).

143. Soragni, E. *et al.* Long intronic GAA*TTC repeats induce epigenetic changes and reporter gene silencing in a molecular model of Friedreich ataxia. *Nucleic Acids Res.* **36,** 6056–6065 (2008).

144. Grant, L. *et al.* Rational selection of small molecules that increase transcription through the GAA repeats found in Friedreich's ataxia. *FEBS Lett.* **580,** 5399–5405

(2006).

145. Ditch, S., Sammarco, M. C., Banerjee, A. & Grabczyk, E. Progressive GAA.TTC repeat expansion in human cell lines. *PLoS Genet.* **5,** e1000704 (2009).

146. Li, L. *et al.* Pharmacological screening using an FXN-EGFP cellular genomic reporter assay for the therapy of Friedreich ataxia. *PLoS One* **8,** e55940 (2013).

147. Sarsero, J. P. *et al.* Upregulation of expression from the FRDA genomic locus for the therapy of Friedreich ataxia. *J Gene Med* **5,** 72–81 (2003).

148. Lufino, M. M. P. *et al.* A GAA repeat expansion reporter model of Friedreich's ataxia recapitulates the genomic context and allows rapid screening of therapeutic compounds. *Hum. Mol. Genet.* **22,** 5173–5187 (2013).

149. Takahashi, K. & Yamanaka, S. Induction of pluripotent stem cells from mouse embryonic and adult fibroblast cultures by defined factors. *Cell* **126,** 663–676 (2006).

150. Rowe, R. G. & Daley, G. Q. Induced pluripotent stem cells in disease modelling and drug discovery. *Nat. Rev. Genet.* **20,** 377–388 (2019).

151. Ross, C. A. & Akimov, S. S. Human-induced pluripotent stem cells: potential for neurodegenerative diseases. *Hum. Mol. Genet.* **23,** R17-26 (2014).

152. Schreiber, A. M., Misiorek, J. O., Napierala, J. S. & Napierala, M. Progress in understanding Friedreich's ataxia using human induced pluripotent stem cells. *Expert Opin. Orphan Drugs* **7,** 81–90 (2019).

153. Ku, S. *et al.* Friedreich's ataxia induced pluripotent stem cells model

intergenerational GAA·TTC triplet repeat instability. *Cell Stem Cell* **7,** 631–637 (2010).

154. Liu, J. *et al.* Generation of induced pluripotent stem cell lines from Friedreich ataxia patients. *Stem Cell Rev* **7,** 703–713 (2011).

155. Hick, A. *et al.* Neurons and cardiomyocytes derived from induced pluripotent stem cells as a model for mitochondrial defects in Friedreich's ataxia. *Dis. Model. Mech.* **6,** 608–621 (2013).

156. Piguet, F. *et al.* Rapid and complete reversal of sensory ataxia by gene therapy in a novel model of friedreich ataxia. *Mol. Ther.* **26,** 1940–1952 (2018).

157. McDermott, L. A. *et al.* Defining the functional role of nav1.7 in human nociception. *Neuron* **101,** 905–919.e8 (2019).

158. Dionisi, C., Rai, M., Chazalon, M., Schiffmann, S. N. & Pandolfo, M. Primary proprioceptive neurons from human induced pluripotent stem cells: a cell model for afferent ataxias. *Sci. Rep.* **10,** 7752 (2020).

159. Sherzai, M. *et al.* HMTase Inhibitors as a Potential Epigenetic-Based Therapeutic Approach for Friedreich's Ataxia. *Front. Genet.* **11,** 584 (2020).

160. Kim, H.-J. & Bae, S.-C. Histone deacetylase inhibitors: molecular mechanisms of action and clinical trials as anti-cancer drugs. *Am J Transl Res* **3,** 166–179 (2011).

161. Zhang, X., Wen, H. & Shi, X. Lysine methylation: beyond histones. *Acta Biochim. Biophys. Sin. (Shanghai)* **44,** 14–27 (2012).

162. Kaniskan, H. Ü., Martini, M. L. & Jin, J. Inhibitors of protein methyltransferases and

demethylases. *Chem. Rev.* **118,** 989–1068 (2018).

163. Husmann, D. & Gozani, O. Histone lysine methyltransferases in biology and disease. *Nat. Struct. Mol. Biol.* **26,** 880–889 (2019).

164. Lai, J.-I. *et al.* Transcriptional profiling of isogenic Friedreich ataxia neurons and effect of an HDAC inhibitor on disease signatures. *J. Biol. Chem.* **294,** 1846–1859 (2019).

165. Ignowski, J. M. & Schaffer, D. V. Kinetic analysis and modeling of firefly luciferase as a quantitative reporter gene in live mammalian cells. *Biotechnol. Bioeng.* **86,** 827–834 (2004).

166. Thompson, J. F., Hayes, L. S. & Lloyd, D. B. Modulation of firefly luciferase stability and impact on studies of gene regulation. *Gene* **103,** 171–177 (1991).

167. Ahimsadasan, N., Reddy, V. & Kumar, A. in *StatPearls* (StatPearls Publishing, 2021).

168. Marmigère, F. & Ernfors, P. Specification and connectivity of neuronal subtypes in the sensory lineage. *Nat. Rev. Neurosci.* **8,** 114–127 (2007).

169. Du, J. *et al.* Role of mismatch repair enzymes in GAA·TTC triplet-repeat expansion in Friedreich ataxia induced pluripotent stem cells. *J. Biol. Chem.* **287,** 29861–29872 (2012).

170. Petitjean, H. *et al.* Dorsal Horn Parvalbumin Neurons Are Gate-Keepers of Touch-Evoked Pain after Nerve Injury. *Cell Rep.* **13,** 1246–1257 (2015).

171. Cui, L. *et al.* Identification of early RET+ deep dorsal spinal cord interneurons in

gating pain. *Neuron* **91,** 1137–1153 (2016).

172. Mertens, J., Marchetto, M. C., Bardy, C. & Gage, F. H. Evaluating cell reprogramming, differentiation and conversion technologies in neuroscience. *Nat. Rev. Neurosci.* **17,** 424–437 (2016).

173. Vierbuchen, T. *et al.* Direct conversion of fibroblasts to functional neurons by defined factors. *Nature* **463,** 1035–1041 (2010).

174. Miller, J. D. *et al.* Human iPSC-based modeling of late-onset disease via progerin-induced aging. *Cell Stem Cell* **13,** 691–705 (2013).

175. Yiu, E. M. *et al.* An open-label trial in Friedreich ataxia suggests clinical benefit with high-dose resveratrol, without effect on frataxin levels. *J. Neurol.* **262,** 1344–1353 (2015).

176. Georges, P. *et al.* Induced pluripotent stem cells-derived neurons from patients with Friedreich ataxia exhibit differential sensitivity to resveratrol and nicotinamide. *Sci. Rep.* **9,** 14568 (2019).

177. Wong, A. O.-T. *et al.* Correlation between frataxin expression and contractility revealed by in vitro Friedreich's ataxia cardiac tissue models engineered from human pluripotent stem cells. *Stem Cell Res Ther* **10,** 203 (2019).

178. Lee, Y.-K. *et al.* Modeling of Friedreich ataxia-related iron overloading cardiomyopathy using patient-specific-induced pluripotent stem cells. *Pflugers Arch.* **466,** 1831–1844 (2014).

179. Crombie, D. E. *et al.* Friedreich's ataxia induced pluripotent stem cell-derived cardiomyocytes display electrophysiological abnormalities and calcium handling

deficiency. *Aging (Albany, NY)* **9,** 1440–1452 (2017).

180. Meier, T. & Buyse, G. Idebenone: an emerging therapy for Friedreich ataxia. *J. Neurol.* **256 Suppl 1,** 25–30 (2009).

181. Lynch, D. R. & Johnson, J. Omaveloxolone: potential new agent for Friedreich ataxia. *Neurodegener Dis Manag* **11,** 91–98 (2021).

182. Li, J. *et al.* Excision of the expanded GAA repeats corrects cardiomyopathy phenotypes of iPSC-derived Friedreich's ataxia cardiomyocytes. *Stem Cell Res.* **40,** 101529 (2019).

183. Li, Y. *et al.* Excision of expanded GAA repeats alleviates the molecular phenotype of friedreich's ataxia. *Mol. Ther.* **23,** 1055–1065 (2015).

184. Shen, X. *et al.* Efficient electroporation of neuronal cells using synthetic oligonucleotides: identifying duplex RNA and antisense oligonucleotide activators of human frataxin expression. *RNA* **25,** 1118–1129 (2019).

185. Mazzara, P. G. *et al.* Frataxin gene editing rescues Friedreich's ataxia pathology in dorsal root ganglia organoid-derived sensory neurons. *Nat. Commun.* **11,** 4178 (2020).

186. Czuba-Wojnilowicz, E. *et al.* Particle-mediated delivery of frataxin plasmid to a human sensory neuronal model of Friedreich's ataxia. *Biomater Sci* **8,** 2398–2403 (2020).

Appendices

Compound	Half-life (min) liver microsomes		Half-life (min) hepatocytes	
	Mouse	Human	Mouse	Human
A-196	5.79	7.28	10.8	48

Appendix 1: Pilot data detailing metabolic stability of A-196

Metabolic stability data showing the half-life (in mins) of A-196 tested in mice and human liver microsomes and hepatocytes.